The Impact of Magnetic Fields on Cosmological Galaxy Mergers

Joseph Whittingham
University of Potsdam

A thesis submitted for the degree of
Master of Science

February 2020

First reader: Prof. Dr. Christoph Pfrommer
Second reader: Prof. Dr. Philipp Richter

Statement of originality

This thesis is based on research carried out at the Leibniz-Institut für Astrophysik Potsdam (AIP). No part of this thesis has been submitted elsewhere for any other degree or qualification. All work presented is my own unless otherwise stated.

Abstract

The magnetic field energy density in nearby galaxies is roughly in equipartition with the turbulent, thermal, and cosmic ray energy densities. Magnetic fields are therefore expected to be dynamically important at present times. Field strengths are also expected to be strongly amplified during major mergers, which are themselves believed to be an important driver of galaxy evolution. To date, however, investigations into the relationship between magnetic fields and galaxy mergers have only used isolated set-ups. Such simulations require many free parameters, and frequently do not treat physical processes in a cosmologically self-consistent fashion. In this thesis, we present the first ever cosmologically-consistent magnetohydrodynamic (MHD) zoom-in simulations of major mergers. Our simulations employed the moving-mesh code AREPO and the comprehensive Auriga galaxy formation model. By comparing these simulations with hydrodynamic simulations run from the same initial conditions, we evaluate the impact of including MHD physics. In contrast to previous cosmological MHD simulations of isolated galaxies, we find a substantial difference. Whilst magnetic fields do not strongly impact global properties such as the star formation rate and total stellar mass, we find that they dramatically affect the morphology produced. Furthermore, we find that this effect is only uncovered with high enough resolution. We identify increased AGN feedback in the MHD simulations as the primary cause.

Zusammenfassung

Die Energiedichte des Magnetfeldes in nahe gelegenen Galaxien entspricht ungefähr der Energiedichte des turbulenten und thermischen Gases sowie der kosmischen Strahlung. Es wird daher erwartet, dass Magnetfelder gegenwärtig für die galaktische Dynamik wichtig sind. Es wird auch erwartet, dass die Feldstärken bei größeren Galaxienverschmelzungen stark ansteigen, die ihrerseits sehr wahrscheinlich einen wichtigen Antrieb in der Entwicklung von Galaxien darstellen. Bisher wurden bei Untersuchungen des Zusammenhangs zwischen Magnetfeldern und Galaxienverschmelzungen nur Simulationen isolierter Galaxien verwendet. Solche Simulationen erfordern viele freie Parameter und behandeln physikalische Prozesse häufig nicht kosmologisch konsistent. In dieser Arbeit präsentieren wir die ersten kosmologisch konsistenten magnetohydrodynamischen (MHD) Zoom-In-Simulationen von größeren Galaxienverschmelzungen. In unseren Simulationen verwenden wir den bewegten Gittercode AREPO und das umfassende Auriga-Galaxienbildungsmodell. Durch den Vergleich dieser Simulationen mit hydrodynamischen Simulationen, die unter denselben Anfangsbedingungen durchgeführt wurden, bewerten wir die Auswirkungen der Einbeziehung der Magnetohydrodynamik. Im Gegensatz zu früheren kosmologischen MHD-Simulationen isolierter Galaxien hat die Einbeziehung von MHD einen erheblichen Einfluss auf die Simulationen. Obwohl Magnetfelder globale Eigenschaften wie die Sternentstehungsrate und die gesamte Sternmasse nicht stark beeinflussen, stellen wir fest, dass sie die erzeugte Morphologie dramatisch beeinflussen. Darüber hinaus stellen wir fest, dass dieser Effekt nur mit einer ausreichend hohen Simulationsauflösung aufgedeckt wird. Wir identifizieren eine erhöhte AGN-Rückkopplung in den MHD-Simulationen als Hauptursache dieses Effekts.

Acknowledgements

The completion of this thesis would not have been possible without the support of a multitude of people. In particular, I would like to express my thanks to the Leibniz Institute for Astrophysics (AIP) in Potsdam for providing me with the resources to perform this research. I would also like to express my appreciation of the Cosmology department at AIP for being a lively, sociable, and generally pleasant place to work in. Similarly, I would like to express my thanks to the members of staff in the Astrophysics department at the University of Potsdam and to the enthusiastic teachers there who taught me during my studies. On a personal level, I would also like to thank Prof. Dr. Christoph Pfrommer for his direction and advice during this project, Dr. Rüdiger Pakmor for providing the data that was used to help construct the figures in sections 3.1.4, 3.3.5, and 3.3.6, and I would especially like to thank Dr. Martin Sparre for the countless hours of conversation and advice, as well as his patience and friendship throughout. Finally, I would like to thank my friends and family for their support and encouragement, without which none of this would have been possible.

Contents

List of Figures

Chapter 1

Introduction

Mergers play a key role in the evolution of galaxies. They give rise to a rapidly varying gravitational potential, which can have dramatic consequences for the galactic components and their kinematics. Being diffusive, the gas component of the galaxy is particularly sensitive to such changes. During a merger, gas may be drawn deep into the galaxy, leading to bursts in star formation. It may also be expelled almost entirely, transforming the galaxy into a so-called *red and dead* galaxy. Under the theory of hierarchical structure formation, mergers are not infrequent. Indeed, for late times they are suggested to be the driving force of massive galaxy evolution (Hopkins et al., 2008; Tacchella et al., 2019). Such predictions are supported from observations, which have shown that half of all galaxies with present-day masses of $M_* > 5 \times 10^{10}$ $M_\odot$ are likely to have undergone a major merger since $z = 0.8$ (Bell et al., 2006).

Radio observations, amongst other evidence, has shown that most late type galaxies in the local Universe are permeated by magnetic fields (Beck et al., 1985; Beck and Hoernes, 1996). Indeed, for these galaxies the magnetic pressure in the interstellar medium (ISM) is believed to be roughly in equipartition with the thermal gas pressure (Arshakian et al., 2009). These observations suggest that magnetic fields may be dynamically important for the evolution of galaxies. As the gas in the galactic halo is almost fully ionised, and that in the ISM is at least partially ionised, magnetic fields may also be considered to be intimately coupled to the gas component of galaxies (Ferrière, 2001). This means that as the gas is disrupted so are the magnetic fields, with fields becoming strengthened by shocks and gas inflow and weakened by gas expulsion and disruption to dynamo processes. As such effects are heightened during a merger, magnetic fields may have an important role to play in the outcome of galaxy mergers. Furthermore, if magnetic fields are significantly altered during a merger, observing them could also provide a window onto the merger history of galaxies.

Naturally, the interplay between the forces and components involved in this problem is extremely

non-linear. It is therefore best investigated through the use of numerical simulations. However, there are an extraordinary range of dynamic scales to cover: resolving the turbulence generated in the galaxies is expected to require close to parsec resolution (Teyssier et al., 2010; Renaud et al., 2014). On the other hand, parameters such as the impact velocity and the overall gravitational field experienced by the participating galaxies comes from the environmental context. This requires resolving tens of Mpc. In an attempt to reconcile the differences between these scales, we use the technique of high-resolution cosmological "zoom-in" simulations. Such simulations are able to probe the fine-scale nature of the problem, including stellar and black hole feedback (e.g. Grand et al., 2017, hereafter G17), without resorting to the use of arbitrary parameters, as required in idealised set-ups. Implementing a proper treatment of magnetohydrodynamics in such simulations is technically challenging, and has only recently been achieved in a satisfactory manner (Pakmor et al., 2014). Now that these methods exist and have been found to be reliable, it is finally possible to investigate the impact of magnetic fields on galaxy mergers, and vice versa, in a proper cosmological context. We do this here for the first time through comparison of hydrodynamic and magnetohydrodynamic (MHD) simulations of major mergers of late-type galaxies based on the same initial conditions.

This thesis is organised in the following way: in the following section, we recap the physics involved in the problem. This includes: the theory of large-scale structure formation, as used in our cosmological simulations; some of the key physical processes required in galaxy formation and evolution models; our current theoretical understanding of galaxy mergers; and a brief summary of what is known of cosmological magnetism and of its role in galaxy evolution. In Chapter 2 we introduce our simulations and the numerical methods we used, including the galaxy formation model and MHD implementation. In Chapter 3, we present results of tests done to validate our methods, followed by our simulation results and analysis thereof. In Chapter 4, we identify caveats of the main work, and suggest possible future extensions. Finally, in Chapter 5 we summarise our main conclusions.

1.1 Large-scale structure formation

Over the last few decades, cosmology has made great strides in tackling the problem of large-scale structure formation. Indeed, the astrophysics community has now generally settled on a standard model for cosmology known as the ΛCDM model[1] (White and Rees, 1978; Blumenthal et al., 1984). This theory has had a lot of success in being able to predict the observed distribution of galaxies, clusters, and voids. As with most of the other competing cosmological models, it is based on two main assumptions:

i) The Universe is homogeneous and isotropic.

ii) The Universe is governed by its mass-energy content, which acts according to Einstein's theory of General Relativity.

The first supposition is known as *the cosmological principle*, and it appears to be consistent with observations made thus far. For example, the Sloan Digital Sky Survey (SDSS), which claims to have created the most detailed three-dimensional maps of the Universe ever made, shows that the Universe is roughly homogeneous on scales larger than 70 Mpc/h (Blanton et al., 2017). Similarly, the cosmic microwave background (CMB) appears to be roughly isotropic for all lines of sight (Jarosik et al., 2011; Planck Collaboration, 2014, 2018). Together, these assumptions lead to the Friedmann-Lemaître-Robertson-Walker (FLRW) metric. This metric may be used to understand the appearance of objects at cosmological distances, as affected by the curvature of space-time. We may also derive the Friedmann equations from it, which govern the expansion of space-time in such a universe.

Under the ΛCDM model, the matter-energy content of the Universe is divided into three distinct categories: i) ordinary or "baryonic" matter, ii) dark matter, and iii) dark energy. In contrast to the particle physics definition, baryonic matter in cosmology is considered to be all objects made of protons, neutrons, and electrons. In practise, this means matter that takes the form of stars, gas, or dust. Dark matter, on the other hand, is considered to be all other forms of matter. It is uncertain what the majority of dark matter is composed of, but its existence is strongly implied from a variety of astrophysical observations. Evidence for dark matter starts as early as the beginning of the 20th century, when several authors reported inconsistencies to be found between calculating the mass of large composite objects from mass-luminosity relations versus that obtained by applying Kepler's laws or the virial theorem to the observed velocity dispersion.

[1] Naturally, there are competitors to this theory, such as Modified Newtonian Dynamics (MOND), but these will not be discussed here.

Most notably, Swiss astrophysicist Fritz Zwicky used these two methods to calculate the mass of the Coma Cluster in 1933 and concluded that the majority of the mass in the cluster must be unseen (Zwicky, 1933). In the 1970s, as spectrograph technology became better developed, further strong evidence was provided for dark matter through the observation of galaxy rotation curves. It was found that stars in spiral galaxies exhibited either flat or rising rotation velocities with increasing radius, implying the existence of a significant amount of non-luminous matter beyond the optical galaxy (Rubin and Ford, 1970; Freeman, 1970). Such results initially proved controversial, but have since been confirmed over subsequent decades (Rubin et al., 1980). To strengthen the case further, strong evidence for the existence of dark matter has also been produced through other methods such as the gravitational lensing of background objects by galaxy clusters (Taylor et al., 1998).

The evidence for dark energy is also indirect, but again comes from many independent sources. The most often cited sources of evidence for dark energy are: i) supernovae distances in comparison with their cosmological redshift showing that the Universe is expanding at an accelerating rate (Riess et al., 1998; Perlmutter et al., 1999), ii) the observation of a geometrically flat universe resulting in the need for an additional energy term in the Friedmann acceleration equation (de Bernardis et al., 2000), and iii) measurements of the baryon acoustic oscillations (BAO) — the fluctuations in the density of visible baryonic matter in the Universe (Eisenstein et al., 2005). The simplest possible explanation for dark energy, and the explanation invoked in ΛCDM, is that it is an intrinsic, fundamental energy of space, known as the cosmological constant. This constant is usually represented by the Greek capital letter lambda: Λ. Through mass-energy equivalence this cosmological constant also has a gravitational effect. Indeed, it actually has a strong negative pressure, with an equation of state given as $p = \omega\rho$, where $\omega < -1/3$, and p and ρ are pressure and density, respectively. Dark energy is also the dominant component in the Universe. From current observations it is estimated that $\sim 70\%$ of the Universe takes the form of dark energy, with a further $\sim 25\%$ being dark matter, and only the remaining $\sim 5\%$ being baryonic matter (Jarosik et al., 2011; Planck Collaboration, 2014, 2018). Of these three types, the first two are the most influential factors in the theory of cosmological structure formation.

Different types of dark matter would affect the structure formation process differently, so it is worth discussing the properties of dark matter as supported in the current theory. In ΛCDM the dark matter component is collisionless, dissipationless, and cold. *Collisionless*, in this respect, means that the dark matter interacts only very weakly, other than via the gravitational force. Perhaps the best evidence so far for dark matter being collisionless comes from gravitational lensing studies of the two colliding galaxy clusters in the Bullet Cluster, which show the majority of the mass is in a clear bi-modal distribution following the initial cluster collision (Clowe et al.,

2004; Markevitch et al., 2004). *Dissipationless* means that the dark matter may not cool by radiating photons, which is necessary in order to explain why it may not be observed directly. Finally, *cold* is here taken to mean that that the velocity of dark matter at the era of radiation-matter equality was far less than the speed of light. Cold Dark Matter (CDM) provides the final part of the acronym in ΛCDM, but the distinction between hot and cold dark matter is also of vital importance in terms of structure formation. Dark matter in the early Universe was able to move a certain distance on average before before falling into a potential well. Such distance is known as the *free streaming length* and naturally increases with the velocity of the dark matter particle. Density fluctuations smaller than the free streaming length were washed out, as particles spread from overdense to underdense regions, in effect setting the minimum scale for later structure fluctuation. This minimum scale dictates whether structure formed "top-down" or "bottom-up"; that is, whether large matter aggregations formed early before fragmenting into separate galaxies, or whether galaxies formed first with larger, more complex structure forming later.

Deep-field observations now rule-out "top-down" formation, showing that smaller structure does indeed form before larger structure (Babul and Ferguson, 1996; Madau and Dickinson, 2014). We may therefore feel confident in only concentrating on "bottom-up" or "hierarchical" structure formation. Hierarchical structure formation is a feature that is present in all cold dark matter models, and proceeds thusly: during a period of rapid expansion, known as inflation, quantum fluctuations in the primordial energy distribution were magnified to cosmic size. As the Universe expanded further, regions with a higher than average density expanded more slowly due to their self-gravitational attraction. Correspondingly, regions with a lower than average density expanded more quickly than their surroundings. Eventually, once a region became about twice as dense as a typical region its size (see e.g. Peebles, 1970; Primack, 2009), it stopped expanding all together and collapsed to form a virialised structure. As dark matter is dissipationless, and consequently does not gain any support from radiation pressure, it was the first type of matter to collapse, forming so-called *dark matter haloes*. It is possible to construct models of inflation such that the primordial energy distribution may be described by a Gaussian random field characterised by a power spectrum of the form $P_0(k) = Ak^n$, where n is the spectral index and takes a value of $n \approx 1$[2]. This primoridal power spectrum must then be convolved with a *transfer function* (Bardeen et al., 1986) to describe its evolution after physical processes such as free-streaming or the Meszaros effect (Meszaros, 1974). The final processed power spectrum then takes the form $P(k) = P_0(k)|T^2(k)|$ and is consistent with observations of the temperature anisotropies in the CMB (Smoot et al., 1992). It may be seen that this power spectrum provides greater power for higher wavenumbers. This is equivalent to higher power for smaller scales, as

[2] A choice of $n = 1$ is often called the "scale-free" or "Harrison-Zel'Dovich" power spectrum.

k is inversely proportional to physical size. Consequently, perturbations on smaller scales have higher characteristic amplitudes, and so smaller objects collapse first before merging with larger objects in a hierarchical manner.

As long as density perturbations remain small, their evolution may be tracked analytically using well-defined linear perturbation theory (e.g. Zel'Dovich, 1970). However, as the perturbations grow in size, their evolution reaches a non-linear regime, which may only be tracked numerically. To this end, there have been many cold dark matter simulations performed. These simulations generally agree with one another and predict a highly inhomogeneous distribution on small scales, displaying a web-like structure, consisting of voids, walls, filaments and haloes (Davis et al., 1985; Navarro et al., 1996; Springel et al., 2005b; Klypin et al., 2011). Such structure may be quantified and compared to observational results through power spectrum analysis (Cole et al., 2005) or using methods such as subhalo abundance matching to produce theoretical galaxy distributions (Trujillo-Gomez et al., 2011; Chaves-Montero et al., 2016), which may then be compared to observational results using functions such as the two-point correlation function (Maddox et al., 1990). A prime example of this is the Millennium Simulation, which was able to faithfully reproduce many of the characteristics seen in SDSS sky maps (Springel et al., 2006). Without the ability to radiate away its potential energy though, dark matter structures tend to be relatively diffuse. Smaller, denser structures require baryonic physics.

1.2 Physical processes in galaxy formation

As the Universe expanded, it cooled. At $z = 1100$, or about 380 thousand years after the Big Bang, the Universe had cooled to a temperature of around 3000 K, and ionised plasma from the early Universe was able to stably recombine, forming mostly neutral hydrogen. This epoch is often referred to as the *era of recombination* and, as neutral hydrogen is unobservable throughout most of the electromagnetic spectrum, the era following is sometimes referred to as the *dark ages*. The earlier formation of primordial dark matter haloes provided the additional gravitational attraction needed for neutral gas to overcome its thermal and radiative pressures and collapse as well. This gas is believed to have collapsed into pressure-supported quasi-hydrostatic gaseous haloes, where it cooled slowly (Rees and Ostriker, 1977). The subsequent evolution of the gas was dependent on its ability to radiate away the extra energy.

The main cooling processes relevant in this picture, and for galaxy formation over cosmic history, may be separated into three regimes: gas that is hotter than 10^7 K is fully ionised and cools predominantly via bremsstrahlung (free-free emission); gas that is in the temperature range

of 10^4 K $\leq T \leq 10^7$ K is partially collisionally ionised and may decay to its ground state, allowing electrons and ions to recombine; and gas below 10^4 K cools via molecular and metal line cooling (Somerville and Davé, 2015). The effectiveness of each of these modes depends on the metallicity of the gas involved, but they may be summed over to create a single cooling function (e.g. Sutherland and Dopita, 1993; Wiersma et al., 2009). The cooling processes presented here were also augmented by inverse Compton scattering during the early Universe ($z \gtrsim 5$), when the density of cosmic microwave background photons was sufficiently high (Ikeuchi and Ostriker, 1986).

The time taken for the gas to reach thermal equilibrium is known as the cooling timescale. This is the thermal energy of the gas per unit volume divided by the cooling rate:

$$t_{\text{cool}} = \frac{\frac{3}{2}nkT}{n_{\text{H}}^2 \Lambda}$$

where Λ is the cooling function normalised by the hydrogen number density squared, n_{H}^2. As can be seen, t_{cool} decreases with increasing density. This eventually leads to a period of runaway cooling, where the gas is unable to respond to the loss of pressure. Such a process eventually leads to the formation of giant molecular clouds. Eventually dense cores within these clouds collapse even further to the densities required to ignite nuclear fusion thereby forming stars (McKee and Ostriker, 2007). Considering only molecular hydrogen cooling — the predominant constituent in the early Universe, as noted earlier — the Jeans mass[3] for the first stars is expected to be between 10^2 $\text{M}_\odot$ and 10^3 $\text{M}_\odot$ (Abel et al., 2002). Such *Population III* stars would have unavoidably affected their neighbouring environment and the subsequent star formation. Their radiation would have been able to reionise nearby regions, affecting cooling rates and inducing star formation down to scales of ~ 40 $\text{M}_\odot$, generating so-called Population III.2 stars (Yoshida et al., 2007). In turn, as the stars evolved they would synthesise new elements. These elements would be expelled by supernovae and stellar winds, enhancing cooling at low temperatures in the neighbourhood and inducing the creation of Population II stars. Massive Population III stars may also have led to the first super massive black holes (Bromm and Loeb, 2003), which are to be found in nearly all large galaxies (Kormendy and Ho, 2013).

As yet, no Population III star has ever been observed, and thus they remain a purely hypothetical construct. It is believed that the lack of detection is because the stars were exclusively high-mass, and as such would have exhausted their nuclear fuel on short time scales, existing today only as remnants. It is well understood that the evolution of a single star is determined almost entirely by its initial mass (Hopkins, 2018). To this end, much work has been done on empirically quantifying the *initial mass function* (IMF), which establishes the probability that a star will enter the

[3]The minimum mass for which a spherical, gaseous cloud is unstable to collapse.

main sequence at a given mass (e.g. Salpeter, 1955; Kroupa, 2001; Chabrier, 2003). In theory, this distribution should change with varying star-forming conditions, and some authors have indeed argued for temporal or spatial variations in the IMF (e.g. van Dokkum and Conroy, 2010; Gunawardhana et al., 2011). In general though, such claims are still considered controversial (Bastian et al., 2010; Chabrier et al., 2014), and the IMF is normally taken to be a universal distribution.

The efficiency with which gas is converted into stars also appears to be nearly universal. On physical grounds we may expect a relation between the gas density and star formation rate (SFR) in a given region, and such a relation is borne out by the Kennicutt-Schmidt law (Schmidt, 1959; Kennicutt, 1998). As most observations of external galaxies may only measure surface densities integrated along lines of sight, this relation is also given in terms of surface densities, relating the star formation rate surface density to the gas surface density: $\Sigma_{\rm SFR} \propto (\Sigma_{\rm gas})^n$. Here too there have been suggestions that the relation may evolve with redshift or have a metallicity dependence (Dib, 2011; Scoville et al., 2016). However, such dependencies are again disputed, particularly in the case of high gas surface densities (Orr et al., 2018). There is increasing evidence that the Kennicutt-Schmidt law is a result of feedback processes at the giant molecular cloud scale (Hopkins et al., 2014; Agertz and Kravtsov, 2016). It has also been demonstrated that a power law star formation relation at this scale can imprint a power law of identical slope at the galactic scale (Gnedin and Kravtsov, 2011), explaining how the relation holds over several orders of magnitude.

Feedback is also a concept that is invoked increasingly frequently in order to explain a series of remaining problems in the ΛCDM model. In particular, it is used to explain why the stellar to dark mass fraction ($M_\star/M_h$) for observed galaxies is so far below the cosmological baryon fraction. For example, galaxies with Milky Way-size haloes have $M_\star/M_{\rm h} \approx 3-5\%$ whilst the cosmological baryon fraction is $\Omega_b/\Omega_m \approx 16\%$ (Kravtsov et al., 2018). Whilst this is clearly inefficient, the efficiency becomes even worse at both smaller and larger masses (Moster et al., 2010; Behroozi et al., 2013). At smaller masses photo-heating, photo-ionisation, and winds from stellar feedback are expected to reduce the star formation efficiency (Hopkins et al., 2012; Marinacci et al., 2019), whilst at the high mass end active galactic nuclei (AGN) feedback is expected to reduce the star formation efficiency (Silk and Rees, 1998). Observational signatures of AGN feedback include high velocity winds, which may eject cold star-forming gas from the galaxy, and hot "bubbles", apparently generated by radio jets, which heat the halo gas (Heckman and Best, 2014).

The energetics of AGN feedback is governed by the black hole mass, which also strongly affects the

kinematics of the host galaxy, as may be seen from the well-known $M_{\rm BH} - \sigma$ relation (Ferrarese and Merritt, 2000; Gebhardt et al., 2000). Black holes are believed to grow either through mergers with other black holes or through the accretion of gas within a sphere of influence. Mass growth from gas accretion is usually described by the Bondi-Hoyle-Lyttleton model and is limited at the Eddington rate (Bondi and Hoyle, 1944; Bondi, 1952). This model predicts reasonably low accretion rates when galaxies are undisturbed, but may be boosted to levels sufficient to drive powerful quasars when gas is driven towards the galactic nucleus, as is understood to happen during a major merger (Di Matteo et al., 2005). The Bondi-Hoyle-Lyttleton model does, however, implicitly assume that the accreting gas has negligible angular momentum, which is not necessarily a good assumption in general (Somerville and Davé, 2015). Furthermore, some competing models that attempt to explicitly model the dissipation of angular momentum have shown qualitatively different behaviour from Bondi accretion (e.g. Hopkins and Quataert, 2011).

Together the physical processes listed above create galaxies of a range of sizes and morphologies. Traditionally, these morphologies have been grouped into three categories: elliptical, spiral, and irregular; such as in the well-known Hubble sequence (Hubble, 1926, 1936). Unlike irregular galaxies, elliptical and spiral galaxies exhibit clear morphologies, and may be defined through a distinct set of criteria.

Elliptical galaxies are spheroidal in nature and generally lack developed internal structure. This gives them a smooth intensity distribution, with their surface brightness well described by a "de Vaucouleurs" profile (de Vaucouleurs, 1948) — or equivalently a Sérsic profile with $n = 4$ (Sérsic, 1963). The stellar content that produces these profiles tends to be relatively uniform and predominantly old, resulting in the galaxies having higher flux in the red end of the spectrum (Bower et al., 1992). Older stellar populations require very low star formation rates, and such a low SFR is traditionally attributed to a lack of cold gas (i.e. HI) and dust in the galaxy (Faber and Gallagher, 1976). However, there has been some recent evidence that points to the existence of residual gas reservoirs (Crocker et al., 2011) and recent star formation (Combes et al., 2007) in at least a fraction of such galaxies. Elliptical galaxies are also supported mostly through anisotropic velocity dispersion rather than through rotation (Binney, 1978).

Spiral galaxies, in contrast to ellipticals, exhibit very developed structure. This structure is usually separated into: a rotationally-supported, flattened disc, with large spiral arm structures; a central bulge, which shows some of the features of elliptical galaxies; and a pressure-supported gaseous halo. About two thirds of spiral galaxies also show a bar structure (de Vaucouleurs, 1963), which is understood to form due to gravitational instabilities (Bournaud and Combes, 2002). The disc has an approximately exponential profile (Freeman, 1970), or equivalently a Sérsic profile

with $n = 1$. Most spiral galaxies also show a chemically and kinematically independent thicker disk, which contains an older star population (Yoachim and Dalcanton, 2006). Significant star formation is observed in the spiral arms, where there is also a large amount of dust and cold gas.

1.3 Mergers in galaxy evolution

In Hubble's sequence, elliptical galaxies are referred to as *early-type* galaxies and spiral galaxies as *late-type* galaxies. Hubble emphasised that such terminology referred to the position of the galaxy in the sequence and was *not* an indication of an evolutionary sequence (Hubble, 1927). However, even Hubble could not help but mention the similarity of his sequence to the evolutionary theory put forward by Jeans (Jeans, 1928), which suggested that disc galaxies could be formed through the monolithic collapse of spherical nebulae, with tidal forcing at the two opposite ends of the flattened nebulae producing the spiral structure. The similarities between the morphology of elliptical galaxies and the bulge component of spiral galaxies (Sandage, 1961) was also taken to imply an evolutionary link.

Despite this, observational results and improved theoretical understanding over the past decades have essentially ruled out scenarios where early Hubble types transform into late ones. For example, it is now known that early-type galaxies are in general more massive than late-type galaxies (Naab and Ostriker, 2017), and that early-type *spiral* galaxies are also more massive than their late-type analogues (Freeman, 1970). Indeed, it appears that the other direction — that late type galaxies should be transforming into early-type ones — is more likely. This is supported by the observation that there are many more late-type galaxies at an intermediate to late redshift than at the present day (Couch et al., 1998), and that there is a smooth and systematic variation of galaxy number counts from late to earlier Hubble types as redshift decreases (Zhang, 1999).

In a series of seminal papers, Toomre and Toomre (1972) and Toomre (1974, 1977) proposed that such an evolution might occur through mergers. The brothers had been investigating tidal forces between interacting galaxies and had found that the stellar bridges and tails commonly seen in interacting and irregular galaxies could be explained purely through gravitational effects. This result was found by simulating encounters between two spiral galaxies, where the galaxies were modelled as rings of massless test particles orbiting a central potential[4]. It was noted that the loss of angular momentum to these tidal tails could result in the formation of elliptical-looking galaxies. Toomre (1977) also observed that galaxies embedded in extensive haloes would undergo this transformation even more completely and rapidly due to dynamical friction (Chandrasekhar,

[4]This is known as the *restricted three-body* technique.

1942). In this case, the matter in the galaxies would quickly undergo a process known as *violent relaxation* (Lynden-Bell, 1967), where stellar orbits are randomised and the system loses all memory of its previous configuration.

With the advent of hierarchical cosmological theories (White and Rees, 1978) merging became a natural consequence of structure formation, especially at early times. The theory also gained support through the observation that elliptical galaxies tended to reside in high density regions, whilst spiral galaxies tend to reside in low density regions (Dressler, 1980), as predicted by the merger scenario of Tremaine et al. (1975). Consequently, the 1980s saw a range of galaxy merger simulations. These simulations were now full N-body simulations but, due to computational expense, tended to embed discs in relatively low-mass dark matter haloes (e.g. Gerhard, 1981; Negroponte and White, 1983). A consequence of this was that the orbital angular momentum of the merging galaxies was mostly converted into internal spin, producing galaxies that looked morphologically correct but rotated too quickly. This problem was alleviated by the introduction of tree codes (Barnes and Hut, 1986). Such codes reduced the computational expense for simulating N particles from $\mathcal{O}(N^2)$ to $\mathcal{O}(N \log N)$. This allowed the modelling of much more extended dark matter haloes, which produced better agreement with observations (Barnes, 1988).

As well as a kinematic transformation, Toomre and Toomre (1972) also noted that many of the galaxies they were attempting to model displayed unusually high star formation rates. In a discussion section entitled *Stoking the Furnace?* they suggested that if mergers and tidal interactions were having a strong impact on the stellar kinematics, this would also be the case for the gas component of galaxies. Cold gas could then be brought deep into the galaxy, triggering this star formation. Due to the added computational expense, early work mostly ignored the gas component in mergers[5]. However, Noguchi (1987), for example, was able to show that tidal encounters could trigger bar formation in stellar discs, which could then extract angular momentum by gravitationally torquing the gas.

The first accurate treatments of the gas as a fluid were done through the use of smoothed particle hydrodynamics (see Subsection 2.1.2). Barnes and Hernquist (1991), in particular, were able to employ this technique to show how a merger could transport $\sim 5 \times 10^9$ $M_\odot$ of gas (roughly 60% of that in the simulation) to the central 200 pc of a galaxy. Mihos and Hernquist (1996) built upon this work by adding a star formation model using the Kennicutt-Schmidt law (see Section 1.2). This model provided the final step to showing that mergers could lead to intense starbursts and to the formation of ultra-luminous infra-red galaxies (ULIRGs). Major mergers are now understood to be a significant contributor to the ULIRG population, particularly in the local

[5] A notable exception is Negroponte and White (1983) who used a 'sticky-particle' approximation.

Universe (Draper and Ballantyne, 2012).

The inclusion of the gas component in merger simulations also caused some problems, however. If the progenitor galaxies were gas-rich and had high enough orbital angular momentum, a stellar disc was able to reform (Robertson et al., 2006). On the one hand, this provided a mechanism for late-type spiral galaxies to be transformed into early-type spiral galaxies. On the other hand, as most mergers in the early Universe are expected to be gas-rich, this would prevent the formation of elliptical galaxies at early enough times. A mechanism was needed to *quench* galaxies after a merger. Circumstantial evidence suggested an evolutionary link between ULIRGs and AGN activity (Sanders et al., 1988). This activity would be able to prevent the regrowth of the stellar disc by expelling gas from the galaxy (see Section 1.2). This mechanism was modelled successfully by Springel et al. (2005a) by assuming that a fraction of the gas that reached the centre of the galaxy was accreted by the black hole, powering the AGN feedback. The model managed to significantly reduce the star formation rate when the black hole reached a critical size, thus allowing the remnant to evolve quickly from a blue to a red galaxy again.

The process of galaxies evolving through mergers to be quenched was codified through the *Hopkins merger scenario* (Hopkins et al., 2008). However, it is important to note that this is not necessarily a linear pathway. For example, Sparre and Springel (2017) showed that mergers between gas-rich galaxies with stellar masses of $\sim 10^{10}$ $M_{\odot}$ could still regrow their discs in cosmological simulations, even when reasonably strong AGN feedback was included. It therefore appears that the gas component of galaxies still has a critical role to play in the outcome of mergers. As previously noted, this gas is also often fully or at least partially ionised and its motion is consequently described by the equations of magnetohydrodynamics.

1.4 Cosmological magnetism

Magnetic fields occur on every physical scale yet probed, but have only recently begun to be seriously investigated on the cosmological scale. Galactic magnetic fields were first proposed in 1949 by Enrico Fermi, who suggested that such a field could play an important role in the generation of the observed high energy cosmic rays in the Milky Way (Fermi, 1949). Observations of the local Galactic magnetic field followed soon after (e.g. Kiepenheuer, 1950) but it was not until the late 1970s that studies of the Galactic magnetic field beyond our own spiral arm really began (Ruzmaikin and Sokolov, 1977; Simard-Normandin and Kronberg, 1979).

Early observations led to the belief that magnetic fields in the ISM reached strengths of only a few

μG. This may be converted into an energy density, and thereby compared with other elements of the ISM. The energy density of a magnetic field — or *magnetic pressure* — in CGS units is equal to $B^2/8\pi$, where B is the magnetic field strength. A magnetic field strength of a few μG therefore equates to a magnetic pressure of $< 10^{-12}$ erg cm^{-3}. In comparison, the turbulent energy density of the gas in the ISM is on the order of $10^{-11} - 10^{-12}$ erg cm^{-3} (Beck, 2007). Magnetic fields were hence believed to be dynamically unimportant from an energetic standpoint. However, as technology and observational techniques improved, it was eventually recognised that field strengths had been largely underestimated. In gas-rich galaxies they are regularly an order of magnitude higher than this, and in the central starburst regions of galaxies field strengths of 50 μG to 100 μG have been recorded (Heesen et al., 2011; Adebahr et al., 2013). In these regions, the magnetic field actually contributes significantly to the total pressure, balancing the gas disc against gravitation and changing the dynamics of the gas flow. This impact is only increased when the controlling effect of the magnetic field on the anisotropic transport of charged particles is considered.

One of the difficulties in studying magnetic fields is that, in contrast with other components of the ISM, they do not radiate. Consequently, direct measurements of the field must be done *in situ*. While this is achievable for the near-Earth environment, it is clearly not possible for distances far outside the solar system. In order to probe the strength and geometry of magnetic fields at these distances the use of indirect methods is required. The major methods used are as follows:

- *Zeeman splitting:* An external magnetic field lifts the degeneracy of quantum mechanical energy levels, resulting in the splitting of the relevant spectral lines in a manner proportional to the field strength. This technique is often used to study the magnetic fields in compact objects such as molecular clouds or stars (Li and Henning, 2011), but has also been applied to investigations of the local diffuse ISM (Heiles and Robishaw, 2009).

- *Polarisation of starlight:* In the presence of a magnetic field, dust particles align their minor axis parallel to the field direction via the Davis-Greenstein mechanism (Davis and Greenstein, 1951). When starlight passes through a region containing such grains, the light is also polarised parallel to the field. This polarisation is then seen projected onto the plane perpendicular to the line-of-sight. Field strengths may then also be crudely estimated using the Chandrasekhar-Fermi method (Chandrasekhar and Fermi, 1953). In general, this technique requires a high flux of optical light, making it only useful for probing nearby magnetic fields, such as those within the local spiral arm (Heiles, 1996).

- *Polarisation of infrared emission from dust:* As well as polarising star light, dust grains

also radiate polarised light in the infrared. Magnetic fields may therefore also be analysed when starlight is blocked (see e.g. Hildebrand, 1988). This technique has recently begun to be applied to external galaxies (e.g. Lopez-Rodriguez et al., 2019).

- *Synchrotron radiation:* Synchrotron radiation is electromagnetic radiation emitted when charged particles are accelerated radially. The intensity and polarisation of this emission is proportional to the density of relativistic particles and the magnetic field strength in the emitting region. Assuming that the contributions from both factors are approximately equal — a condition known as the *equipartition condition* — properties of the magnetic fields may be inferred for external galaxies (Beck, 2009). The similarity of values derived for the Milky Way relative to that given by the methods listed above provides evidence that the equipartition condition is a valid assumption (Beck, 2015).

- *Faraday rotation:* The Faraday rotation effect appears during the propagation of electromagnetic waves in a magnetised plasma. If this wave is already polarised, its rotation in radians may be well described by the formula: $\Psi = 812\ \lambda^2 \int n_e \mathbf{B} \cdot d\mathbf{l} = \lambda^2 \mathrm{RM}$, where λ [m] is the wavelength of the wave, n_e [cm^{-3}] is the electron density, $\mathbf{B}$ [μG] is the magnetic field, d$\mathbf{l}$ [kpc] is the element of the path length (defined as the distanced between the source and observer), and RM [rad m^{-2}] is the observable quantity known as *rotation measure*. Pulsars, amongst other compact sources, often provide highly linearly polarised radiation. Observations of the pulse dispersion as a function of frequency provides a measure of the column density of electrons in the line of sight. Combining this relation and the Faraday rotation measure formula, we may therefore obtain a value for the mean line-of-sight component of the magnetic field. This value is weighted by the thermal electron density, which means that it provides an excellent estimate of the intermediate interstellar or galactic magnetic field (Manchester, 1972).

The last two techniques have provided the majority of information on extra-galactic magnetic fields. Radio synchrotron results in particular have shown that spiral galaxies have a mean magnetic field strength of about 9 μG (Niklas, 1995; Beck, 2000), with strengths ranging from $\sim$ 4 μG in radio faint galaxies like M31 and M33 to $\sim$ 15 μG in grand design spiral galaxies like M51, M83, and NGC 6946 (Beck, 2004). Faraday rotation maps, on the other hand, have shown that magnetic fields in spiral galaxies have both a regular (or ordered) and random (or turbulent) component[6]. The random component is always strongest, with a mean value of up to 30 μG within the spiral arms (Beck, 2004). It is understood to trace the distribution of cool gas and dust. The regular field, in contrast, is usually weak within the spiral arms. Instead, the

[6]Exact definitions of these terms vary within literature, but we use them here to mean fields with a well-defined direction or otherwise.

regular field is strongest in the regions between the spiral arms, with a mean value of $10 - 15$ μG, and is usually orientated parallel to the adjacent spiral arms (Beck, 2004). The ordered field is also observed to form magnetic arms in almost all galaxies (Wielebinski and Beck, 2005), including in ringed (Chyży and Buta, 2008) and flocculent galaxies (Soida et al., 2002). This indicates that the magnetic fields in galaxies must not follow the gas flow exactly.

Gas flows have a strong impact on magnetic fields, however, with interacting systems showing fields frequently aligned along compression fronts or perpendicular to velocity gradients (Adebahr et al., 2017). Field regularity, defined as $B_{\rm reg}/B_{\rm ran}$, has also been found to be lower in merging systems than in isolated spiral galaxies, with strongly turbulent fields resulting in a peak in magnetic field strength at the time of coalescence, followed by a return to previous lower values (Drzazga et al., 2011). Interactions with a dense intergalactic medium imprints unique signatures onto magnetic fields. For example, virtually all cluster galaxies observed so far show asymmetries in their polarised emission, as outer magnetic fields undergo compression (Vollmer et al., 2013).

The origin of magnetic fields in galaxies is still unclear and many methods to generate initial 'seed' fields have been suggested. Seed fields can be *primordial*, i.e. generated in the early Universe through phase transitions and other nonstandard physics (Durrer and Neronov, 2013; Subramanian, 2016), or may originate during later epochs. In later epochs, plasma instabilities, which produce magnetic fields on kinetic scales (Schlickeiser and Shukla, 2003), and cosmic battery mechanisms, which produce magnetic fields on macro scales, have both been proposed as viable mechanisms. One of the best understood candidates is the Biermann battery process (Biermann, 1950). This, like most other cosmic battery mechanisms, is based on the fact that positively and negatively charged particles in a charge-neutral universe do not have identical properties. In an ionised plasma, the electrons have a much lower inertia than the ions. Consequently, for a given pressure gradient, they are accelerated much more quickly. The subsequent displacement sets up an electric field, which, if it has a curl[7], generates a magnetic field by Faraday's law of induction.

Naturally, this process is fastest in small systems where the temperature and density change rapidly, such as in accretion discs. However, it is also possible for this method to generate fields on cosmological scales, such as in cosmological shock fronts (Kulsrud et al., 1997) and cosmological ionisation fronts (Gnedin et al., 2000). This is useful, as it is still not understood whether magnetic fields started out as an all-pervasive field before being amplified during structure formation (top-down magnetogenesis), or whether it was seeded in small objects, such as in the first stars, before being injected into the proto-galaxies (bottom-up magnetogenesis). In either case, the initial field strength must have initially been much lower than that of present day levels. For

[7]Quantitatively, this happens when the gradients of the electron density and temperature are not parallel.

example, for top-down magnetogenesis, analysis of CMB power spectra data provides an upper limit of ~ 5 nG on a co-moving scale of 1 Mpc (Planck Collaboration, 2016). For bottom-up magnetogenesis, models have only been able to produce field strengths to similar levels (Rees, 2005). In both cases, observations that the intergalactic medium was mostly ionised at $z \approx 7$ provides an upper limit of $2 - 3$ nG for this time frame (Schleicher and Miniati, 2011).

Such field strengths are clearly well below that seen today in galaxies. In order to amplify the field to the strengths seen today, a dynamo, which transfers mechanical energy into magnetic energy, is required. For scales of less than 1 kpc, a turbulent dynamo, driven by supernova shocks and stellar winds, is believed to be able to amplify the magnetic field strength efficiently up to energy equipartition values over time scales of $10^6 - 10^7$ years. Such regions are characterised by a small-scale, random field with a low degree of polarisation (Arshakian et al., 2009). For scales up to 10 kpc, a mean field dynamo is believed to responsible. This dynamo works over time scales of $10^8 - 10^9$ years to produce a large-scale, coherent field with a high degree of polarisation (Shukurov et al., 2006). From a timing argument, it is therefore expected that a small-scale dynamo acts first to rapidly amplify the seed field, before a large-scale dynamo takes over, ordering the field and increasing the field strength at a slower rate. The most promising mechanism to generate and sustain large-scale regular fields from turbulent fields in the ISM of galaxies is the $\alpha - \Omega$ dynamo (Beck et al., 1996). It is based primarily on the combination of the differential rotation (Ω) and the twisting of the gas, and therefore magnetic fields, through the Coriolis effect (α-effect)[8].

The evolution of a magnetic field is governed by the induction equation:

$$\partial_t \mathbf{B} = \nabla \times \mathbf{v} \times \mathbf{B} - \nabla \times (\eta \nabla \times \mathbf{B}) \tag{1.1}$$

where $\mathbf{v}$ is the fluid velocity and η is the magnetic diffusivity. The first term on the right-hand side of Eq. 1.1 is the convective term and the second is the diffusive term. The ratio between these terms is the *magnetic Reynolds number*, which may be approximated as: $\mathcal{R}_\mathrm{m} = vL/\eta$, where v is the root-mean-square turbulent velocity, and L is the typical eddy scale. For astrophysical systems, this number is very large. For galaxies, it is on the order of 10^{18} (Brandenburg and Subramanian, 2005). The diffusive term would thus appear negligible. However, if we neglect η altogether — an approximation known as *ideal MHD* — the magnetic flux threading a fluid element becomes a constant of the motion and the topology of the magnetic field becomes immutable (Vishniac, 2005). The aforementioned $\alpha - \Omega$ dynamo, which involves the conversion of field lines between poloidal and toroidal components, would then not be possible. Neither would magnetic reconnection, which acts as a source of magnetic energy loss and potentially also

[8] A similar approach exploits a cosmic ray-driven Parker instability (Parker, 1992) to provide the large-scale turbulence necessary.

as a source of heating in the galactic halo (Raymond, 1992). Nonetheless, this approximation is frequently a useful starting point for numerical simulations.

Problems involving MHD and hydrodynamics are frequently highly non-linear, outside specific well-known test cases. This results in the need for numerical simulations of the physics. Numerical treatments of MHD are, however, technically difficult, particularly in regards to maintaining the $\nabla \cdot \mathbf{B} = 0$ constraint in simple discretisation schemes (Springel, 2010b; Pakmor and Springel, 2013). For MHD simulations on a galactic scale, such problems are made worse due to the large dynamic range that must be accounted for. In order to resolve the small scale dynamo in such simulations an extremely high resolution is required, whilst in order to understand the cosmological evolution of the magnetic field a very high box size is required.

This resolution problem has meant that many investigations into galactic magnetic fields have ignored the full cosmological context and have instead focused on isolated galaxies. Several of these simulations have shown that, given high enough resolution and strong enough turbulence, initial uniform seed fields can be effectively amplified by a turbulent dynamo (e.g. Dubois and Teyssier, 2010; Wang and Abel, 2009). Virtually all such simulations have used the ideal MHD approximation, although there have been notable exceptions that have used a resistive-MHD treatment (e.g. Hanasz et al., 2009). Idealised simulations necessarily have arbitrarily chosen initial conditions, however, and must exclude the full effects of the galactic environment. This means that the role of hierarchical structure formation in the development of galaxies and their magnetic fields must be ignored.

An investigation into the magnetic fields of galaxies, as considered within their cosmological environment, has been precluded until very recently by the lack of realistic galaxies formed in such simulations (Pakmor et al., 2017). However, better modelling of feedback processes, as well as yet further increased resolution, has mostly solved these issues. There now exists several major galaxy simulation projects that are fully cosmological, high resolution, and contain ideal MHD physics. These include the Auriga project (G17), the Illustris TNG project (Nelson et al., 2019), and the FIRE-2 project (Hopkins et al., 2018). The inclusion of MHD physics was shown to have a limited impact in the FIRE-2 simulations (Hopkins et al., 2019), but the field strength in galaxies at $z = 0$ in these simulations was lower compared to that seen in Auriga and Illustris TNG simulations. The magnetic field in Auriga galaxies was also considered to have a limited impact, but this was because the field took too long to reach equipartition strength in order to affect a galaxy's evolution (Pakmor et al., 2017). Importantly, the magnetic field in Auriga galaxies has been shown to produce realistic Faraday rotation maps (Pakmor et al., 2018). This provides good support for this particular galaxy formation model.

Whilst all galaxies in cosmological simulations will have undergone merging and accretion during their evolution, few of the simulated galaxies from the projects listed above experienced late major mergers, with emphasis being put on studying isolated systems. Furthermore, none of the major mergers that did take place have been seriously investigated in published papers. Having said this, Pakmor et al. (2014) observe, when studying mostly isolated haloes, that a minor merger in one of their cosmological zoom-in simulations is able to boost the magnetic field strength in the galaxy by a factor of two. This result is supported by idealised set-ups, such as that performed by Geng et al. (2012), who also found that magnetic fields were amplified during a merger, with the amplification efficiency dependent on the impact energy of the progenitor galaxies. Further studies based on idealised set-ups have included attempts to create mock radio data for comparison with a real system (Kotarba et al., 2010) and to investigate the saturation of the magnetic field during a merger (Kotarba et al., 2011). However, whilst the mock data shows some qualitative agreement with the synchrotron observations of the Antennae system (NGC4038, NGC4039), the predictive power of the simulation is limited by the idealised set-up. Such drawbacks would be strongly reduced through the use of fully cosmologically-consistent simulations.

Chapter 2

Methodology

In this chapter we introduce: the numerical methods used in our simulations (Section 2.1), the simulation suite itself and definitions of terms used later in the thesis (Section 2.2), and finally, the results of tests performed to check the validity of our methods (Section 3.1).

2.1 Numerical methods

The task presented — namely, investigating the relationship between magnetic fields and the evolution of a galaxy during a major merger — is technically complex. It is therefore important to build upon previously proven work in order to consider our own results to be reliable. Here we introduce the numerical methods used in our simulations and discuss the advantages of these methods relative to competing ones. In particular, we discuss: the concept of cosmological zoom-in simulations (Subsection 2.1.1), the moving-mesh code AREPO and its MHD implementation (Subsections 2.1.2 and 2.1.3, respectively), and the Auriga galaxy formation model (Subsection 2.1.4).

2.1.1 Zoom-in simulations

As previously stated, the physics involved in modelling galaxies is highly non-linear. This means that the problem is best investigated through the use of numerical simulations. As a fine-scale problem, it is necessary to divide the simulation volume into a large number of cells, such that the physical scales required are resolved. However, increasing the number of cells results in a higher computational expense, which quickly becomes unmanageable. The computational expense may be reduced if we focus our attention on the evolution of a single galaxy only. In this case, a significant percentage of the simulated volume becomes dynamically unimportant for the finer

scales. By distinguishing between such regions, we may direct our available computational power to be applied preferentially to the cells that *are* dynamically important.

Dynamically important cells are deemed to be all those that end up within a certain radius of the galaxy, as it exists in the final snapshot. These cells may then be tracked backwards in time to their origin and can be significantly refined in the initial conditions, whilst the rest of the cosmological volume is sampled with coarser resolution. Such a strategy allows the large-scale tidal field originating from the regions far away from the galaxy to still be captured, without having to apply the same increased computational power here. Of course, by increasing the resolution, we also increase the Nyquist frequency — the highest frequency that waves in the power spectra may be added at, such that the power spectra can be unambiguously recovered from the discretised density field. Power may thus be added at higher spatial frequencies in these cells (see e.g. Jenkins, 2010), allowing the formation of previously unresolved small scale structure in the simulation.

The zoom-in technique allows for individual haloes to be studied in great detail, without resorting to idealised set-ups, which may not be cosmologically consistent. Such advantages have been used frequently in the modelling of small-scale baryonic phenomena, such as stellar feedback (Übler et al., 2014), and the modelling of low-mass haloes (Ceverino et al., 2014). The increased dynamic range in the high resolution region also allows for a better resolved galactic structure, with a higher level of resolved physics. The subgrid recipes[1] that remain can in turn be designed in a more physically-motivated fashion, as localisation reduces the need to try and mimic large-scale phenomena at the subgrid level. An example of this may be seen in Sparre and Springel (2016), who showed that the relatively simple, but physically-motivated, Springel and Hernquist (2003) star formation model could produce the phenomena of starbursts, given sufficient resolution.

2.1.2 AREPO

As alluded to in the previous subsection, in order to simulate the laws of nature in code, both time and space must be discretised. This becomes especially problematic when attempting to describe the motion of fluids. Historically, discretising a fluid has been performed in one of two ways: either through a Eulerian or a Lagrangian specification of the flow field. In the Eulerian specification, space is discretised and mass flows in and out of volume elements on a mesh. In the Lagrangian specification, mass is discretised, and fluid elements are represented as particles moving in space. Both of these methods have their own specific advantages and disadvantages.

[1] Algorithms that apply below the grid scale to represent unresolved physics.

Smoothed Particle Hydrodynamics (SPH) is one of the most widely-employed Lagrangian techniques (Monaghan, 1992, 2005). This method has the natural advantage that resolution automatically adjusts to the flow, as well as having other useful properties such as Galilean invariance and exact conservation of energy, linear momentum, and angular momentum. However, in the last few years SPH has come under severe scrutiny and it has been shown to be inaccurate for a series of phenomena relevant to galaxy formation, including the Kelvin-Helmholtz instability (Agertz et al., 2007) and subsonic turbulence (Bauer and Springel, 2012). Some of these issues are solved with the use of Eulerian techniques such as Adaptive Mesh Refinement (AMR). Such codes are also typically faster at converging, with the added advantage that they provide more accurate gradient estimates and do not require an artificial viscosity term. However, these codes also have weaknesses, such as a dependence of advection errors on the bulk velocity. AMR codes have also proved problematic when used to follow the growth of very small haloes (Heitmann et al., 2008).

Such problems may be mostly avoided through the use of the massively-parallel moving-mesh code AREPO (Springel, 2010a; Weinberger et al., 2019). This code uses a set of mesh-generating points to define a Voronoi tessellation, on which a second-order accurate, finite-volume Godunov scheme is formulated. As the mesh points may be moved arbitrarily, they may be set to contain a specific target mass (specified to a tolerance). In this manner they may be moved with the flow, thereby inheriting the advantages of Lagrangian codes, whilst keeping the advantages of mesh-based Eulerian codes. AREPO has also been shown to be considerably more accurate than standard SPH methods when applied to a range of computational fluid dynamic problems (Sijacki et al., 2012). This increased accuracy has been shown to have significant macro effects, with cosmological simulations that were ran with AREPO producing distinctly different results to their SPH counterparts. For example, for an identical physics model and an equal gravity solver, AREPO-based simulations form larger and more well-defined disc galaxies than SPH simulations (Springel, 2012). Furthermore, it has also been shown that AREPO produces the expected Kolmogorov turbulent cascade (Kolmogorov, 1941) for subsonic turbulence, unlike standard SPH models (Bauer and Springel, 2012). The power spectrum of turbulence has a significant impact on its ability to excite the small-scale dynamo, hence this is a very germane result to our investigation.

2.1.3 MHD implementation

In general, the main obstacle to overcome for numerical implementations of MHD is in how to keep divergence errors to a minimum. Whilst the continuum equations of MHD preserve the $\nabla \cdot \mathbf{B} = 0$ condition perfectly given an initial divergence-free field, this is not necessarily the case

for discretised versions of the equations. Worse still, partial differential equation (PDE) solvers are generally unstable to the production of magnetic monopoles. This means that once such fields are produced, they have the tendency to become rapidly larger in any non-trivial MHD flow, rendering the simulation results unphysical (Pakmor et al., 2011). To this end, there have been two major numerical techniques developed to implement MHD in AREPO, with the differences between them to be found mostly in their treatment of divergence errors. In their initial form, these methods are presented in Pakmor et al. (2011) and Mocz et al. (2014), respectively.

In Pakmor et al. (2011), additional terms are added to the equations such that $\nabla \cdot \mathbf{B}$ components are diffused away. In the current version of this technique (Pakmor and Springel, 2013) this is achieved through the use of a so-called Powell 8-wave scheme (Powell et al., 1999). It is, however, also possible to fulfill the divergence constraint by construction through use of 'constrained transport' (CT) methods, as introduced in Evans and Hawley (1988). These methods are able to preserve the $\nabla \cdot \mathbf{B} = 0$ condition to machine precision, but are significantly more complex in nature when applied to unstructured moving-meshes. Mocz et al. (2014) were able to implement a CT MHD scheme in AREPO by replacing the standard finite-volume approach to solving PDEs with a discontinuous Galerkin method.

In comparing both techniques, Mocz et al. (2016) found that whilst both methods gave similar results when applied to cosmological simulations, the Powell method produced more cell-level noise. As resolution became higher, differences between the two methods consequently became stronger. This was seen particularly when simulating an isolated Milky Way-sized disc galaxy. Here, it was observed that magnetic fields in the CT scheme were amplified more slowly than in the Powell scheme and saturated at a lower level. As a result, whilst the magnetic fields in the Powell scheme grew to be dynamically dominant in the central parts of the galaxy, they did not become dominant in the CT scheme[2]. The CT algorithm was also observed to better maintain the topological winding of the magnetic field. Differences were attributed mostly to the increased accuracy afforded by the CT scheme in maintaining $\nabla \cdot \mathbf{B} = 0$.

Despite a weaker ability to fulfill the divergence constraint, the Powell scheme has been shown to be able to accurately replicate a series of MHD phenomena. For example, Pakmor and Springel (2013) compared the linear phase of growth of the magneto-rotational instability (Balbus and Hawley, 1991) produced by this method to that expected analytically, and found good agreement. This instability is believed to be key in allowing matter to be accreted onto a compact object by transporting angular momentum radially. Pakmor et al. (2014) also used this scheme to simulate the formation and evolution of a Milky Way-like galaxy in a cosmological simulation and found

[2]It must, however, be said that the magnetic fields were *not* seen to become dynamically dominant in Pakmor et al. (2017).

evidence of a small-scale dynamo in action, as expected from dynamo theory. This dynamo was then succeeded by amplification due to differential rotation once a gaseous disc had formed[3]. Furthermore, the final magnetic field strength and radial profile produced were similar to those seen observationally. Analysis of galaxies simulated in the Auriga project (G17), which also uses this scheme, produced similar results to those seen above (Pakmor et al., 2017). Finally, Auriga galaxies show Faraday rotation strengths that are broadly consistent with those observed for the Milky Way (Pakmor et al., 2018).

2.1.4 The Auriga galaxy formation model

The Auriga galaxy formation model was introduced in G17 as part of the Auriga project. This project was designed to simulate the formation of galaxies in isolated Milky Way-mass dark matter haloes. This was done by employing the AREPO code in a series of cosmological zoom-in simulations. The formation model has been shown to be able to produce galaxies with appropriate stellar masses, sizes, rotation curves, star formation rates, and metallicities (Grand et al., 2017), as well as finer details such as the correct structural parameters of bars (Blázquez-Calero et al., 2019) and possession of chemically distinct thick and thin discs (Grand et al., 2018).

The model is closely based on the work of Vogelsberger et al. (2013) and Marinacci et al. (2014), but contains significant changes with respect to stellar feedback and the inclusion of the Pakmor and Springel (2013) MHD implementation. Importantly, models for star formation, stellar feedback, and AGN feedback are all physically well-motivated, and parameters do not require re-tuning between resolution levels. Earlier work (e.g. Scannapieco et al., 2012) has shown that this is non-trivial, as many codes are not robust to a change of resolution, with outcomes being particularly dependent on the implementation of the feedback. With this in mind, some of the key properties of this model are listed below.

Gas cells and star particles

Gas may cool via both atomic and metal-line cooling with self-shielding corrections accounted for (Vogelsberger et al., 2013). A spatially uniform UV background field is included, which fully reionises hydrogen by $z \sim 6$ (Faucher-Giguère et al., 2009).

The ISM is described using the Springel and Hernquist (2003) subgrid model. This model treats the star-forming gas as a two-phase medium, with dense, cold clouds embedded in a hot, ambient medium. The phases are assumed to be in continuous pressure equilibrium and are therefore

[3]Note, that as an ideal MHD code, this implementation is not able to simulate a true $\alpha - \Omega$ dynamo due to flux-freezing (see Section 1.4 for details).

governed by an effective equation of state at densities above the threshold particle density for star formation, $n_{\rm s.f.} = 0.13$ cm^{-3}. Above this density, the gas is considered to be 'star-forming' and star particles are formed stochastically according to a probability that scales with the local dynamical time. When star particles are formed, gas mass is converted into stellar mass, with the gas cell either being completely removed or retained with reduced mass based on the target mass for that cell (see Subsection 2.2.1). Magnetic field flux is considered to be locked up in the star particle and is removed with the gas cell when a star particle forms.

Each star particle represents a single stellar population (SSP), which is characterised by an age and metallicity. The distribution of stellar masses contained initially in each SSP is given by a Chabrier IMF (Chabrier, 2003) (see Section 1.2). By calculating the amount of mass leaving the main sequence at each time step, the mass loss and metal yields (H, He, C, N, O, Ne, Mg, Si, Fe) from SNII, SNIa, and AGB stars are calculated. These are distributed among the nearby gas cells using a top-hat kernel, allowing stellar evolution to be determined in a self-consistent manner. Photometric properties of the star particles are provided in the form of mock SDSS broad bands using the catalogues of Bruzual and Charlot (2003).

Stellar feedback

Star-forming gas cells may probabilistically become a site for an SNII event instead of a star particle. This event is modelled by converting the gas cell into a wind particle and launching it in a randomly-chosen direction. As with the formation of star particles, the magnetic field flux is removed with the gas cell during this event. The wind particle is loaded with 40% of the metal mass of the gas cell from which it was created, and is set with a velocity proportional to the local one-dimensional dark matter velocity dispersion (Okamoto et al., 2010). The wind particle then interacts only gravitationally until it reaches a gas cell with $n < 0.05\ n_{\rm s.f.}$ or exceeds the maximum travel time. Here it deposits its mass, metals, momentum and energy, with energy split into equal parts thermal and kinetic. This result is smooth, regular winds that provide non-local feedback between star-forming and non-star-forming gas. These winds become mostly bipolar at late times, as the wind takes the path of least resistance away from the galaxy.

Black hole particles and AGN feedback

Black holes are seeded with a mass of 10^5 M$_\odot$ h^{-1} in FoF groups (see Subsection 2.2.3) with masses greater than 5×10^{10} M$_\odot$ h^{-1} at the position of the most dense gas cell. Following Springel et al. (2005a), black hole particles merge when they come within the smoothing length (see Section 2.2.1) and grow through the accretion of gas. This accretion is described by Eddington-limited Bondi-Hoyle-Lyttleton accretion (see Section 1.2) with an additional term that models radio

mode accretion (see Equation 8 of G17 for the full form[4]).

Feedback from black holes is implemented in both radio and quasar mode. For the quasar mode, thermal energy is injected isotropically into neighbouring gas cells, whilst for radio mode, bubbles of gas are gently heated at locations within the halo, such that their distribution forms an inverse square profile with distance from the black hole. In both cases, energy is injected continuously with a rate given by $\dot{E} = \epsilon_{\rm f}\,\epsilon_{\rm r}\,\dot{M}_{\rm BH}\,c^2$, where $\epsilon_{\rm r}$ and $\epsilon_{\rm f}$ are efficiency parameters equal to 0.2 and 0.07, respectively, and $\dot{M}_{\rm BH}$ is the rate that gas is being accreted onto the black hole.

2.2 Simulations

During this research, we ran a set of twelve high-resolution cosmological zoom-in simulations, with magnetohydrodynamical and hydrodynamical simulations performed from common initial condition files. Resolution, choice of parameters, and set-up are discussed in Subsection 2.2.1. The naming of the simulations is discussed in Subsection 2.2.2. The definitions of 'halo' and 'galaxy', within the context of our analysis, are discussed in Subsection 2.2.3. The coordinate system used during our analysis is defined in Subsection 2.2.4. Finally, a brief description of the mergers analysed is given in Subsection 2.2.5.

2.2.1 Set-up and initial conditions

Initial conditions for our simulations are the same as those presented in Sparre and Springel (2016). These were created by selecting galaxies from the hydrodynamic cosmological simulation *Illustris* (Genel et al., 2014; Vogelsberger et al., 2014a,b) that had undergone a major merger between $1 < z < 0.5$ but had relaxed by $z = 0$[5]. For four such galaxies, zoom initial conditions were created using a modified version of the *N-GenIC* code (Springel, 2015) for a periodic box with sides 75 Mpc/h (co-moving). This code uses the Zel'Dovich approximation (Zel'Dovich, 1970) to create Gaussian random fields with a prescribed power spectrum (see Section 1.1). The power spectrum follows from the cosmological parameters used. Naturally, we use the WMAP-9 (Hinshaw et al., 2013) parameters, as used in the initial Illustris run. These are: $\Omega_m = 0.2726$, $\Omega_b = 0.0456$, $\Omega_\Lambda = 0.7274$, and $H_0 = 100\ h$ km s^{-1} Mpc^{-1} with $h = 0.704$.

Dark matter particles were given a high resolution within a roughly spherical region around the target galaxy. A shell of standard resolution particles with resolution close to the original

[4]The radio mode accretion term is based on relations presented in Nulsen and Fabian (2000).
[5]See Sparre and Springel (2016) for a full list of selection criteria.

Illustris run then followed, with low resolution particles filling the remaining volume. Dark matter particles were split into dark matter particle and gas cell pairs. Mass was then placed in gas cells according to the expected cosmological baryon fraction (i.e. Ω_b/Ω_m). The gas cells were displaced from the dark matter particles, such that the centre of mass for each particle-cell pair was left unchanged. The mean distance between dark matter particles and mesh-generating points was also maximised to avoid artificial pairing effects. This resulted in a computationally efficient simulation that also maintained the correct representation of external effects such as mass infall and the cosmological tidal field.

The resolution of a dark matter particle is defined by the *zoom factor*, where 1 is equal to standard resolution. We have run simulations with zoom factors 1, 2, and 3 (see Section 2.2.2), which correspond to mass resolutions of 1.4, 11.4, and 38.5 times finer than in the original Illustris simulation[6]. The zoom factor is tied to the finest dark matter mass resolution by the following equation:

$$m_{\rm dm} = \left(\frac{1820}{2048 \times \text{`zoom factor'}}\right)^3 \times 6.299 \times 10^6 \ \mathrm{M}_\odot \tag{2.1}$$

where 1820/2048 is the ratio between the number of dark matter particles per box length in Illustris relative to our standard resolution, and the remaining numerical factor is the finest dark matter resolution in Illustris. The highest dark matter mass resolution reached in our simulations is therefore $\sim 1.6 \times 10^5$ $\mathrm{M}_\odot$, whilst the highest baryon mass resolution reached is $\sim 2.7 \times 10^4$ $\mathrm{M}_\odot$.

Following Springel (2005) and Price and Monaghan (2007), we choose the softening length to be $\sim 1/40$ of the average particle spacing in the initial conditions, i.e.:

$$\epsilon \approx \frac{L}{40 \times 2048 \times \text{`zoom factor'}}$$

where L is the box length. The softening length is a co-moving length until $z = 1$, at which point it is frozen in physical units, thereby maintaining the same resolution in the simulation for $z < 1$. For our highest resolution simulations, the softening length is therefore 0.3 kpc at $z = 0$. Calculating the softening length in this manner prevents unrealistic two-body interactions that would violate the collisionless nature of the system at early times, whilst still allowing small-scale structure to continue to form at late-times (see e.g. Power et al., 2003). As gas cells vary strongly in density, their softening length is also scaled by the mean radius of the cell. Such cells have a minimum softening length of ϵ, as defined previously, and a maximum softening length of 1.1 kpc.

As previously mentioned, energy from AGN feedback is injected into neighbouring gas cells.

[6]For reference, Level 4 and Level 3 Auriga simulations are $\sim$ 21 and $\sim$ 157 times better than the original Illustris resolution.

As resolution increases, the number of cells neighbouring the black hole increases as well. We therefore increase the *black hole neighbours* parameter with resolution. Ideally, this number would increase with the third power of the zoom factor (i.e. proportional to the increased mass resolution) but this soon becomes extremely computationally expensive. As a compromise, we double the number of neighbours instead for each increased level of resolution. This compromise may be a factor in the slight, but systematic, increase in star formation rate seen for higher resolution simulations, as observed in Sparre and Springel (2016) and G17 (see Subsection 3.1.2).

Finally, a homogeneous co-moving seed field of 10^{-14} G is seeded throughout the simulated volume at $z = 127$, orientated along the z-direction. This is equivalent to a physical strength of 1×10^{-10} G for this redshift[7]. Such a choice is essentially arbitrary as, for a broad range of values, all traces of the initial field strength and configuration are erased by an exponential dynamo in collapsed haloes (Pakmor et al., 2014). Our choice of initial field strength has also been shown to produce magnetic fields are dynamically irrelevant outside of collapsed haloes (Marinacci and Vogelsberger, 2016).

Following this set-up, the Auriga galaxy formation model is evolved from a redshift of $z = 127$ to $z = 0$, producing 136 snapshots. Gas cells, star and wind particles, black hole particles, and dark matter particles are all tracked continuously. Gas cells are kept within a factor of two of the mean cell mass, with the mesh being refined and de-refined as required. We also include *tracer particles* (Genel et al., 2013), which are used in some of our analysis (see e.g. Section 3.5.3). These are explained in detail in the apposite section.

2.2.2 Naming

Simulation names are given in the format *AAAA-BC*, where *AAAA* is the four-digit friends-of-friends group number in Illustris for the halo containing the galaxy at $z = 0$ (see Subsection 2.2.3 and Nelson et al., 2015), B is the 'zoom factor' of the simulation (see Eq. 2.1), and C is the letter 'M' or 'H', indicating whether the simulation included magnetohydrodynamic (MHD) or hydrodynamical (HD) physics, respectively. This last letter is sometimes referred to as the simulation *suffix* during this thesis, with the *AAAA-B* section of the simulation name is referred to as the simulation *prefix*. By definition, simulations that have the same prefix were run from the same initial conditions file. During this thesis, we will sometimes use the simulation name as a synecdoche for the main galaxy in that simulation, as defined in the following subsection.

In total, the following simulations were run:

[7] 1 co-moving Gauss $= a^2/h$ physical Gauss, where a is the scale factor.

MHD simulations:	1330-1M	1330-2M	1330-3M	1349-3M	1526-3M	1605-3M
HD simulations:	1330-1H	1330-2H	1330-3H	1349-3H	1526-3H	1605-3H

As may be seen, eight of the twelve simulations were ran at the highest resolution, whilst four were run at lower resolutions. The lower resolution runs have been used for convergence tests in order to validate our results (see Section 3.1).

2.2.3 Galaxy tracking

Without discrete edges, the boundary of a cosmological structure is necessarily somewhat arbitrarily defined. This is especially true during mergers, and many algorithms have been created and tested in an attempt to solve this problem (see e.g. Behroozi et al., 2015). In this study, we use the standard friends-of-friends (FoF) approach (Davis et al., 1985) to identify haloes, followed by use of the SUBFIND algorithm (Springel et al., 2001) to identify 'subhaloes'. Such subhaloes are considered to have a one-to-one correspondence with the location of galaxies.

An FoF group is produced by linking all particle pairs separated by less than a fraction b of the mean interparticle separation. In our simulations, this algorithm is applied to dark matter particles, using a value of $b = 0.2$, with groups only kept if they contain at least 32 particles. Baryonic elements are then assigned to the same FoF group as their nearest dark matter particle. Such an FoF group is defined as a *halo*, and is then searched for further substructure.

SUBFIND defines substructures within a halo as locally overdense, gravitationally bound groups of particles. In the version written for AREPO, a density field is calculated for all particles and gas cells using an adaptive smoothing length. Any locally overdense region within this field is then considered to be a *substructure candidate*. The boundary of this substructure candidate is determined by the first isodensity contour that passes through a saddle point of the density field or, equivalently, the boundary of two separate substructure candidates. Once all substructure candidates have been located, they are subjected to an iterative unbinding procedure with a tree-based calculation of the potential. The result is the decomposition of the FoF group into a set of disjoint self-bound *subhaloes*.

Whilst FoF haloes may form tenuous bridges during galaxy interactions, and hence be identified as a single structure, the criteria of 'self-boundness' means that structure identified by SUBFIND remains essentially distinct until coalescence. This property makes the algorithm particularly useful for the investigation of galaxy mergers. The main and secondary galaxy involved in the merger were therefore identified as the first and second most massive subhaloes at $z = 0.93$, respectively, as during this period both galaxies are relatively isolated. The time of merger is

considered to be snapshot at which the galaxies have finally coalesced. After this time, the progenitors have the same descendants in the merger tree (see Sparre and Springel, 2016).

To track a galaxy between snapshots, it is a case of identifying the subhalo that shows the most consistent trajectory to a previously identified one. In practise, this provides the same results as identifying the subhalo that contains the same black hole particle as the previous subhalo. Such a result is expected, as earlier work has shown that reliable merger trees can be constructed by tracking only the 10-20 most bound particles of each subhalo (Wetzel et al., 2009; Rodriguez-Gomez et al., 2015). The differences that do occur are described in Section A.1.

2.2.4 Galactic coordinates

In our simulations, the *centre* of the galaxy is defined as the position of the particle in the subhalo with the lowest gravitational potential energy (see Subsection 2.2.3). Galactocentric coordinates are then produced by subtracting these coordinates from the general simulation coordinates that map the periodic box. These new galactocentric coordinates are then rotated such that the z-axis is aligned with the stellar angular momentum vector for the disc. The stellar angular momentum vector for the disc is calculated using the formula:

$$\mathbf{L} = \sum_i \mathbf{r}_i \times m_i \mathbf{v}_i$$

where i refers to a star particle, $\mathbf{r}$ is its galactocentric position, m is its mass, and $\mathbf{v}$ is its galactocentric velocity. To select star particles that lie preferentially within the disc, we select only star particles that are less than 3 Gyr old. In order to prevent excessive disruption due to interactions with other subhaloes, only star particles within 10% of the distance $R_{200,\mathrm{crit}}$ of the galaxy are included[8]. $R_{200,\mathrm{crit}}$, in turn, is defined as the radius of a sphere centered on the galaxy, such that its mean density is 200 times the critical density of the Universe at the time the galaxy is considered.

In order to rotate the system accordingly, a skew-symmetric matrix is created through the formula:

$$M = I_3 \times \frac{\mathbf{L}}{|\mathbf{L}|}$$

where I_3 is the three-dimensional identity matrix. This matrix is transformed into a rotation matrix using the formula:

$$R = \exp(M\theta)$$

where the angle, θ, is defined as the angle between $\mathbf{L}$ and the z-axis. This is then applied to

[8]This region is known to roughly encompass the galactic disc (Deason et al., 2011).

all spatial coordinates used. These coordinates are given in a cartesian or a cylindrical basis depending on the analysis being performed.

Naturally, this orientation procedure becomes unreliable when the galaxy does not show a clear disc, or when external galaxies are too close to the disc (i.e. within 10% of $R_{200,\mathrm{crit}}$). In practice, this is rarely an issue, as a) properties that apply to the subhalo as a whole, such as the total star formation in the subhalo, are unaffected by a change of coordinates, and b) most analysis is performed before and after the merger when the galaxies are isolated and show clear discs. When this is not the case, it is discussed during the appropriate section.

2.2.5 Description of the mergers

Whilst the main merger in each simulation presented here is considered to be 'major' — the stellar mass ratio of the two participating galaxies in each simulation is within the range $1.0 \lesssim M_{*,1}/M_{*,2} \lesssim 1.5$ — the trajectories and number of interacting galaxies involved in each simulation varies. It is therefore of interest to give a brief overview of the qualitative merger history for each simulation, as this helps to explain the difference in the results seen between them. We create such a merger history by visually inspecting mock SDSS images, created for each snapshot through a process described in Subsection 2.1.1. We do not show these here due to space constraints, but summarise the main points instead. Roughly speaking, we may separate our merger scenarios into inspiralling (prefixes 1330 and 1526) and head-on (prefixes 1349 and 1605). The main details of each scenario are then as follows:

- Simulations with the prefix 1330 show a major merger, with an initial fly-past followed by a protracted period of inspiralling. The merger remnant also experience a minor merger, which coalesces at a lookback time of ∼4 Gyr. The galaxies undergo a series of minor tidal interactions at late times.
- Simulations with the prefix 1526 show a minor merger coalescing shortly after the major merger. The remnant experiences flybys from small galaxies after the merger, as well as having a relative major tidal interaction at a lookback time of ~ 2.5 Gyr. Both the fly-bys and the tidal interaction have smaller impact parameters in the hydrodynamic simulation.
- Simulations with the prefix 1349 show a very complex merger, with 7 galaxies of significant mass within 100 kpc of the main galaxy at the time of the major merger. Many of these coalesce with the main galaxy immediately following. The merger remnant then experiences relative isolation until a fly-past at a lookback time of ~ 1 Gyr, which has a relatively large impact parameter.

- Simulations with the prefix 1605 show a highly energetic, head-on merger. Both simulations also show a minor merger taking place at roughly the same time, as well as a small inspiralling galaxy, which passes the main galaxy at its closest points at lookback times of around 5, 1.8, and 0.1 Gyr.

The dynamical progress of each merger may also be well understood by examining the visual time series shown in Fig. 1 in Sparre and Springel (2017). The trajectories may be similarly well understood through Fig. 6 and Fig. 7 of Sparre and Springel (2016). The simulations presented in these papers were run from identical initial conditions and used similar physics models. They hence show similar trajectories and dynamical evolutions.

Chapter 3

Analysis

We separate our analysis in the following chapter into: validation of the methods and simulations (Section 3.1), global properties (Section 3.2), the effects of increased resolution on morphology (Section 3.3), quantification of the observed effects (Section 3.4), evidence for a potential mechanism (Section 3.5), and the impact of the merger on the magnetic field structure (Section 3.6).

3.1 Validation of methods and simulations

Before we investigate the impact of including MHD physics in our merger simulations, it is important to make sure that our simulations are: a) consistent with what is expected under ΛCDM cosmology, and b) numerically convergent. To this end, we present a series of validation tests: convergence of the bound dark matter mass of the galaxies between physics models (Subsection 3.1.1), appropriate values for the $M_* - M_h$ relation over all resolution levels (Subsection 3.1.2), convergence of the star formation rate between resolution levels (Subsection 3.1.3), and an appropriate magnetic field strength as a function of density (Subsection 3.1.4).

3.1.1 Dark matter mass evolution

As discussed at length in Section 1.1, the large-scale structure of the Universe is set predominantly by its dark matter distribution. Dark matter interacts only gravitationally in our simulations, and so we should not see any significant differences to its distribution and evolution between physics models. We check this by considering the evolution of the bound dark matter mass for the main galaxy in each simulation. The dark matter mass bound to a galaxy is identified by the SUBFIND algorithm, as described in Subsection 2.2.3. This quantity is similar, but not totally

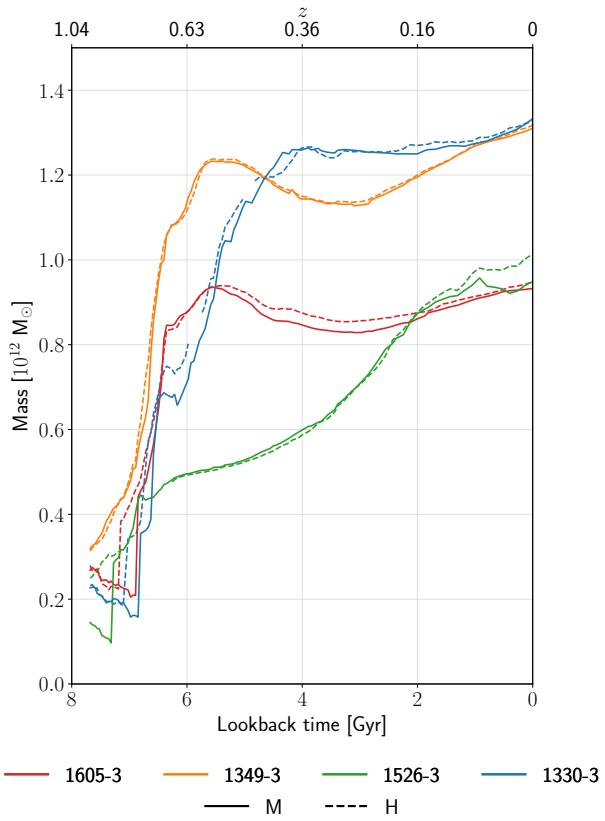

Figure 3.1: Total bound dark matter mass for the main galaxy (as defined in Section 2.2.3) in each of our highest resolution simulations as a function of time. Colour indicates the prefix of the simulation name, whilst the linestyle indicates the suffix; i.e. inclusion of either MHD or hydrodynamic physics. Data for simulation 1526-3H between 7.11 Gyr and 6.35 Gyr has been omitted due to identification of the subhalo by SUBFIND being inconsistent with our definition between these times. Excluding this, lines of the same colour show an almost identical evolution with a mean difference of less than 5%, as expected from large-scale structure theory.

equivalent, to the M_{200} parameter commonly used in observational literature[1]. The advantage of using the bound dark matter mass over M_{200} is that it is better at keeping structures distinct during mergers and tidal interactions (see Subsection 2.2.3 for more detail). It is therefore a more sensitive characterisation of the large-scale structure evolution. We may also use this parameter to check that the galaxies in each pair of MHD and hydrodynamic simulations are undergoing the same tidal processes at roughly the same times. Such interactions should be predominately set by the large-scale structure, with allowances given for baryonic influence at close range.

The evolution of the bound dark matter mass is shown for the main galaxy in each of our highest resolution simulations in Fig. 3.1. The dark matter mass evolution is clearly extremely similar

[1] M_{200} is the mass contained within a sphere, such that the interior density of that sphere is 200 times the critical density of the Universe.

between physics models. Indeed, the mean difference over all snapshots between MHD and hydrodynamic simulations is less than 5%. This is very close, especially given the highly dynamic nature of the system and the sensitivity of the bound mass parameter. This shows that our simulations are well-converged. The missing line segments for simulation 1330-3H are due to a corruption of the subhalo catalogues at these snapshots. The subhalo identification process is fully independent of the evolution of the simulation, however, and so does not affect the particle dynamics. The missing line segments for 1526-3H between 7.11 Gyr and 6.35 Gyr are due to SUBFIND briefly allocating extra mass to the merging galaxy, leading to a non-continuous mass evolution for the main galaxy. This is inconsistent with our visual-based galaxy tracking method (as defined in Subsection 2.2.3) and is a result of the fact that SUBFIND identifies subhaloes independently at each snapshot, rather than using information about the dynamics and trajectories of particles in other snapshots, as we do.

The time of the merger in each simulation pair is evident by the rapid increase in mass. This increase is often somewhat discontinuous at the initial stages of the merger, as SUBFIND reallocates mass between interacting subhaloes. A discrete jump in mass is, however, typical of subhalo-finders during mergers (Behroozi et al., 2015). For simulations with the prefix 1349-3 and 1605-3, most of the growth in mass takes place within ± 1 Gyr of the major merger, which occurs at $t_{\rm lookback} \approx 6.5$ Gyr. The growth process takes a little longer (from $t_{\rm lookback} \approx 7$ - 4 Gyr) for simulations with the prefix 1330-3, as the galaxies inspiral and therefore take longer to coalesce. This is seen by the two clear periods of mass growth, with dark matter being transferred from the merging galaxy to the main galaxy during the initial fly-bys. In the most head-on mergers — i.e. in simulations with prefix 1349-3 or 1605-3 — the bound dark matter mass dips slightly after the merger before recovering. This is interpreted to be mostly a result of the destruction and re-growth of structure in the merger remnant[2] and the subsequent reallocation of matter by SUBFIND. The ejection of matter as the remnant relaxes may, however, also play a role (Carucci et al., 2014).

After the merger, the total bound dark matter mass stays relatively constant in every simulation except in those with prefix 1526-3, where there is a continual increase in the bound dark matter mass. This starts at a fairly gradual rate, in-line with the increases seen for other galaxies, but accelerates after a lookback time of $\sim$4 Gyr. A significant percentage of this effect may be attributed to the fact that another subhalo enters the system around this time. The differences seen after ~ 1 Gyr are also interpreted as being a result of the tidal interaction that takes place then. It is worth noting that the the galaxies in the 1526-3 simulations evolve slightly differently

[2]See e.g. Fig. 3.14 for comparison.

from other pairs, as will be made clear in later analysis[3]. At least some of this may be attributed to the difference in accretion history seen here. Regardless of evolution, by $z = 0$ each galaxy has a total bound dark matter mass roughly within 1σ of the virial mass of the Milky Way (Kafle et al., 2014).

3.1.2 Stellar mass and halo mass evolution

Each halo should fit the so-called *stellar mass - halo mass* relation. As explained in Section 1.2, for Milky Way-size haloes this relation takes a value of $M_\star/M_\mathrm{h} \approx 3 - 5\%$. We also expect to see a rough convergence of both the halo and stellar masses between resolution levels, assuming that the galaxy formation model is sensitive to the choice of physical parameters rather than the numerical implementation[4]. To this end, in Fig. 3.2 we show the total bound mass and bound stellar mass for the main galaxy in each simulation with prefix 1330.

Once again, at the time of the merger we see a sharp increase in the total bound mass. The exact time of this increase differs between resolution levels as SUBFIND apportions mass between subhaloes differently. This is expected as the particle dynamics at this time are highly non-linear, and the separation of structures becomes more difficult. This is unfortunately a problem of most subhalo finders that only use single snapshots to identify structure with (Behroozi et al., 2015). The reapportioning of matter by SUBFIND is also seen for the low and medium resolution hydrodynamic simulations at ~ 6 Gyr. This is the manner of discontinuity that affects 1526-3H between 7.11 Gyr and 6.35 Gyr, as described in Subsection 3.1.1. Despite these differences, the ratio between the standard deviation and the mean at $z = 0$ is only $\sim 2\%$. This shows that the halo mass is very well converged between resolution.

The total bound stellar mass is also well converged, but not as well as the halo mass. For each level of increased resolution, we see an increase of $\sim 25\%$ in stellar mass. The result is that the highest resolution simulations have a $M_\star - M_\mathrm{h}$ ratio of $\sim 8\%$. This is above the values observed for Milky Way-size haloes, but is still within a factor of two of the target values, which is considered acceptable. The increase in stellar mass is perhaps not too surprising, as both Sparre and Springel (2016) and G17 also saw a slight, but systematic, increase in star formation with resolution for versions of this galaxy formation model. In G17, it was found that the extra star particles were created almost exclusively within the central 5 kpc of the galaxy. This has been previously suggested to be a result of the highly non-linear and interconnected AGN and

[3] An especially clear example is Fig. 3.7.

[4] As discussed in Subsection 2.1.4, convergence between resolution levels is notoriously difficult to achieve in galaxy formation models, especially for stellar and AGN feedback implementations.

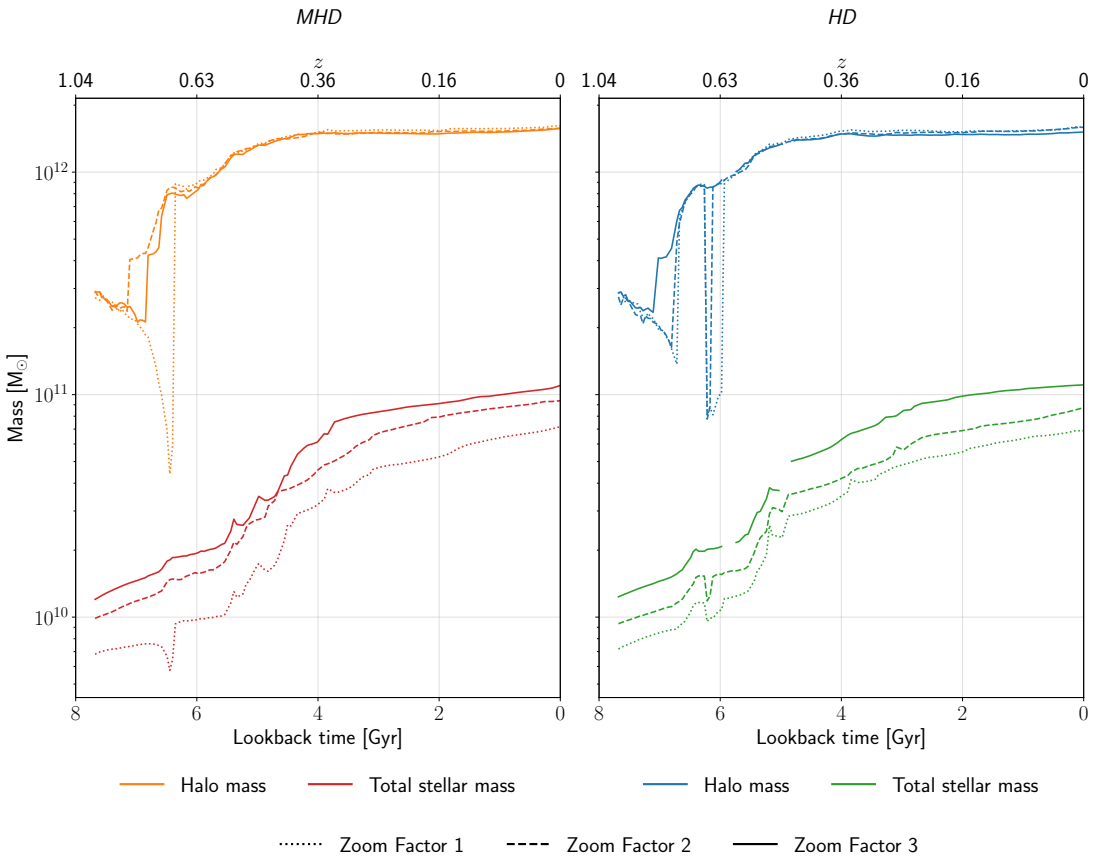

Figure 3.2: Total bound halo and stellar mass for the main galaxy in each simulation (as defined in Section 2.2.3) as a function of time. All data comes from simulations that have the prefix 1330. Simulations shown in the left-hand panel included MHD physics, whilst those in the right-hand panel only included hydrodynamic physics. Linestyle indicates simulation resolution (see Section 2.2.2 for details). In general, the halo mass evolution is very well converged, with the mass at $z = 0$ showing a coefficient of variation for all simulations of only ∼2%. Total stellar mass, by contrast, increases on average by ∼25% with each increase in resolution level. During the merger of the two main haloes in each simulation (at ∼6 Gyr), identification by SUBFIND is not necessarily consistent with our method, resulting in some of the observed discontinuities. All simulations stay generally within the M_*-M_h relation, although this quantity ends up slightly too high in the best resolution runs.

stellar feedback loops active in this region (Marinacci et al., 2014).

Outside of this effect, the stellar mass shows a very similar evolution between resolution levels. Some mild fluctuations may be seen during the early stages of the merger, which are again a result of the apportioning of mass by SUBFIND at this time. The remaining mass increases are almost exclusively due to merger-induced starbursts and standard stellar evolution. It is reassuring that our simulated galaxies are broadly consistent with the $M_\star - M_h$ relation, as this indicates that our galaxies resemble real ones.

3.1.3 Star formation history as a function of resolution

Whilst a slight increase in star formation is allowable between resolution levels, the star formation history (SFH) should still show the same general trends if the simulations are converged. That is to say, that the peaks in star formation should take place at roughly the same times, and that they should be roughly proportional to one another. We check this for the main galaxy in all simulations that have the prefix 1330 and present our results in Fig. 3.3. In the top two rows, we show the SFH for MHD and hydrodynamic simulations, respectively. In the bottom row, we show the proper distance between the centres of the main and merging galaxies (as defined in Subsection 2.2.4). We use this distance as a proxy for the merger progress.

To create the star formation history, we select all star particles that are within 10% of $R_{200,\mathrm{crit}}$[5] of the centre of the main galaxy at $z = 0$. We then display the initial masses of these star particles, binned by their formation time, with bin widths equal to 30 Myr. We find this bin width provides adequate time resolution, without resulting in the plot becoming dominated by stochastic noise[6]. A minor disadvantage of this method is that we neglect star formation that immediately results in SNII, as well as excluding stars that have left the galaxy after formation. This method also include effects from later tidal interactions. In practise, however, these factors have a negligible impact on the final result. The star formation history is therefore dominated by that of the two main galaxies, and hence by the merger event. A similar result would have been given by following the average SFR of the main galaxy at each snapshot. We choose this method instead, however, as it is independent of any galaxy tracking. This means that the effects we see are dependent on the resolution, and not on SUBFIND.

Inspecting the figure, we see that the star formation rates are systematically higher for increased resolution until the merger is at an advanced stage. The timing of the various peaks in the star formation before this point are also remarkably similar. As the galaxies coalesce, the star formation rate takes on a more nonlinear relationship with resolution. This is especially the case for the simulations that included MHD physics. One of the reasons behind this may be the rate at which the merger progresses. At first, the distance between the galaxies decreases at essentially the same rate for every simulation, as these dynamics are dominated by the gravitational potential set up by the large-scale structure. As the galaxies get closer to one another, the orbits begin to be affected by baryonic physics. This results in minor deviations after the first pass which, due to the non-linearity of N-body problems, results in a spread in the time of final coalescence[7].

[5] See Subsection 2.2.4 for a definition.

[6] Star formation between time steps is probabilistic, as explained in Subsection 2.1.4

[7] The deviation in merger progress is especially noticeable for the highest resolution MHD simulation, which coalesces significantly faster than the others. This effect will be seen to some extent in all of our highest resolution

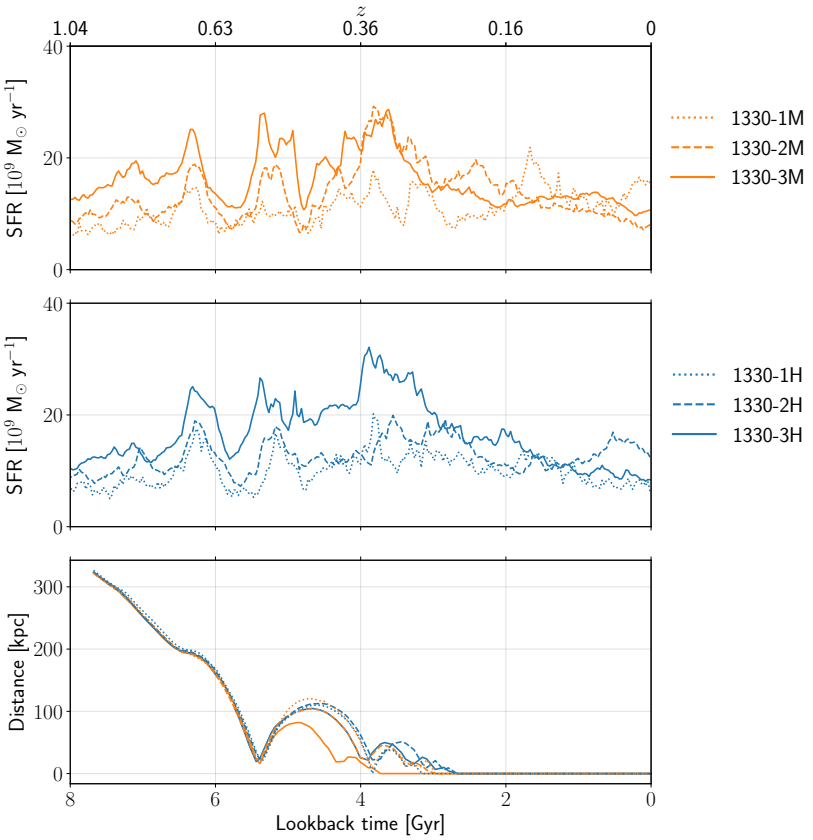

Figure 3.3: *Top two panels:* Star formation history for the main galaxy (as defined in Section 2.2.3) for simulations that included MHD (top) and those that only included hydrodynamic physics (bottom). Each point shows the mean star formation rate (SFR) during a period of ±15 Myr. *Bottom panel:* Proper distance between the centres of the galaxies involved in the major merger of that simulation (as defined in Section 2.2.4). Colours and linestyles follow from the upper panels. Star formation is systematically higher for higher resolution in both sets of simulations but shows the same general trend before the merger event. After the merger, the star formation takes on a more non-linear relationship with simulation resolution. This is especially the case for simulations that included MHD physics. As the main galaxy in each simulation is allowed to relax, the star formation rate begins to converge again.

The difference in orbits results in gas being brought into the centre of the galaxy at different times. As mentioned earlier, the star formation mechanisms at the centre of the galaxy are particularly sensitive to such details. We therefore see slightly different peak star formation rates during this time. As the star formation rates drop to lower values again, they also begin to converge again. Considering these effects, we must conclude that in general the shape of the star formation history is well recovered for all resolution levels, and that our simulations are indeed broadly converged.

simulations and will be discussed in more detail later (see Subsection 3.2.1).

3.1.4 Magnetic field strength as a function of density

Whilst convergence is important, it is equally important that our MHD simulations are producing appropriate magnetic field strengths. Naturally, the magnetic fields will have no significant impact if their strength is too low. Correspondingly, the impact of including MHD physics could be unrealistically high if the field strengths are too high. Following Dolag et al. (2005) and Marinacci et al. (2018b), in Fig. 3.4 we plot the median magnetic field strength as a function of density for simulation 1330-3M at $z = 0$. The dark and light gray shaded areas indicate the 1σ and 2σ deviation from this relation, respectively. The median is plotted for gas density bins of 0.1 dex width. All cells within a radius $6 \times R_{200,\mathrm{crit}}$ (approximately 1.4 Mpc) of the main galaxy were used to calculate the data. This is outside the region covered by our high resolution cells, which ends at approximately $3 \times R_{200,\mathrm{crit}}$. This somewhat aggressive radial cut is made to reach the lowest density values. The inclusion of lower resolution cells is the cause of the small dip in the magnetic field strength at densities of $\sim 10^{-29}$ g cm^{-3}, as well as producing most of the scatter below the median at densities lower than this. Correspondingly, the high resolution cells provide the scatter above the median at these low densities. Towards the very end, the scatter is mostly a result of low-number statistics, as few cells show densities so low.

The dashed black line has a gradient of $\rho^{2/3}$ and shows the density scaling of the magnetic field strength as expected in the case of magnetic flux conservation. This is the relation we would see if the magnetic field strength were amplified purely by isotropic compression due to the collapse of the gas (Heitsch et al., 2004). Instead, we see a rapid increase in the magnetic field strength to a magnitude at least 5 orders higher than that expected from adiabatic compression alone. This indicates that shearing and turbulent processes in the simulation have also worked to amplify the field (Dolag et al., 1999; Marinacci et al., 2018a). The gradient of the median trend above 10^{-28} g cm^{-3} follows a relation of $\mathrm{B} \sim \rho^{1/2}$. Interestingly, this is what is expected for self-gravitating, magnetically sub-critical clouds (Heitsch et al., 2004). The vertical dotted line in the figure indicates the minimum density of all star-forming gas cells in simulation 1330-3M at $z = 0$. This shows us that the magnetic field strength in star-forming gas cells is typically between 5 and 40 μG. The average for the whole disc is towards the lower end of this, whilst denser regions such as the centre and the spiral arms of the galaxy will have higher values, as expected observationally (see Section 1.4).

We compare our results with data available for other cosmological simulations. The solid green line in Fig. 3.4 shows the median magnetic field strength as a function of density for the simulation *Au 6* from the Auriga project, as initially presented in G17[8]. The solid blue line shows

[8]The simulation data for this galaxy was provided by Rüdiger Pakmor.

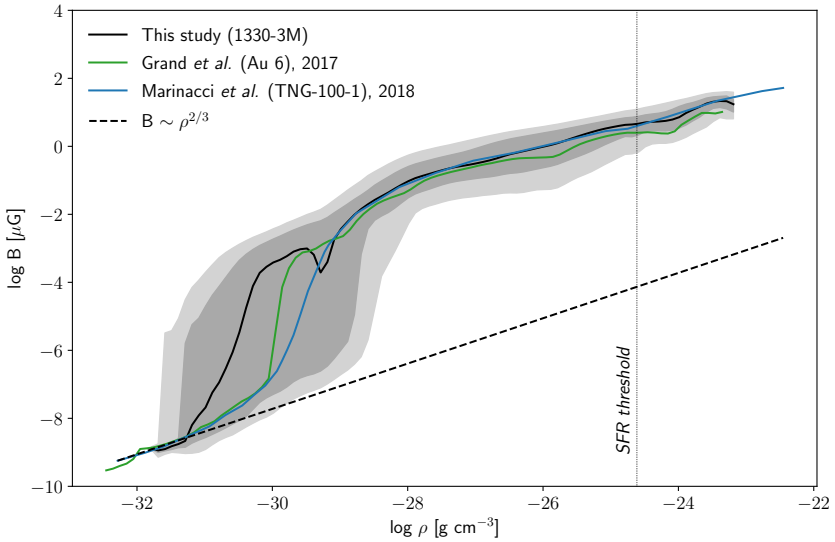

Figure 3.4: Median magnetic field strength as a function of density at $z = 0$ for the simulations (shown in brackets) presented in the legend (top left). The dashed black line has a gradient of $\rho^{2/3}$ and shows the density scaling of the magnetic field strength as expected in the case of magnetic flux conservation. The dark (light) gray shaded areas indicate the 1σ (2σ) deviation from the median for simulation 1330-3M. The vertical dotted line indicates the minimum density of all star-forming gas cells in this simulation at $z = 0$. Our simulations are completely consistent with those done by G17 and Marinacci et al. (2018b). This is expected as these simulations also use the same MHD implementation. Higher magnetic field strengths at lower densities for these simulations are a result of increased resolution and the subsequent ability to resolve the turbulent dynamo at smaller scales.

the same relation for the simulation *TNG-100-1*, as presented in Marinacci et al. (2018b)[9]. The origin of the higher density gas in this simulation is unclear. However, it is likely to result from the fact that this data is taken for the whole simulation volume rather than for one halo. Both of these simulations employ the same MHD implementation as we do, but there are minor differences in the galaxy formation model. More significantly, there are large differences in the mass resolution. The TNG-100-1 simulation has a dark matter mass resolution approximately $31\times$ lower than our highest resolution simulations, whilst Au-6 has a dark matter mass resolution that is $\sim 1.8\times$ lower. This gap in resolution is the most likely reason behind the differences seen between the relations at low densities. All three simulations attempt to keep the gas cells within a target mass. For higher mass resolutions, this target mass is lower and hence so are cell sizes. This means that shear and turbulent effects may be resolved at lower densities. Even in this region, however, all lines lie within 1σ of another. We may therefore conclude that the magnetic field strength seen in our simulation is in very good agreement with that seen in G17 and Marinacci et al. (2018a). Our MHD implementation is hence considered to be representative of what is state of the art in the field of cosmological galaxy formation simulations.

[9]This was converted from Fig. 3 of this paper using a factor of $\rho_b = 4.189\times10^{-31}$ g cm^{-3}, as given in Planck Collaboration (2016).

3.2 Galaxy properties

In this section, we investigate the impact of magnetic fields on the global properties of the simulated galaxies. In particular, we investigate the effect of including MHD physics on: the star formation history (Subsection 3.2.1); the evolution of the stellar mass fraction in the disc (Subsection 3.2.2); and the evolution of the total bound gas and stellar mass (Subsection 3.2.3). We conclude that the addition of MHD physics does not result in a significant impact on galactic global properties, and may even result in *less* efficient feedback, as measured through the evolution of the bound gas mass.

3.2.1 Star formation rate as a function of merger progress

As discussed in Section 1.3, mergers can have a dramatic impact on the star formation rates in a galaxy. This, in turn, affects the morphological evolution of the galaxy. Some previous simulations have suggested that sufficiently high magnetic pressures can launch a galactic wind (e.g Steinwandel et al., 2019). This wind would eject cold gas from the galaxy, thereby reducing the star formation rate. On the other hand, magnetic pressure could also act to support increased gas densities or otherwise influence gas dynamics. This could possibly impact the timing and duration of any merger-induced starbursts. To investigate these effects, we plot the star formation rate as a function of time for each of our highest resolution simulations in Fig. 3.5. As in Fig. 3.3, we also show the distance between the centres of the main and merging galaxies in the bottom row, and use this as a proxy for the merger progress. Broadly speaking, the galaxies shown on the left-hand side of the figure, being direct collisions, undergo more energetic mergers than those on the right-hand side (see Subsection 2.2.5). In each panel, solid lines indicate simulations that included MHD physics, whilst dashed lines indicate hydrodynamic simulations. The missing distance points for 1330-3H are due to a corruption of the subhalo catalog at these times, as explained in Subsection 3.1.1. The star formation history is calculated as described in Subsection 3.1.3.

In general, the star formation history profiles produced by both physics models are very similar. Reassuringly, the profiles for the hydrodynamic simulations are particularly close with those presented in Sparre and Springel (2016), who ran hydrodynamic simulations from the same initial conditions as our own. As expected, the more energetic mergers show more enhanced star formation at the time of the merger. However, the galaxies in simulations with the prefix 1330-3 and 1526-3 still fall well below the starburst threshold, as defined in Sparre and Springel

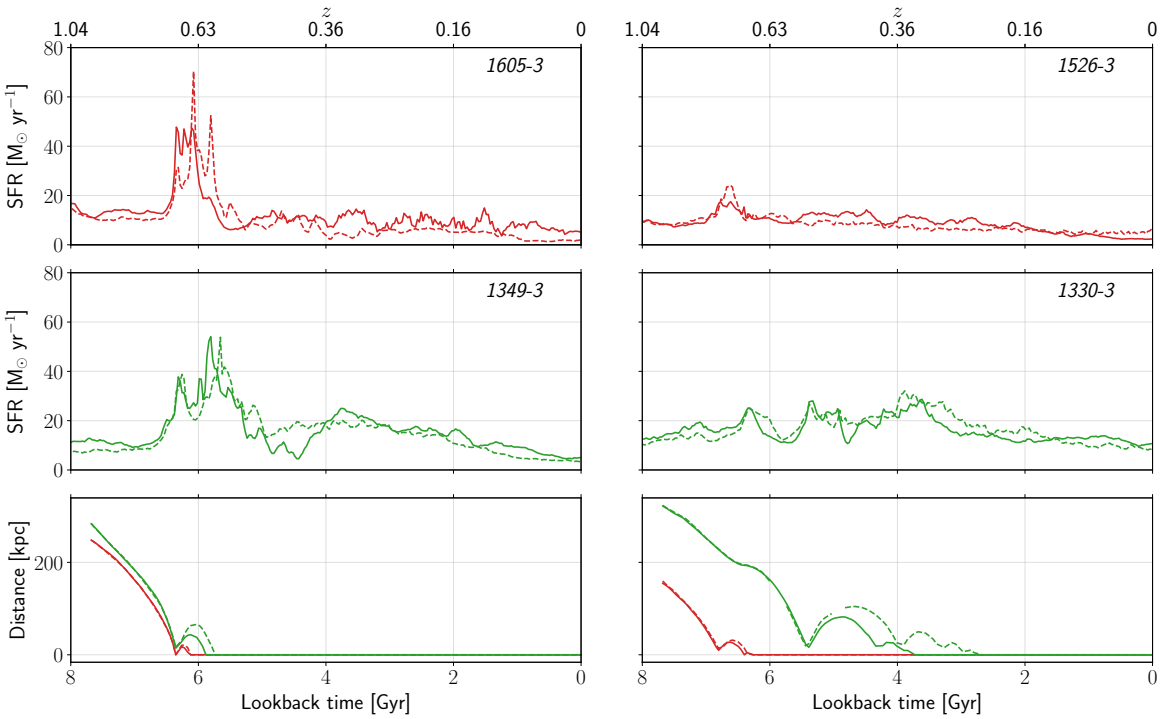

Figure 3.5: *Top two rows:* The star formation history at $z = 0$ for the main galaxy (as defined in Section 2.2.3) in each of our highest resolution simulations. The simulation prefix is located in the top right-hand corner of each panel. Solid lines indicate simulations that included MHD physics whilst dashed lines used hydrodynamic physics instead. Each point shows the mean star formation rate (SFR) during a period of ±15 Myr. *Bottom row:* The proper distance between the centres of the galaxies involved in the major merger of that simulation (as defined in Section 2.2.4). Colours follow from the upper panels. Star formation in each panel follows a similar evolution despite the different physics models being used. In particular, there is no evidence to be seen of magnetically-driven winds suppressing star formation. Interestingly, the time of coalescence in each merger shows a correlation with the physics model, with simulations including MHD physics coalescing at systematically earlier times.

(2017)[10]. This is not too surprising, as our time and mass resolution is still too coarse to produce the necessary gas-consumption timescales for such starbursts (Sparre and Springel, 2016).

Taking a closer look at the details of the star formation profiles, for simulations that included MHD physics we generally see slightly lower star formation rates during the merger, followed by slightly higher star formation rates at later times. It is not clear from this plot whether these differences are a result of physical processes, or whether they are a result of the numerically stochastic nature of star formation at the time of the merger. It also remains to be seen whether the differences affect the total stellar mass produced, or whether the same amount of gas is

[10] A star formation rate to stellar mass ratio that lies 3σ away from the star formation main sequence in Illustris.

being consumed at slightly different times. We will determine this by inspecting the total bound stellar mass evolution in Subsection 3.2.3. Either way, all merger remnants in our simulations are star forming for long periods after coalescence. The galaxy in simulation 1330-3M even has a similar star formation rate at $z = 0$ to that which it had pre-merger. This shows that the Hopkins evolution scenario (see Section 1.3) does not tell the whole story. In particular, it increasingly appears that 'wet' gas-rich major mergers may produce a star-forming remnant (see also Robertson et al., 2006; Sparre and Springel, 2017).

There also appears to be a weak correlation between the inclusion of MHD physics and an earlier onset of enhanced star formation rates. This appears to result from the faster coalescence of the galaxies in MHD simulations, as seen in the bottom row of the figure. In every simulation, the MHD galaxies coalesce before their hydrodynamic analogues. This difference is particularly striking for galaxies that underwent sustained tidal interaction before merging, such as in the simulations with prefix 1330-3. In visual inspections (see Subsection 2.2.5), it appears that the merging galaxy in both of these simulations has lost most of its mass by ~ 5 Gyr. The increased rate of coalescence may therefore be an artefact of non-linear N-body dynamics. However, the effect is systematic in our simulations. One could envisage a mechanism where the magnetic field provides an additional drag force, particularly at periapsis, thereby hastening coalescence. Confirmation of this effect is outside of the scope of this thesis, however, and we leave the investigation of it to future work (see Section 4.2 for further details). In general, we conclude that the magnitude, duration, and timing of the star formation does not change significantly between physics models. As a corollary, we conclude that we do not see evidence of a magnetically-driven wind suppressing star formation rates.

3.2.2 Disc-to-total ratio as a function of merger progress

The outcome of a merger may also be defined by the impact on the kinematics of the galaxy. Sparre and Springel (2017) found that galaxies in simulations based on the same initial conditions as our own regrew substantial stellar discs post-merger. As discussed in Section 1.2, elliptical galaxies and the bulges of spiral galaxies are predominantly supported through anisotropic velocity dispersion whilst stellar discs are predominantly supported by rotation. One method of investigating the regrowth of discs within our own simulations is therefore to attempt to quantify the amount of rotational support in the main galaxy as a function of time. We do this in Fig. 3.6 using the orbital circularity parameter, ϵ, as defined in Abadi et al. (2003)[11]. To calculate

[11] We could equally well have chosen other measures, such as ϵ_v as defined by Scannapieco et al. (2009) or $\kappa_{\rm rot}$ as defined in Sales et al. (2012). We choose ϵ as it is commonly used in literature discussing the Auriga and Illustris simulations (e.g. Snyder et al., 2015; Rodriguez-Gomez et al., 2017).

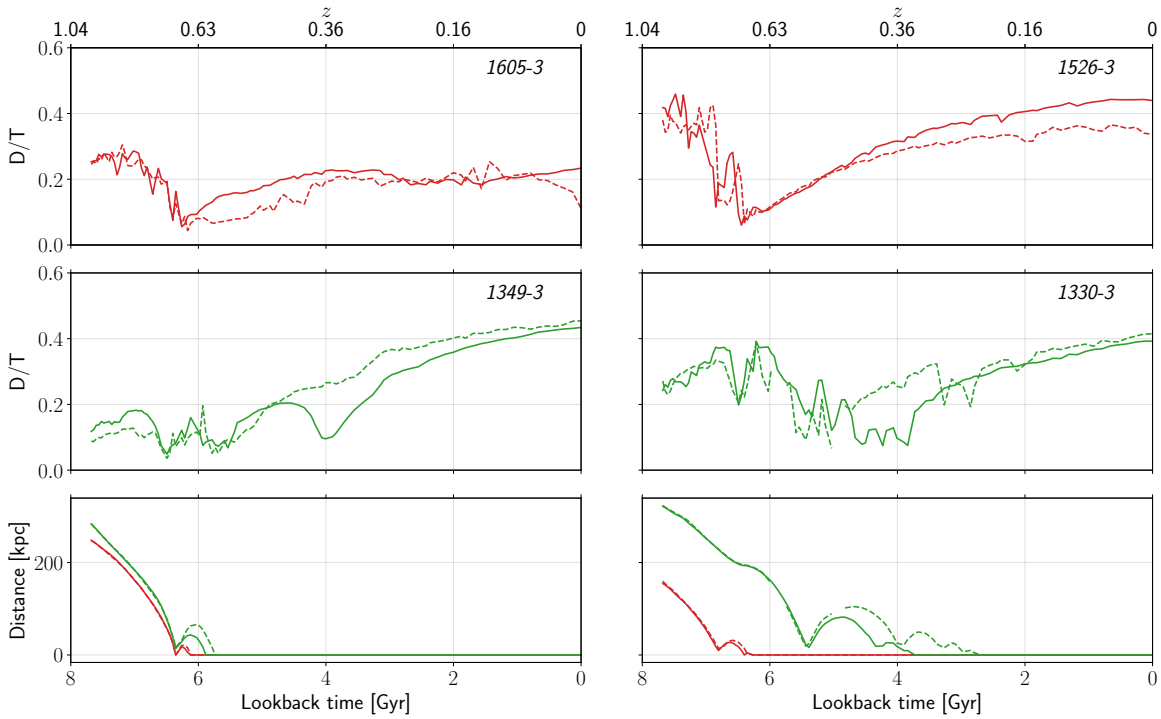

Figure 3.6: As Fig. 3.5, but showing the disc-to-total ratio (D/T) instead of the mean star formation rate. Some values, such as those seen for simulation 1349-3M at ∼4 Gyr and simulation 1605-3H at ∼0 Gyr, appear superficially lower due to tidal interactions with other galaxies distorting the calculation (see text and Section 2.2.4 for details). Once these are ignored, the D/T ratio in each panel appears to follow a similar evolution despite the different physics models being used. Only for the top right panel does including MHD physics seem to support the growth of the disc component relative to what is achieved with hydrodynamic physics, but even here the effect is mild.

this value, we first identify every star particle within $0.1 \times R_{200,\mathrm{crit}}$ of the centre of the main galaxy — as previously noted, this is roughly the extent of the galactic disc. We then define the specific angular momentum in the z-direction, $j_z = (v \times r)_z$, and the specific binding energy, $E = 1/2v^2 + U_{\mathrm{grav}}$, for these particles, where v is the galactocentric velocity, r is the galactocentric position, and U_{grav} is the specific gravitational potential energy of the star particle. The circularity of a star particle is then calculated to be: $\epsilon = j_z/j(E)$, where $j(E)$ is the maximum specific angular momentum possible for the specific binding energy of that star. Finally, we define the stellar mass fraction in the disc relative to the total as the fraction of all star particles having $\epsilon > 0.7$. This ratio is also known as the disc-to-total or D/T ratio[12].

Before we discuss the trends seen, it is worth noting that there are some points in the figure that

[12]Our method will lead to slightly lower disc-to-total measurements than those presented in Sparre and Springel (2016), who use the ϵ_v parameter instead. See Rodriguez-Gomez et al. (2017) for an explanation on how different circularity parameters may be compared.

do not represent the true fraction of stellar mass in the disc. Trivially, as in previous figures, there are two regions where simulation 1330-3H is missing values. As explained in Subsection 3.1.1, the positions of the main galaxy are missing for these snapshots due to corrupt subhalo catalogues. Consequently the disc-to-total ratios are missing as well. Less trivially, the disc-to-total ratios are also impacted by stars from outside the main galaxy entering the selection boundary. Whilst this may cause a genuine disruption to the stellar dynamics, a significant amount of the decrease in the D/T value seen at these times results from the effect of the foreign stars on the calculation of the stellar angular momentum vector (as defined in Subsection 2.2.4). This can result in a mis-rotation of the coordinate system such that the disc of the galaxy no longer lies in the x-y plane, thereby distorting calculations of j_z. An example of this effect is seen for 1605-3H at $z \approx 0$. The merger remnant in this simulation does not grow a large disc post-merger, and so the calculation of the stellar angular momentum vector is unduly affected by a close fly-by at this time[13]. Whilst some galaxies show a dip in their disc-to-total ratio due to a tidal interaction, the dip seen for 1349-3M at $\sim$4 Gyr is due to the reorientation of the galaxy at this point[14]. Here, the galaxy builds a new stellar disc, orientated differently to its remnant. The dip in the disc-to-total ratio signals the new disc becoming dominant over the old remnant disc.

With these factors in mind, we see that the evolution of the disc-to-total ratio is remarkably similar for each galaxy pair. For each galaxy, the D/T value decreases rapidly during the merger. The disc then starts to rebuild almost immediately after the merger, with regrowth proceeding at approximately the same rate in each simulation. The regrowth is generally weaker in simulations with the prefix 1605-3. This results from the formation of a limited disc, rather than from the formation of a large bulge component (see Fig. 3.9 and Fig. 3.14). As noted in Subsection 3.2.1, the merger does not progress at exactly the same rate in each simulation. This affects the convergence of the disc-to-total ratios between the two physics models. These differences are once again particularly clear for simulations with the prefix 1330-3. The reduction in the disc-to-total ratio at coalescence for 1330-3H is not as significant as it was for 1330-3M. This shows that the mass ratio between the merging and main galaxy is significantly reduced by this point. This explains why 1330-3H continues to form a strong disc by $z = 0$, despite the shorter time since coalescence. The galaxy in this simulation ends with a very similar disc-to-total ratio to that seen in 1330-3M. Indeed, allowing for tidal interaction affects, it seems that only the galaxies in the 1526-3 simulations show a significant difference between their final disc-to-total ratios. Even here, however, the difference is mild. 1526-3H does not shown a distinct bulge at $z = 0$, but does show a highly puffed-up disc relative to the other galaxies (see Fig. 3.3.2). This

[13] A full range of times when the galaxy orientation is considered unreliable is shown by the grey bars in rows 6 and 7 of Fig. 3.20.

[14] See the stellar angular momentum evolution in the 6th row of Fig. 3.20.

could have reduced the circularity values of the star particles for this galaxy, relative to those in 1526-3M. Overall, however, we conclude that the addition of MHD physics does not significantly impact the disc-to-total ratio.

3.2.3 Bound gas and stellar mass as a function of time

In Subsection 3.1.3, we found that the star formation histories produced by MHD and hydrodynamic simulations were highly similar. We claimed that this meant it was unlikely that our simulations produced a strong magnetically-driven wind. In this subsection, we check the cumulative effect of any differences seen and investigate our claim more thoroughly. To this end, in Fig. 3.7 we plot the bound gas and stellar mass, as allocated by SUBFIND, of the main galaxy in each high resolution simulation as a function of time. We also plot the sum of the two masses over time. Assuming a galaxy exists in relative isolation post-merger, the gradient of this line provides us with information on how effective any feedback is in ejecting gas from that galaxy: if gas is only being converted into stellar mass, this line will stay constant; if feedback is acting, then this line will show a negative gradient, as gas is unbound from the system. As we will see, this is the case for many of our hydrodynamic simulations, to a much greater extent than for our MHD simulations.

Once again, the time of the merger in each panel is evident by the sudden uptake in bound gas mass and the subsequent acceleration of star formation. Simulations with the prefix 1330-3 show a couple of localised peaks as the merger progresses. This is due to SUBFIND reallocating matter between galaxies as they inspiral. This effect is seen in all galaxies, but is most obvious for the galaxies that take the longest to coalesce. The gas bound to the system at the time of coalescence is generally higher for the MHD simulations than for the hydrodynamic simulations. This supports the idea that the accelerated coalescence seen in Fig. 3.5 and Fig. 3.6 may be due to more effective gas transport in MHD simulations at later stages of the merger. As discussed in Subsection 3.2.1, further analysis would need to be done to really confirm this effect, which we leave to future research (see Subsection 4.2).

The nature of cosmological simulations is that the galaxies do not experience true isolation. We therefore expect to see gas accretion after the merger; an effect that would be absent in idealised merger simulations. In both simulations with prefix 1330-3, a mild increase in gas mass can be seen at ~ 4 Gyr, due to the minor merger that takes place at this time. Minor fluctuations in the gas mass may also be seen at later times, such as at ~ 2 Gyr. These are due to the fly-bys that take place at this time. For 1349-3H, we see a sudden stagnation of the rate of gas loss at ~ 1 Gyr. Whilst it is true that star formation has also decreased at this point, reducing the

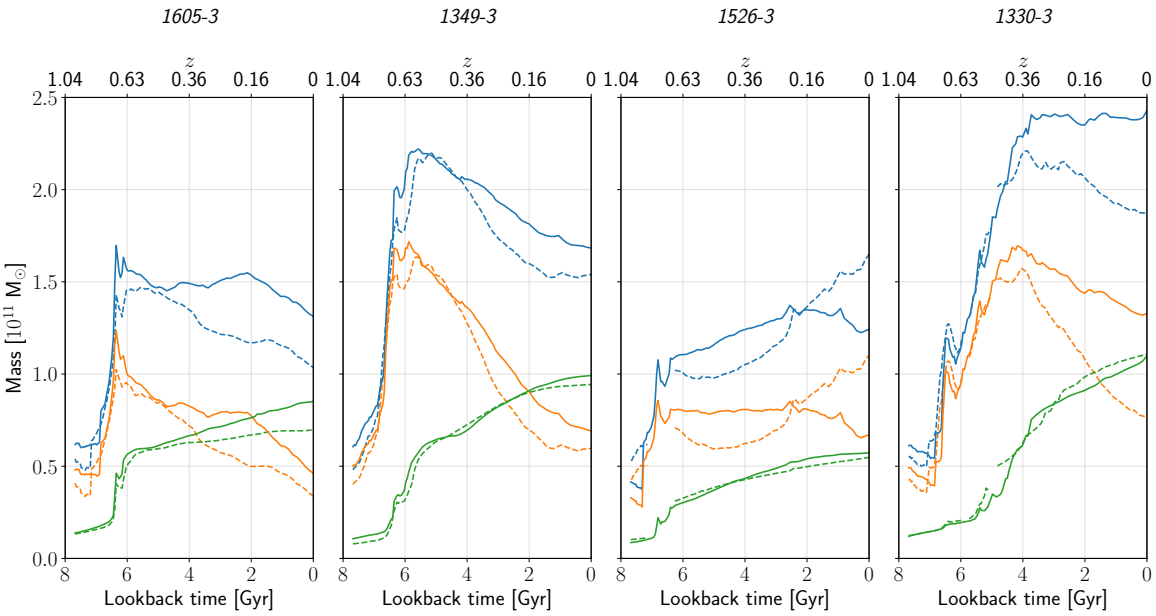

Figure 3.7: Total bound stellar mass (green), total bound gas mass (orange), and the sum of these quantities (blue) for the main galaxy in each simulation (as defined in Section 2.2.3) as a function of time. Solid lines indicate simulations that included MHD physics whilst dashed lines used hydrodynamic physics instead. The simulations shown in each panel start with the prefix displayed above that panel. The total stellar mass formed in each panel is mostly independent of the physics model used. Where there are differences, the total stellar formation is higher when MHD physics were included, as in the rightmost panel. Furthermore, the total bound gas mass is, in general, higher in all simulations except for those with the prefix 1526-3. This implies that feedback is more effective at removing gas in simulations that did not include MHD physics. The growth in total bound mass for simulations with the prefix 1526-3 show that these systems, unlike the others, are accreting significant amounts of gas well after the merger.

impact of stellar winds on the galaxy, the levelling-out of the bound gas mass at this time is most likely a result of gas being brought into the system by the fly-by at this time. The galaxies with the prefix 1526-3 also experience a range of minor fly-bys, which lead to a steady intake of gas after the merger. For the main galaxy in 1526-3H, gas mass is rapidly accreted at ~ 2.5 Gyr due to a very close tidal interaction. This interaction is much more sustained than for 1526-3M, and we see a clear difference in the gas accretion history as a result. The sudden loss of gas mass after ~ 2 Gyr in the 1605-3 galaxies may be attributed to SUBFIND re-allocating mass to an inspiralling galaxy. The main galaxy at this time in these simulations has a very limited size relative to the other galaxies (see Fig. 3.9 and Fig. 3.4.1) and so is more strongly affected by interactions.

Considering these effects, it is apparent that for virtually every merger, feedback is more effectively removing gas from in hydrodynamic simulations than in MHD simulations. Indeed, for many MHD simulations, feedback is highly ineffective, and the loss of gas mass may be accounted for almost entirely by the corresponding increase in stellar mass. This is particularly clear for simulation 1330-3M, but may also be seen in 1526-3M and 1605-3M. This means that we may effectively rule out the existence of strong magnetically-driven winds in our simulations[15]. Interestingly, whilst the gas accretion histories vary between galaxies, there is very little difference in the bound stellar mass evolution. We see that for all simulations except those with prefix 1605-3, the total stellar mass at $z = 0$ is approximately the same. This shows that for these galaxies, variations in the star formation history may be explained mostly as a temporal variation in gas consumption rates. This variation is influenced both by the stochastic nature of star formation as well as by the rate at which the merger progresses. Even for the 1605-3 galaxies, the variation in total stellar mass at $z = 0$ is relatively mild. This suggests that feedback is not efficient at limiting the star formation in these galaxies.

[15] Further evidence against the existence of such a wind will be produced in Subsection 3.5.1.

3.3 Stellar and gaseous morphology

In this section, we investigate the impact of increased resolution on the stellar and gaseous morphology of the merger remnant at $z = 0$ (subsections 3.3.1 and 3.3.3, respectively). We find a significant difference and show that these effects are systematic in our highest resolution simulations (subsections 3.3.2 and 3.3.4). We then perform the same analysis for isolated Auriga galaxies and find similar, but less marked, effects (subsections 3.3.5 and 3.3.6). We interpret this to mean that these effects are induced by mergers.

3.3.1 Mock SDSS gri composites for increasing simulation resolution

In the previous section, we saw that the evolution of the stellar mass in each simulation was similar between physics models. However, similar star formation histories must not necessarily result in the the same galaxy morphology. For example, it has already been shown that the addition of cosmic ray physics to the Auriga galaxy formation model can affect morphological properties whilst leaving global properties relatively unchanged (Buck et al., 2019). On top of this, we also expect that we will only begin to be able to resolve certain small-scale effects, such as the turbulent dynamo, with significantly increased resolution. If these processes significantly impact on the evolution of the galaxies, it will be clear through visual inspection of the merger remnant. We therefore create a series of mock observational images for such inspection.

As discussed in Subsection 2.1.4, each star particle represents a single stellar population, with photometric properties provided in the form of mock SDSS broad bands. These luminosities are tabulated using the catalogues of Bruzual and Charlot (2003). Following Vogelsberger et al. (2014b), we may map the mock g-, r-, and i- band luminosities of these star particles to the red, green, and blue channels of an RGB image. Assuming there is a line of sight to every star, we bin each channel to create a projected image. We then apply the *asinh* scaling given in Footnote 7 of Lupton et al. (2004)[16]. An *alpha* transparency factor is also set proportional to the maximum binned g-band luminosity to provide the impression of saturation. The result is an an RGBA image. This image does not include effects such as dust attenuation, and is therefore not a true observational mock, but it nevertheless provides much useful information. For example, by inspecting this image we may observe where young stars are distributed (bluish-silver pixels) and where old stars are distributed (reddish-brown pixels). We may also qualitatively observe where the most luminosity in the galaxy is concentrated and easily identify morphological features. In

[16] In particular, we use the parameters $\alpha = 0.01$ and $Q = 0.1$ for this equation, and set m to the minimum luminosity value of all bands.

Fig. 3.8, we present mock SDSS images of the merger remnant at $z = 0$, created in this manner. The top two rows show simulations that included MHD physics, whilst the bottom two rows show simulations that included hydrodynamic physics. The mass resolution of the simulation also increases from left to right. In order to roughly conserve the average luminosity per bin, we have coarsened the bin size for the lower resolution simulations.

The galaxy in simulation 1330-1M shows a distribution of younger stars at the centre and at the edge of the disc, resulting in a brighter edge-on image than in 1330-1H. From Fig. 3.3, we may see that the young stars in the MHD simulation are due to a recent boost to the star formation rate. This is probably the result of a tidal interaction caused by the interloping galaxy, visible in the face-on image. Apart from this, the size and stellar distribution of the lowest resolution galaxies are extremely similar. It is likely that before the recent tidal interaction, the galaxies appeared even more similar. By contrast, when we increase the spatial resolution of the simulations by a factor of two, we already begin to see marked differences in the morphology produced. The galaxy in simulation 1330-2M has begun to form sweeping spiral arms and shows a large bulge component. On the other hand, the galaxy in simulation 1330-2H shows significant star formation concentrated in a ring at the edge of the disc. This galaxy also shows a thin stellar bar, with a spiral of stars connecting the ring and the ends of the bar. The radial extent of the disc in the hydrodynamic simulation is also already visibly reduced compared to its MHD counterpart.

Increasing the resolution yet again, we see these components develop further. The smaller spatial resolution has allowed smaller-scale structure to form. The discs are noticeably thinner than they were at the start, with halo stars also less spread out in both simulations. In 1330-3M, the amount of spiral arm structure has increased, but the arms have become less connected. The bulge component has also become much less dominant. In general, the galaxy has developed into a typical flocculent spiral galaxy. The tidal interactions that this galaxy has experienced have led to a warping of the outer disc. The galaxy in simulation 1330-3H shows a much more compact disc, with intense star formation in a stellar ring at the disc edge. The stellar bar is still seen, but is not as well-defined as it was in 1330-2H. The arms linking the bar with the stellar ring are also much less clear, if they exist at all. The stellar ring clearly heavily contributes to the fraction of stellar mass in the disc. This shows that a high disc-to-total ratio does not necessarily result in an extended disc. In general, there is a clear divergence in the evolution of the galaxies between physics models. Importantly, this divergence is only uncovered with significantly increased resolution, suggesting that it is driven by small-scale effects.

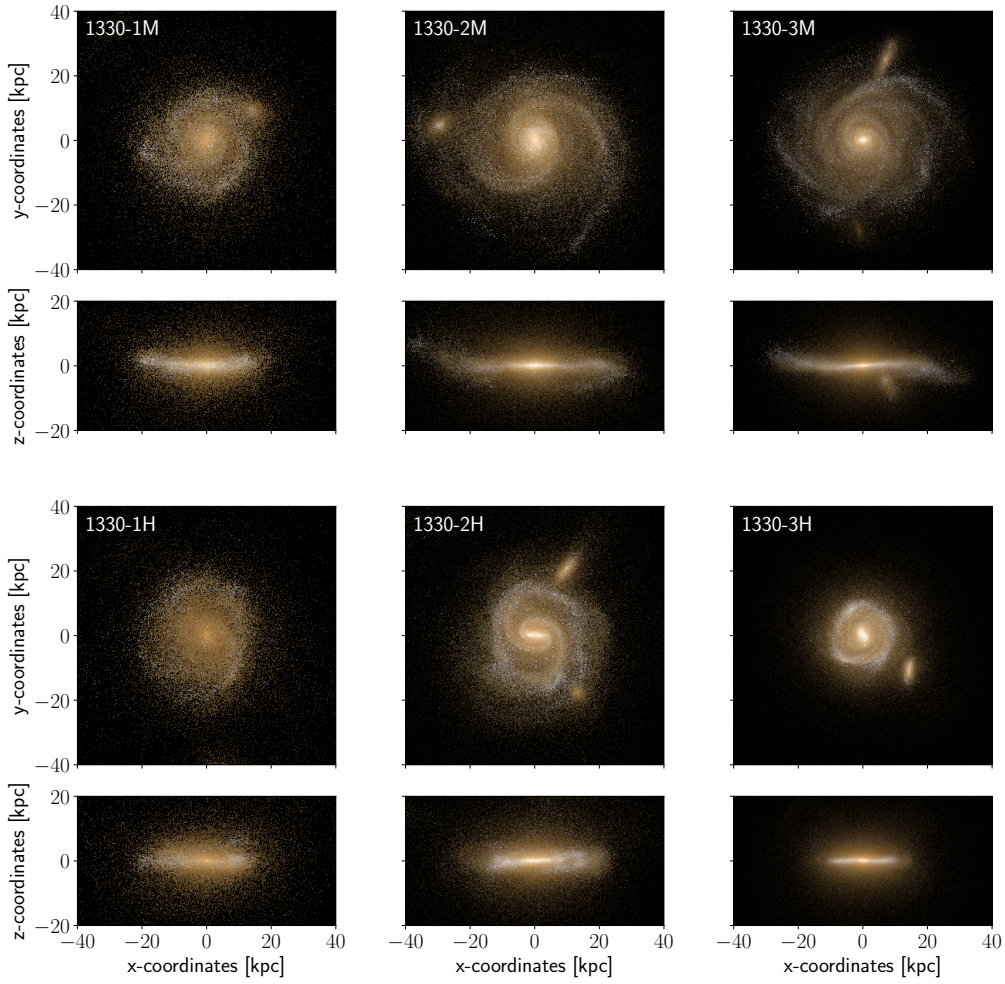

Figure 3.8: *1st row:* Mock SDSS gri composite images for the main galaxy in each simulation (as defined in Section 2.2.3) at $z = 0$. Simulations increase in resolution from left to right, with the simulation name found in the top left-hand corner of the panel. All simulations were run with MHD physics. Galaxy profiles are seen face-on and show star particles to a depth of ± 40 kpc in the z-direction. *2nd row:* As above but galaxy profiles are now seen edge-on. Star particles are seen to a depth of ± 40 kpc in the y-direction. *3rd and 4th row:* As 1st and 2nd row respectively, but simulations included hydrodynamic physics rather than MHD physics. Whilst results for the lowest resolution runs appear roughly independent of the choice of physics model used, increasing the resolution leads to divergent evolution. For simulations that included MHD physics, increasing the resolution resulted in increased radius and increased spiral structure, whilst for those that included hydrodynamic physics, it resulted in a much more compact disc and the formation of bar and stellar ring elements.

3.3.2 Mock SDSS gri composites for the highest resolution galaxies

Naturally, we must check whether the morphological differences seen between the MHD and hydrodynamic simulations presented in Fig. 3.8 occur in all simulations, or whether these differences are unique to the 1330-X simulations. We therefore create mock SDSS images of the merger remnant in all of our highest resolution simulations. These are presented in Fig. 3.9. As mentioned in Subsection 3.2.2, 1605-3H is strongly affected by a tidal interaction at $z = 0$. We therefore present it and its MHD analogue at $z = 0.11$, before this interaction takes place[17]. All other simulations are presented at $z = 0$.

It is immediately apparent that the inclusion of MHD physics leads to a significantly different morphology for every simulation. We also see many of the same features in these images as were identified in Fig. 3.8. For example, galaxies from MHD simulations have systematically larger discs than their hydrodynamic analogues. Naturally, this difference is largest for the largest galaxies. Furthermore, all galaxies from MHD simulations, except for 1605-3M, display extended spiral arm structure. This structure is much less pronounced for 1349-3M than in 1526-3M and 1330-3M, but this may simply be a result of the limitations imposed from possessing a smaller disc-size. In comparison, hydrodynamic simulations result in highly compact galaxies. Indeed, 1605-3H barely forms a disc at all relative to the other galaxies presented. Hydrodynamic simulations also tend to produce stellar bars and rings, which are mostly not apparent in the MHD simulations. That is not to say that stellar bars are systematic to one particular physics model, however. For example, 1349-3M shows a thin stellar bar in its face-on image, whilst 1526-3H does not show a bar. Nonetheless, where they do appear, they are generally much larger in hydrodynamic simulations.

The stellar rings seen in the hydrodynamic simulations are not *typical* of real galaxies, but are also not unknown (see e.g. NGC 1073, NGC 1433, NGC 3081). Where they do exist in reality, the rings are often theorised to be a result of resonant forces channelling the gas. The existence of such resonances is also often interpreted to mean that the galaxy has undergone a mostly secular evolution (see e.g. Buta et al., 2004). Our simulations show, however, that secular evolution is not a necessary condition for such morphology. Interestingly, the galaxies from our hydrodynamic simulations also show some similarities with those presented in Marinacci et al. (2014). In particular, 1526-3H and 1330-3H look similar to Aq-C-4 and Aq-F-5, respectively. This is perhaps to be expected as the Auriga galaxy formation model we use is built upon that of Marinacci et al. (2014). There are, however, significant differences between the models,

[17] The interaction is caused by the small satellite galaxy seen in the top right of the edge-on and face-on images for this galaxy.

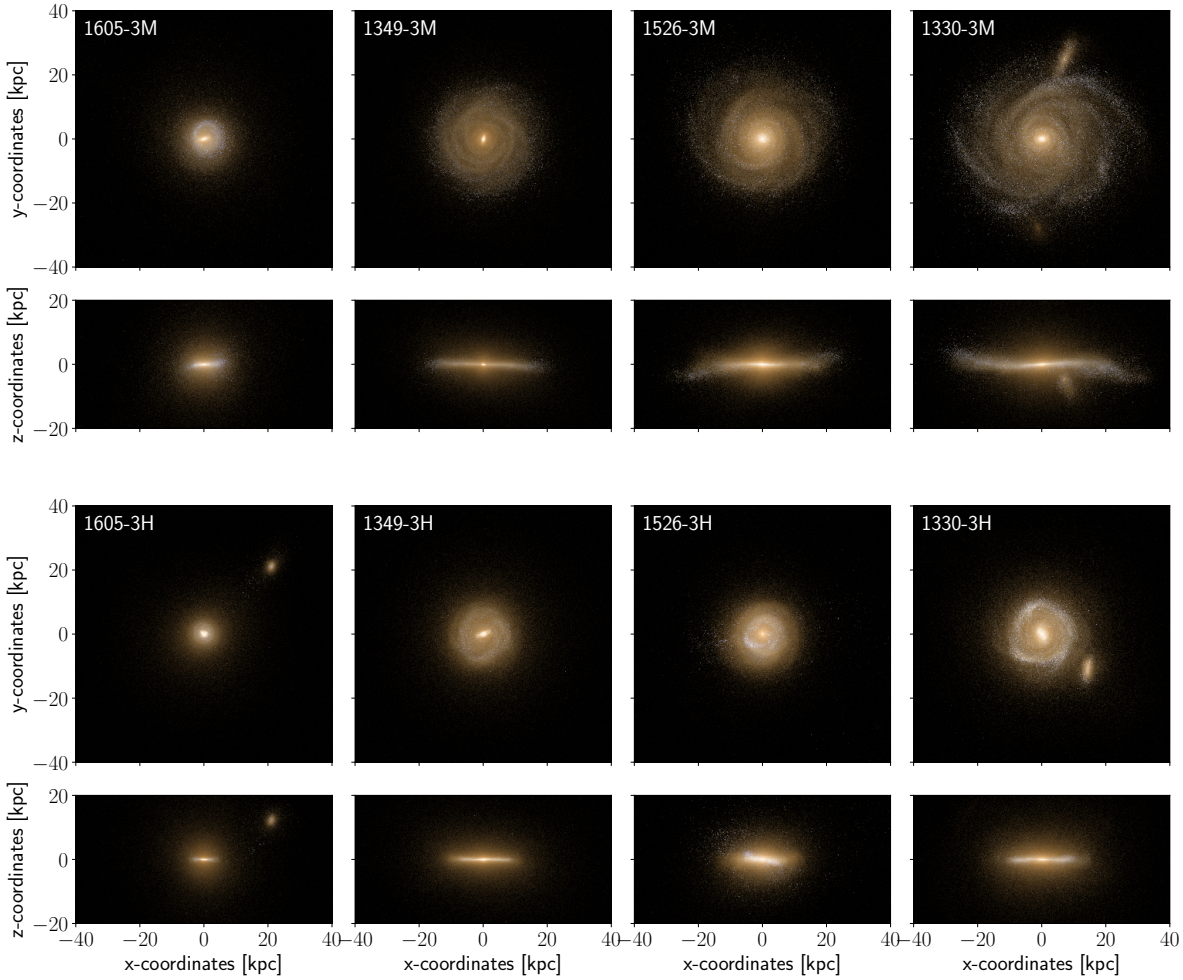

Figure 3.9: As Fig. 3.8, except all simulations presented are now at the highest resolution. Simulations with prefix 1605-3 are shown at $z = 0.11$ due to a tidal interaction disrupting the main galaxy in 1605-3H at later times. All others are shown at $z = 0$. Conclusions from Fig. 3.8 are still applicable here. In particular, in every case including MHD physics has led to a galaxy with a larger radius. Whilst some MHD simulations, such as 1605-3M and 1349-3M do show evidence of bars, these are smaller than those seen in the hydrodynamic runs. 1526-3H does not show the formation of a bar, unlike the other hydrodynamic simulations, however this galaxy is also significantly more puffed-up, suggesting that other dynamics are at play here. The stellar ring in this galaxy also appears qualitatively similar to that in 1605-3M. This suggests that not all features are being formed in the same way.

including a different implementation of stellar feedback (see Subsection 2.1.4). The fact that our hydrodynamic galaxies still look so similar after these changes implies that the addition of MHD physics has been highly significant for the Auriga galaxy formation model.

Outside of the general differences between hydrodynamic and MHD simulations, the galaxies in simulations 1605-3M and 1526-3H are also slightly unusual. Some of their shared features may

be caused by the same underlying mechanism. Both galaxies show a ring of star formation, but this is less well-defined than that seen for other galaxies. The radius of the ring is also near the edge of influence for an AGN. This is supported by the lack of well-defined structure at the centre of 1526-3H, which may be another signature of such activity. A clearer understanding of the dynamics here will be given by inspecting the gas density distribution, which we do in Subsection 3.3.4. 1526-3H also shows a puffed up disc, relative to the other galaxies. Whilst AGN activity could be behind some of this effect as well, the increased scale height has probably resulted from the significant tidal interaction that this galaxy undergoes at ~ 2.5 Gyr. This is particularly likely as halo stars are included in this effect. Minor mergers and tidal interactions have been seen to puff up stellar discs in other simulations (see e.g. Welker et al., 2017).

3.3.3 Gas density distributions for increasing simulation resolution

Star particles in our simulations evolve over several Gyr. Therefore, in inspecting the mock visual images, we are observing the accumulation of changes that have taken place throughout a galaxy's history. As mentioned previously, the gas component is particularly sensitive to changes of the gravitational potential and energy distribution. It therefore provides a window onto the kinematics of the galaxy over much shorter timescales. Furthermore, as the star formation in a region scales with the gas density (see Subsection 2.1.4), the distribution of the gas at a particular time provides information on where future star formation will occur. To analyse the gas density distribution[18], we take a slice through the x-y and x-z planes. We present these in Fig. 3.10. Each pixel indicates the gas density of the cell with the closest Voronoi mesh-generating point. Note, we have increased the dimensions of these images relative to the mock images, such that they now have dimensions of 50×50 kpc. This allows us to show more of the distribution outside of the spiral arms, as well as above and below the galaxy in the x-z plane.

As in Fig. 3.8, differences between the physics models are clearly visible with increased resolution. However, unlike for the visual mock images, such differences are already visible at the lowest simulation resolution. For 1330-1M, we see that the gas takes on a flocculent structure within the disc. There is also a displacement of the gas at the galactic centre, visible both in the face-on and edge-on images. The expulsion of gas in this manner is indicative of an AGN outburst. In simulation 1330-1H, we see that the gas is distributed in a much more inhomogeneous fashion, with the gas mass roughly divided between the centre and the disc edge, with little gas in between. The gas disc is also already notably thinner in the hydrodynamic simulation compared to the MHD simulation, and there is a significant drop in the density above and below the galaxy as

[18] As noted in Subsection 2.1.4, the gas mass of each cell is kept within a target value, so the gas density distribution is roughly equal to the gas mass distribution.

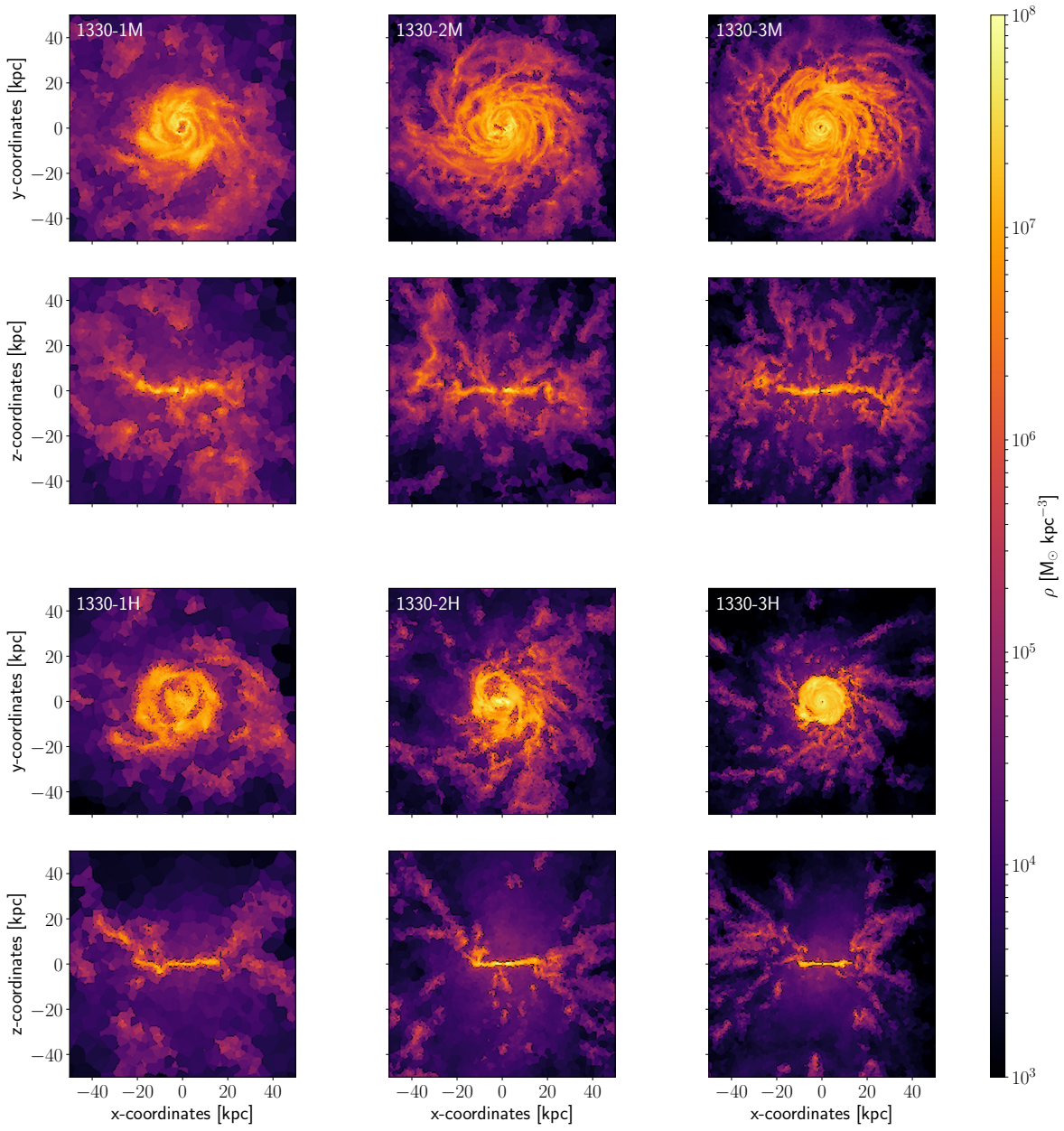

Figure 3.10: *1st row:* Gas density distributions for the main galaxy in each simulation (as defined in Section 2.2.3) at $z = 0$. Simulations increase in resolution from left to right, with the simulation name found in the top left-hand corner of the panel. All simulations were run with MHD physics. Data is displayed as a slice in the x-y plane through the gas cells. *2nd row:* As above but galaxy profiles are now seen edge-on. Data is displayed as a slice in the x-z plane through the gas cells. *3rd and 4th row:* As 1st and 2nd row respectively, but simulations included hydrodynamic physics rather than MHD physics. Differences between the galaxies may already been seen at the lowest resolution, and only increase with increased resolution. The average gas density decreases steadily by radius for simulations that included MHD physics, whilst those that included hydrodynamic physics show peaks in the gas density towards the disc edge followed by a dramatic decrease thereafter.

well. As we increase the resolution, as for the mock visual images, we recover more small-scale structure. For 1330-2M and 1330-3M, this means an increase in the flocculent structure of the gas disc, and the development of more filamentary and clumpy structures above and below the disc. These are typical of a galactic fountain in action. It is also apparent that filamentary gas structure exists in the midplane well beyond the limits of the stellar disc. This is likely to be fuelling the growth of the stellar disc. Once again, mild outbursts are visible at the centre of the disc in both simulations.

As we increase the resolution in the hydrodynamic simulations, the gas discs become thinner and more compact. In 1330-2H, the gas continues to be distributed in a highly inhomogeneous manner, appearing to align most closely with the bar, the inner stellar spirals, and parts of the stellar ring. The high density of gas in the stellar bar shows that this structure is in a positive feedback loop, with its stellar mass supporting further growth. As in 1330-1H, the gas density above and below the disc continues to be much lower than in the MHD simulations. In 1330-3H, the gas structure has suddenly, and perhaps unexpectedly, become much more homogeneous. The bar structure is not particularly well-defined in this image, but it is still clear that there is a peak in the gas density at the galactic centre, surrounding the central black hole. The gas is also particularly dense in the stellar ring. With a keen eye, it may be seen that there are extremely thin spirals of gas connecting the stellar ring with the galactic centre. It is this gas flow that is likely to be fuelling the formation of the stellar bar. Gas has clearly been removed from above and below the galactic disc, and is now only able to accrete from the side. This is a good visual representation of the effectiveness with which gas has been expelled from the galactic neighbourhood, supporting what was seen in Fig. 3.7.

3.3.4 Gas density distributions for the highest resolution galaxies

As before, we check that these effects are systematic by repeating this analysis for all of our highest resolution galaxies. The results are presented in Fig. 3.11. Once again, we see a distinct difference between the two physics models, with galaxies displaying broadly similar features to those identified in Subsection 3.3.3. In particular, simulations 1349-3M, 1526-3M, and 1330-3M all show flocculent gas discs containing a large amount of small-scale structure. The gas discs also have a clear shallow radial gradient. The structure in 1349-3M is generally less flocculent compared to the two larger galaxies, but it too still contains developed small-scale structure, absent from its hydrodynamic analogue. The galaxy in simulation 1526-3M also shows a highly developed gas structure beyond the stellar disc. As for 1330-3M, we expect that this structure is fuelling the growth of this disc.

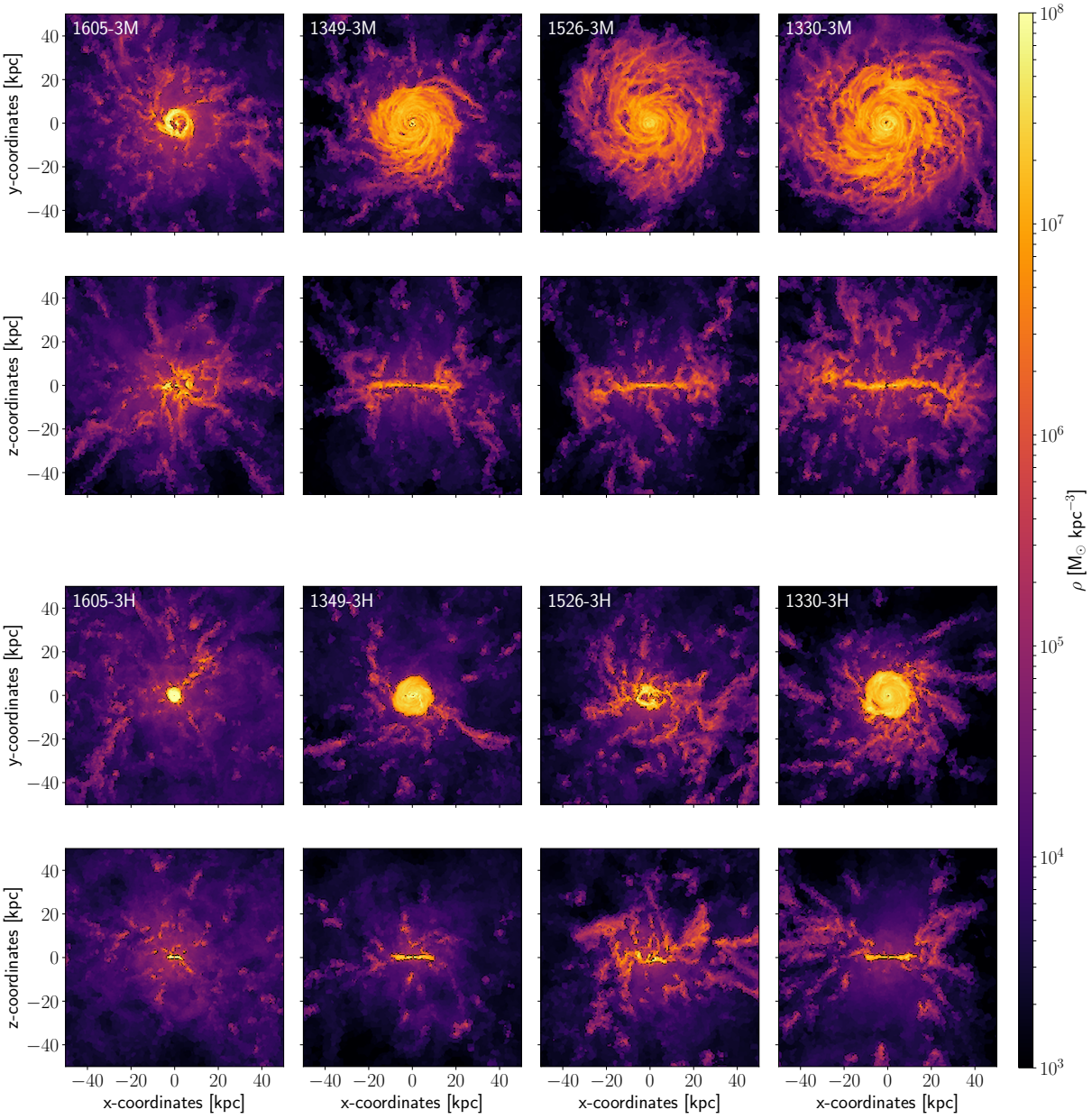

Figure 3.11: As Fig. 3.10, except all simulations presented are now at the highest resolution. Gas density distributions are shown for the same simulations and times as in Fig. 3.9. Conclusions from Fig. 3.10 are still applicable here. In particular, MHD simulations, tend to show a flocculent, radially-extended disc, whilst hydrodynamic simulations tend to show a highly compact disc with a sharp cut off in gas density at the disc edge. The gas density above and below the disc is also notably reduced for hydrodynamic simulations, with disc thickness also reducing with increased resolution. This suggests an increase in the strength of stellar feedback in these galaxies as winds carry the gas away. Simulations 1605-3M and 1526-3H show discs that are heavily disrupted both in the face-on and edge-on projections. This disruption originates from the galactic centre, implying that it is the result of strong AGN feedback.

Simulations 1605-3H, 1349-3H, and 1330-3H show a highly homogeneous gas disc, followed by a drop in density of roughly two orders of magnitude at the disc edge. The increase in stellar mass in these galaxies is also correlated with a reduction in the gas density above and below the disc, suggesting that this gas is being removed by winds. We also expect that this effect is behind the substantially thinner discs seen in the hydrodynamic simulations; wind particles couple with the lower density gas above and below the disc, removing it and thereby thinning the disc. In the MHD simulations, a large stellar mass does not correlate with a reduction in gas density above and below the disc in the same manner. This suggests that the stellar winds in these simulations have a much lower average energy density compared to the hydrodynamic simulations. This assertion will be discussed in more detail in Subsection 3.5.1.

The unusual morphologies that we saw for 1605-3M and 1526-3H in Fig. 3.9 are both partially explained by their gas density distributions, as seen here. Both galaxies show clear disruption of the gas in their face-on and edge-on images. This disruption also originates from the centre of the galaxy, which is a clear signature of an AGN outburst. The similar gas morphologies support our suggestion, made in Subsection 3.3.2, that both stellar morphologies originate from the same underlying mechanism; namely, that the stellar rings in these galaxies are caused by AGN outbursts compressing the gas. Filamentary and clumpy gas structures are visible for both of these galaxies above and below the disc. This suggests that the AGN activity has disrupted the efficient stellar wind seen in the other hydrodynamic simulations. Overall, we may conclude that the effects that we saw in Subsection 3.3.3 are indeed systematic, and that the inclusion of MHD physics has had a substantial effect on the gaseous morphology, especially with increased resolution.

3.3.5 Mock SDSS gri composites for *Auriga* galaxies

The two physics models are clearly producing different morphologies at high resolution. However, it is as yet unclear how much of this effect is due to the major mergers. To investigate this, we compare our merger remnants with a selection of galaxies from the Auriga project. The Auriga galaxies are selected such that, at $z = 0$, they are further than $9 \times R_{200,\,\mathrm{crit}}$ from any halo with a mass >3% of their own[19]. These galaxies have therefore had a significantly quieter merger history than our own[20]. Mock images for these galaxies are produced as in Subsection 3.3.2 and are presented in Fig. 3.12. The Auriga galaxies presented are all 'Level 4' in the Aquarius nomenclature (see Marinacci et al., 2014). This equates to a dark matter mass resolution of 3×10^5 $\mathrm{M}_\odot$, which places them almost exactly between our intermediate and highest resolution

[19] See G17 for a full list of selection criteria.
[20] See also the low accreted stellar mass fractions, f_{acc}, given in Table 1 of G17.

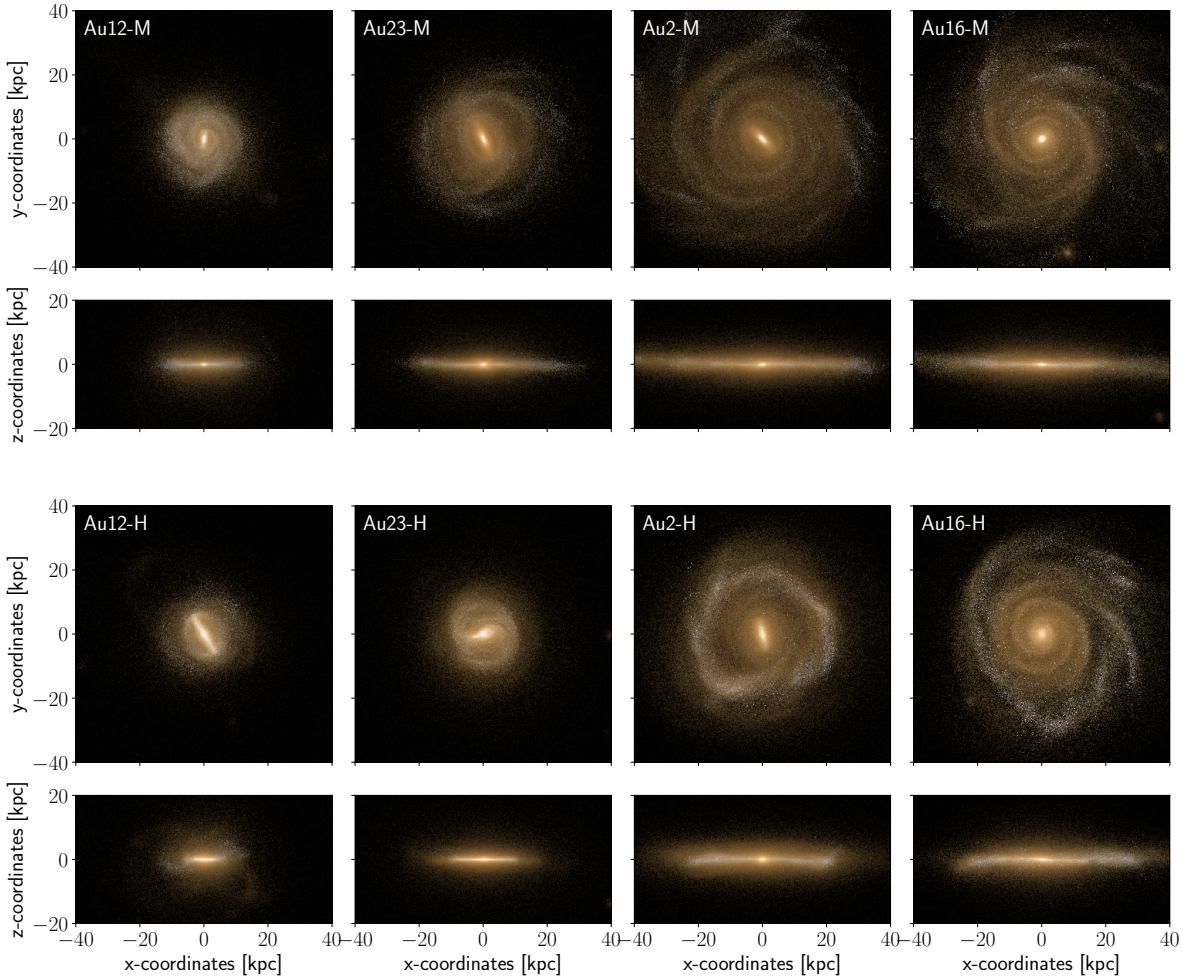

Figure 3.12: As Fig. 3.8, except all simulations presented are now from the Auriga project. Simulation names match those presented in G17, except for the addition of the suffix '-M' to indicate the simulation included MHD physics, or the addition of the suffix '-H' to indicate the simulation included hydrodynamic physics. All simulations are shown at $z = 0$. Data was provided by Rüdiger Pakmor. The dark matter particle resolution in these simulations is $\sim$1.8$\times$ better than our zoom factor 2 simulations and $\sim$1.8$\times$ worse than our zoom factor 3 simulations. All of the galaxies presented here have had a quieter merger history than those in our own simulations, with no major mergers taking place after $z = 1$. Despite this, many of the same features noted in Fig. 3.8 are present, including stronger bars — especially notable in the case of Au12-H — and stellar rings for simulations ran without MHD physics, as well as an increased disc radius for those ran with MHD physics. The difference in the radial size of the galaxy between the different physics models is not as stark as in Fig. 3.9. This may be attributed both to the lower resolution of these simulations and to the quieter merger history.

simulations. Trivially, a lower resolution increases the minimum scale at which physical structure may form. However, as we observed in subsections 3.3.1 and 3.3.3, it also impacts on the resultant morphology. We must consider this effect when comparing the simulation results.

At first glance, many of the features evident in our own simulations may also be observed in the Auriga galaxies. For example, whilst stellar bars are now also seen in the MHD simulations, they are generally more extended in the hydrodynamic simulations. Indeed, the bar in Au12-H transverses almost the entire length of the disc. Furthermore, we continue to see stellar rings in hydrodynamic galaxies, whilst they do not appear in MHD simulations. In particular, the width and position of the stellar ring in Au2-H is extremely similar to that seen in 1330-2H (see Fig. 3.8); only the inner spiral arms connecting the bar and the stellar ring are missing. Even the largest of the hydrodynamic galaxies shows a distorted stellar ring. It is likely that this too was once fully circular[21]. Interestingly, Au16-H is also the only hydrodynamic galaxy not to display a bar structure. It therefore seems likely that the bar structure is providing the resonant forces that generate the stellar ring[22]. This follows from theoretical predictions that gas should accumulate at Lindblad resonances, under the continuous action of gravitational torques (Buta and Combes, 1996; Rautiainen and Salo, 2000).

Whilst there are many similarities between the Auriga galaxies and our own simulations, there are also clear differences. For a start, whilst galaxies from MHD simulations are still systematically larger than those in hydrodynamic simulations, this difference is nowhere near as stark as it was in our own merger simulations. Indeed, both Au2-H and Au16-H have developed quite large discs, relative to those seen in our own hydrodynamic simulations. Au16-H has also developed spiral arm structure in the central part of the disc. In our hydrodynamic simulations, no galaxies were able to form this structure. In Subsection 3.3.3, we saw that the gas distribution in a galaxy could be heavily disrupted by the existence of a stellar ring or bar component. Neither of these features are particularly strong in Au16-H, and this has allowed the spiral structure to form.

In general, it is clear that the two physics models produce more similar morphologies for isolated galaxies than for galaxies that have had a more active merger history. Of course, the Auriga galaxies presented are only isolated from major mergers at late times. Due to the hierarchical growth of structure in ΛCDM, these galaxies will naturally have undergone mergers at earlier times in their history. We therefore propose that the morphological features seen in Fig. 3.9 and Fig. 3.12 are primarily caused by mergers. That these features continue to be identifiable in relatively isolated galaxies is interpreted to mean that the features are relatively stable.

[21] Confirmation of this evolution would be technically simple, but is outside the scope of this thesis.

[22] A corollary of this statement is that we also expect this galaxy to have had a bar at some stage in its evolution. The confirmation of this is, similarly, left to future work.

3.3.6 Gas density distributions for *Auriga* galaxies

In subsections 3.3.3 and 3.3.4, we showed that the differences in the morphology produced by each physics model were even more evident in the gas distribution. We therefore repeat this analysis for the Auriga galaxies. The results are presented in Fig. 3.13. Once again, whilst the rich spiral arm structure in galaxies from MHD simulations is accompanied by an underlying flocculent gas disc, the galaxies from hydrodynamic simulations exhibit either a highly homogeneous gaseous disc or a highly distorted structure. As previously stated, the Auriga galaxies have a dark matter mass resolution roughly 1.8× lower than our highest resolution simulations. This did not lead to significant differences in the stellar morphology between our own highest resolution galaxies and the Auriga galaxies, as seen in Fig. 3.12. Here, however, the gas distributions of the hydrodynamic galaxies are much more reminiscent of our lower resolution simulations, as seen in Fig. 3.10. Only the galaxy in simulation Au23-H shows the homogeneous gas disc that we saw in most of our own hydrodynamic simulations. This galaxy also shows filamentary gas lanes connecting the bar with the disc edge, as well as a similar drop in density beyond the disc edge. The production of this morphology suggests, however, that the Auriga simulations already have sufficient resolution to resolve the features observed in Fig. 3.11. This would imply that the gas distribution in the other galaxies looks different due to their evolution, rather than due to the decreased simulation resolution.

On examining the centre of the disc, it is clear that in MHD simulations the stellar bar is not typically underlaid by a dense, gaseous bar. In contrast, a gaseous bar is clearly present in most of the hydrodynamic simulations. This is taken to its extreme in Au12-H, where the gas distribution follows the bar almost exclusively. The existence of the gas in this distribution implies that this feature is being continually reinforced; the gas fuels further star formation, increasing the gravitational attraction, thereby bringing in more gas in a positive feedback loop. This mechanism is also preventing stars from forming elsewhere in the galaxy. For example, the dominance of the bar means that there is very little gas left in the stellar ring. This has led to a lack of recent star formation here, reducing the luminosity of this ring compared to those seen in our own simulations. In a similar fashion, the gas in Au2-H mostly traces its bar and stellar ring. This has resulted in very little gas being able to produce stars at the centre of the disc, dampening the formation of spiral arms there. The gas in Au16-H is less affected, as its stellar ring is no longer in tact and there is no visible bar structure. This has meant that gas has been able to form a large disc, allowing for the formation of significant spiral structure at the disc centre, as well as filamentary structure at the disc edge. The impact of the remaining stellar ring is still clearly visible, however, as the gas in this galaxy is clearly less flocculent than in its MHD analogue.

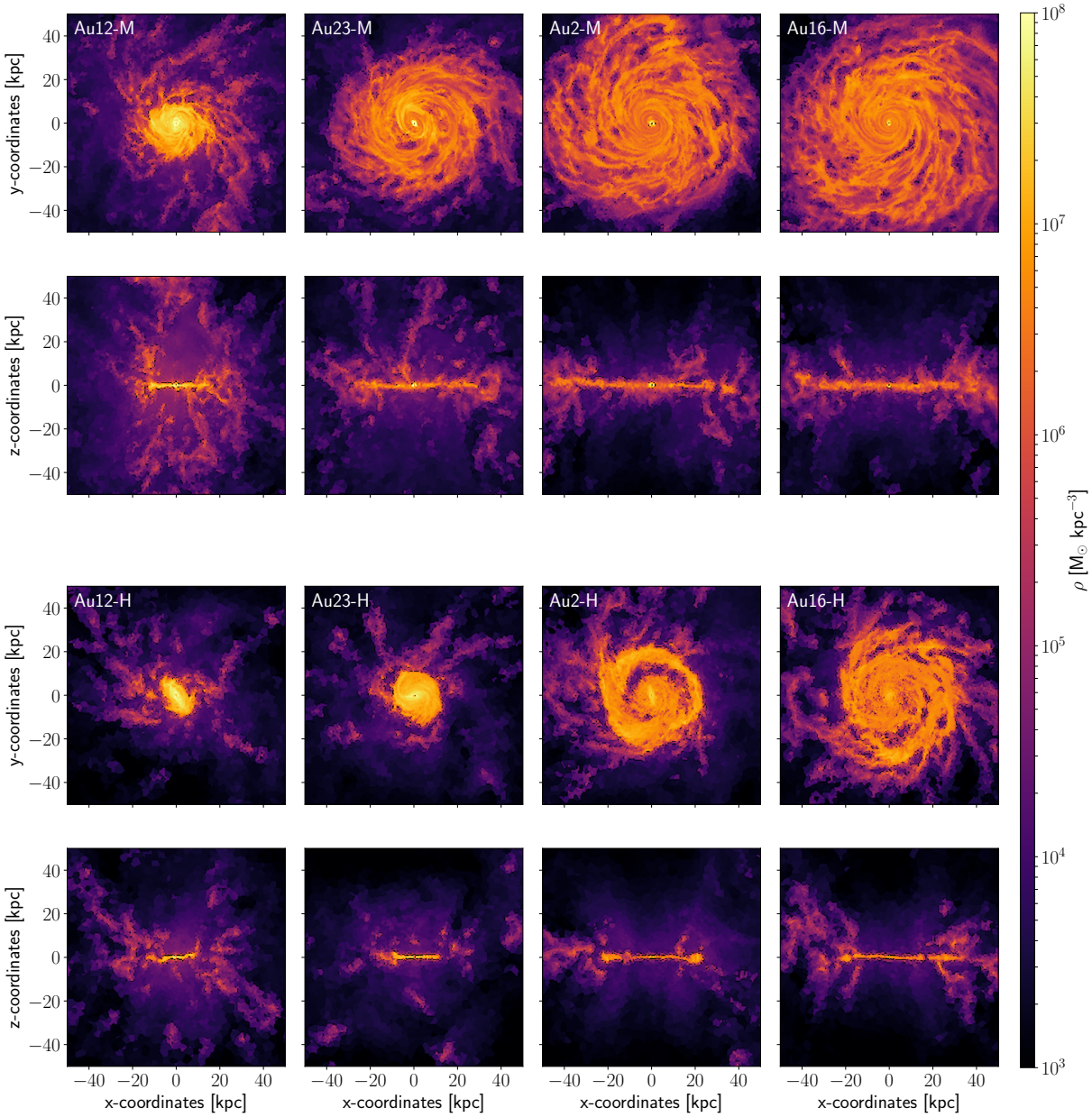

Figure 3.13: As Fig. 3.10, except all simulations presented are now from the Auriga project. Simulations and times are as in Fig. 3.12. Data provided by Rüdiger Pakmor. Many of the features identified in Fig. 3.10 and Fig. 3.11 are visible in this figure as well. For example, in MHD simulations, the gas takes on a flocculent structure, whilst in hydrodynamic simulations, abnormally large stellar bars and rings have pulled the gas into unrealistic distributions. This has, in turn, resulted in a positive feedback loop, where dense stellar features draw in more star-forming gas, perpetuating their formation. This helps to explain why features caused by mergers are still seen in relatively isolated galaxies.

The scale height of the disc in the hydrodynamic simulations is also still visually lower than for MHD simulations. This, combined with the significantly lower gas densities above and below the disc, implies that stellar feedback continues to remove gas more effectively from the disc in these simulations than for galaxies in the MHD simulations. In contrast, these galaxies show highly dense gas surrounding the central black hole, visible in both edge-on and face-on slices. This is not apparent in the hydrodynamic simulations, suggesting that there are generally different gas dynamics at play here between physics models. These gas dynamics may determine whether the morphological features we have identified are stable or otherwise, affecting the evolution of the galaxy.

3.4 Morphological evolution

In this section, we investigate the rate of growth of the disc between physics models (Subsection 3.4.1) and the evolution of the stellar mass, stellar luminosity, and gas surface density profiles (Subsection 3.4.2). We provide further support for our statement that the morphological divergence between the physics models is driven by mergers. We also show further evidence that in MHD simulations AGN feedback tends to dominate gas dynamics over stellar feedback, whilst in hydrodynamic simulations it is the other way around.

3.4.1 Stellar disc growth as a function of time

In Section 3.3, one of the clearest differences seen between hydrodynamic and MHD simulations was the size of the merger remnant at $z = 0$. In every case, the MHD simulation produced a larger disc than its hydrodynamic analogue. The discrepancy in disc size was smaller for simulations of relatively isolated galaxies than for galaxies that had an active merger history. This was one of the factors that led us to propose that these differences were driven by mergers. To substantiate this claim, we investigate the evolution of the disc size in our highest resolution simulations. Following, G17 we calculate the stellar surface density profiles over a depth of ± 5 kpc from the galactic midplane. In the same paper, the authors introduce the parameter $R_{\rm edge}$ to measure the radius of the disc. They define $R_{\rm edge}$ as the radius at which the average stellar surface density drops below 1 $\mathrm{M_\odot\ pc^{-2}}$. We find that this value gives undue weight to the stellar halo in our simulations, and so we raise this value to 5 $\mathrm{M_\odot\ pc^{-2}}$. We find this increased value better correlates with the rejuvenated disc, as embedded in a post-merger stellar background. We calculate the average stellar surface density in concentric rings and linearly interpolate to find the value at which it would be 5 $\mathrm{M_\odot\ pc^{-2}}$. This value is shown in Fig. 3.14, for MHD and hydrodynamic simulations. $R_{\rm edge}$ shows, broadly speaking, the same values for both physics models at $z = 1$. There are some mild differences seen for simulations with the prefix 1605-3 and 1526-3, but these are on the order of $\sim 5\%$. That the disc sizes are so similar before the merger and so divergent afterwards shows that this effect is, indeed, induced by mergers[23].

The major merger in each simulation is evident by the large fluctuation in the $R_{\rm edge}$ value. Minor mergers and close fly-bys result in similar, smaller fluctuations. The latter are particular evident for the simulations with prefix 1605-3 in the peaks at ∼5 Gyr and ∼2 Gyr, as well as at later times for simulations with the prefix 1330-3. The $R_{\rm edge}$ calculation is also occasionally affected by

[23] This conclusion could be confirmed in future work by performing this analysis on the Auriga galaxies presented in Subsection 3.3.5, taking note as to when a minor or major merger took place.

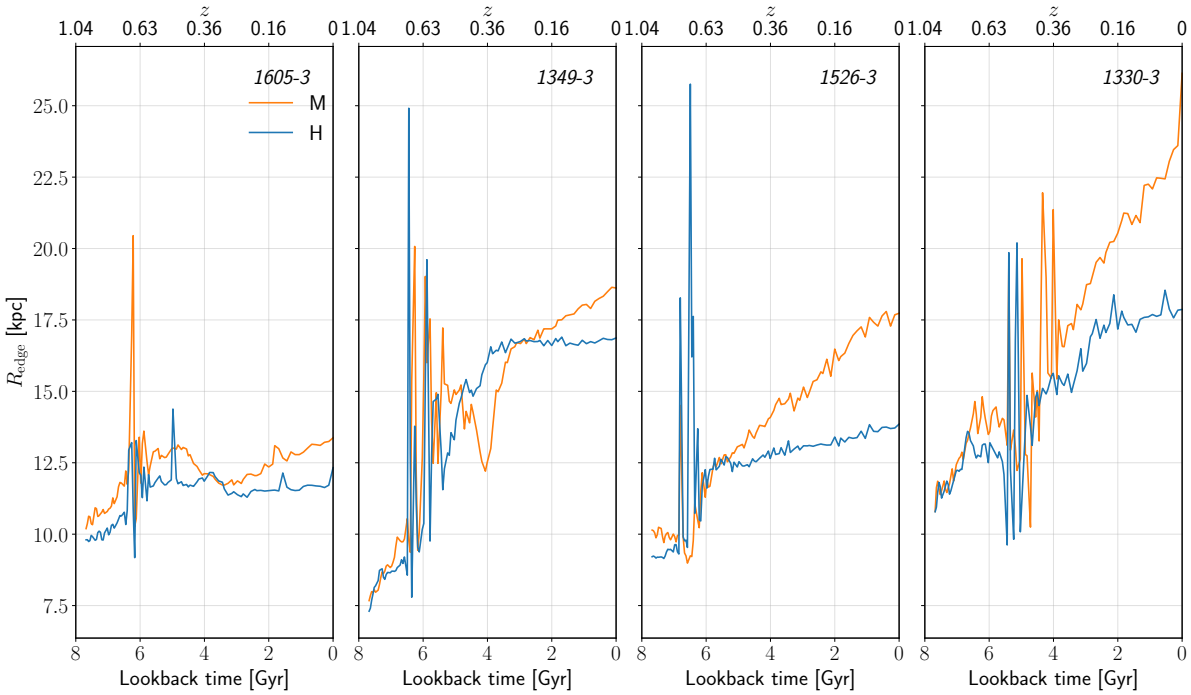

Figure 3.14: The quantity $R_{\rm edge}$ for the main galaxy in each simulation (as defined in Section 2.2.3) as a function of time. $R_{\rm edge}$ is defined as the radius at which the stellar surface density, calculated over a depth of ±5 kpc from the galactic midplane, drops below 5 $M_\odot$ pc^{-2}. Orange (blue) lines show simulations that included MHD (hydrodynamic) physics. The prefix for each simulation may be found in the top right-hand corner of each panel. $R_{\rm edge}$ is broadly independent of the choice of physics model before the merger. During the merger, it fluctuates as the system becomes highly dynamic. As the system relaxes and the disc is allowed to regrow, $R_{\rm edge}$ increases at a steady rate for both physics models. This rate is always higher for the MHD variant and is almost zero in some hydrodynamic simulations (e.g. 1349-3H, 1605-3H). The result is a more radially-extended galaxy in simulations that included MHD physics.

a change in orientation of the stellar angular momentum vector. This is most obviously the case for 1349-3M at the ∼4 Gyr mark, for the same reasons that were outlined in Subsection 3.2.2. After the merger, in MHD simulations, $R_{\rm edge}$ values increase at a relatively rapid, but steady, rate. In contrast, in hydrodynamic simulations, $R_{\rm edge}$ increases at a much slower rate, and for some galaxies appear to have stalled entirely by $z = 0$. Interestingly, the $R_{\rm edge}$ value produced by each physics model only diverges a few Myr after the time of merger. This implies that the growth of the disc is being curtailed in the hydrodynamic simulations by some mechanism.

For simulations with the prefix 1605-3, the $R_{\rm edge}$ values increase after the merger, reach a peak, and then decrease until just after the 4 Gyr mark. This is the most direct and energetic of our merger scenarios, as explained in Subsection 2.2.5. In mock images, created for the descriptions given in Subsection 2.2.5, it is observed that the stellar contents of both main and merging

galaxies is dispersed over a wide volume after the initial collision. The increase and decrease in $R_{\rm edge}$ after the merger is therefore interpreted to be this dispersal, followed by the collapse of the stellar matter onto the merger remnant. The growth of the new disc then starts at around $\sim$4 Gyr. There appears to be a correlation between the difference in the final $R_{\rm edge}$ values and how direct or inspiralling the merger was. Larger discs are expected when the merging galaxy inspirals, as gas is able to maintain a higher orbital angular momentum (G17). The reduced rate of growth of the disc in hydrodynamic simulations, as seen in Fig. 3.14, implies that these galaxies are not maintaining the angular momentum of the accreting gas as well as their MHD counterparts[24].

3.4.2 Stellar mass, stellar luminosity, and gas surface density as a function of time

In Section 3.3, we identified several morphological features that were typical in galaxies in our MHD and hydrodynamic simulations. In MHD simulations, galaxies typically displayed an extended gas disc with a shallow radial gradient, whilst in our hydrodynamic simulations we observed a much more homogeneous gas disc, with a peak in the gas density at the disc edge followed by a sharp drop in density. We also claimed that features in the hydrodynamic simulations were likely to be stable over time. In Fig. 3.15, we check this by presenting the stellar, g-band luminosity, and the gas surface density profiles for our highest resolution galaxies over time[25]. In doing so, we quantify some of the differences in morphology and investigate the rate at which these features form. Analysis of the evolution of these profiles will also provide us with information on the likely mechanism behind the morphologies. The faintest line-colour in a panel indicates the time of merger. Darker shades represent time steps of 1 Gyr towards the present day.

In MHD simulations, it may be seen that the stellar mass surface density in the inner $\lesssim 5$ kpc stays roughly constant for every galaxy. However, as time moves on, the gas from this area is removed, as may be seen by the decreasing gas surface density profiles. This reduces the star formation rate in this region, resulting in a drop in luminosity as the remaining star particles become older and therefore redder. The gas in this central region is also seen to fluctuate in density in some simulations. A scenario explaining this could be that the central AGN is driving the gas out, before switching off due to a lack of recent accretion. Gas would then move back towards the centre of the galaxy as the pressure drops. Self-regulation of the AGN in this manner

[24] We will investigate this effect in more detail in Subsection 3.5.4.

[25] Stellar surface densities are calculated over ± 5 kpc to allow comparison with G17, whilst gas surface densities are calculated over ± 1 kpc to allow comparison with Pakmor et al. (2018).

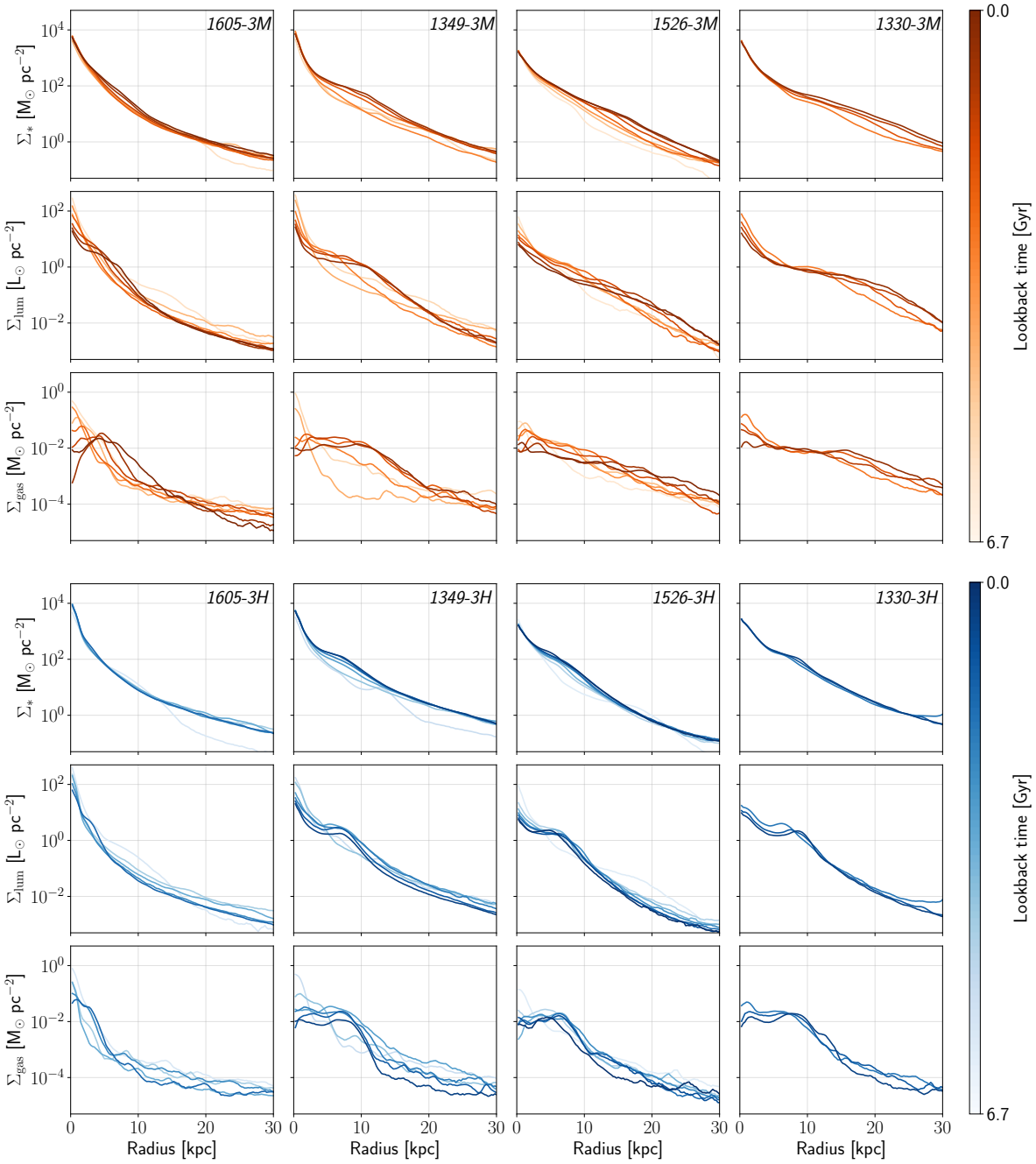

Figure 3.15: *1st row:* Radially-averaged stellar surface density profiles for the highest resolution simulation that included MHD physics. The name of each simulation may be found in the top right-hand corner of each panel. Colours indicate lookback time. The palest shade indicates the time at which the major merger in the simulation took place (as defined in Section 2.2.3). Each darker shade represents a gap of 1 Gyr. The stellar surface density is calculated over a depth of ±5 kpc from the galactic midplane. *2nd row:* As above, except the profiles now show radially-averaged stellar luminosity density in the *g*-band. *3rd row:* As above, except the profiles now show radially-averaged gas surface density calculated over a depth of ±5 kpc from the galactic midplane. *4th, 5th, and 6th rows:* As 1st, 2nd, and 3rd rows respectively, except simulations included hydrodynamic physics. For simulations that included MHD physics, stellar mass is added at a fast but steady rate to the outer regions of the galaxy as new gas is accreted. In contrast, for simulations that included hydrodynamics, gas on the outskirts is removed and stellar material builds up in a ring around the disc. This results in a steep drop off in gas density and a 'sombrero' style luminosity profile.

is expected observationally, although on timescales below our resolution (King and Nixon, 2015; Maccagni et al., 2020). There is evidence of particularly effective AGN outbursts in simulation 1605-3M. These outbursts have carved out the inner regions of the disc and have caused the gas to pile up at the edge of the galaxy. This translates into the star forming ring around the centre, as seen in Fig. 3.9. The peak of this gas density does not remain stable, leading to the stellar ring becoming relatively poorly-defined, compared with those seen in some hydrodynamic simulations.

Whilst gas from the inner parts of the disc is transported outwardly, gas also accretes rapidly onto the outer disc in MHD simulations. This leads to a rapid increase in stellar mass in the outer parts of the galaxy, allowing the stellar disc to quickly grow in size. The final gas structure shows a rather flat surface density profile in the disc, followed by a steady, shallow radial gradient. We may also observe that there is significant amount of fluctuation in the gas density even within the disc. This is the small-scale, flocculent structure within the disc that was observed in Subsection 3.3.4. The break point in the profile is the same for the stellar surface density and luminosity profiles as well. Beyond this point, the gravitational attraction from the star particles is not strong enough to sustain the same gas density. In 1349-3M and 1605-3M, we also see an upwards inflection of the gas density profile outside the disc. At this point the gas dynamics are no longer dominated by gravitational attraction to the star particles. The breaks in the radial surface density are referred to as Type II (downbending) and Type III (upbending) in nomenclature consolidated in Pohlen and Trujillo (2006)[26]. These breaks have been found to occur at approximately the same radii in galaxies from the Auriga project as in real galaxies (Blázquez-Calero et al., 2019).

In the hydrodynamic simulations, we observe that the gas surface density profile shows a much more homogeneous distribution within the disc, with much fewer small-scale variations. This supports what we have already seen in Fig. 3.11. For all discs other than that formed in 1605-3H[27], we observe that the gas distribution is peaked near the centre and at the disc edge. These are the positions of the stellar bar and ring that we described in Subsection 3.3.2. The gas density in the inner $\lesssim 5$ kpc decreases over time, as in the MHD simulations, but here the effect is more gentle. Only in simulation 1526-3H do we see the gas surface density drop appreciably below 10^{-2} $M_\odot$ pc^{-2}. Here too, the gas dynamics appear to be a little more chaotic, again indicating the existence of AGN activity. It appears that gas at the disc edge has moved back towards the interior of the galaxy in the final gas surface density profile shown. This results in star formation taking place closer to the disc centre, smoothing out the previously well-defined stellar ring, as

[26]Type I in this nomenclature refers to a disc that may be described by a single exponential function, as discussed in Section 1.2.

[27]The galaxy in 1605-3H is too small to form a stellar ring or a significant bar.

seen in the stellar mass and luminosity surface density profiles.

In 1349-3H and 1330-3H, the formation of a stellar ring leads to a peak in the gas density there. The radius of this peak remains relatively undisturbed after formation, resulting in a constant localised peak in star formation. This, in turn, results in a peak in the luminosity at this radius, producing an unusual 'sombrero' style luminosity surface density profile. The extreme of this, seen in 1330-3H, is in particular not typical of real galaxies, even for those that do show star-forming rings (see e.g. Fig 31-33 in Buta and Combes, 1996). The galaxies in the hydrodynamic simulations also show a severe drop in gas density outside of the stellar ring. This has developed continuously over several Gyr. In combination with Fig. 3.7 and Fig. 3.11, it is clear that these galaxies are evacuating the gas in their immediate neighbourhood. The reduction in gas in this manner is effectively preventing stellar mass from being formed beyond $\gtrsim 10$ kpc, keeping the stellar disc compact. Most of the stellar mass beyond this distance is dominated by the stellar halo, as seen by the constant stellar mass surface densities and decreasing luminosity surface densities after the merger[28].

It seems clear that the gas dynamics in the galaxy determine its fate post-merger. For galaxies in the MHD simulations, the gas typically settles into a disc with a gentle radial gradient. This allows for more gas to accrete onto the outskirts of the galaxy, resulting in the rapid growth of the stellar disc seen in Fig. 3.14. For galaxies in the hydrodynamic simulations, gas is often pulled into a ring configuration. The dense star formation that follows results in stellar feedback removing gas from the region outside the disc, curtailing the further development of the stellar disc. However, this configuration is only stable as long as the gas at the centre of the galaxy is also stable. Such stability appears to be highly sensitive to the activity of the AGN.

[28]This effect means that the radial position at which the stellar mass surface density drops below 1 $M_\odot$ pc^{-2} does not change appreciably with time for the hydrodynamic simulations. This is why we increased this threshold in the definition of $R_{\rm edge}$, as discussed in the previous subsection.

3.5 Gas dynamics

In this section, we investigate the impact of AGN and stellar feedback on the simulated galaxies. We find that in hydrodynamic simulations, stellar winds dominate the outflows, whilst in MHD simulations, the outflows are dominated by AGN feedback (Subsection 3.5.1). We suggest that the reduced AGN feedback in hydrodynamic simulations results in quieter gas dynamics at the centre of the galaxy, allowing for the formation of stellar bars (Subsection 3.5.2). We also suggest that these stellar bars are torquing the accreting gas, leading to the formation of stellar rings. We propose that, together, these morphological features inhibit the growth of the disc (subsections 3.5.3 and 3.5.4).

3.5.1 Stellar wind and AGN activity

In sections 3.3 and 3.4, we suggested that the different morphologies produced by each physics model could be a result of different feedback processes in action. In this section, we investigate this claim more thoroughly. As the galaxies in simulations 1330-3M and 1330-3H show the greatest difference in morphology, we focus our attention here first. In Fig. 3.16 we present mock images of the galaxies, as seen roughly 2 Gyr after the time of merger. In the panels to the right of this, we show slices in the x-y and x-z planes displaying the velocity of the gas cells[29]. Overlaid are vectors, which show the motion of the gas in the plane. Vectors are not displayed near the disc in order for us to be able to better observe the velocity distribution there[30]. By comparing the mock images and the velocity distribution maps, we may better understand the relationship between the gas flow and the stellar morphology for each physics model.

It is immediately noticeable that the gas dynamics in each galaxy are very different. The velocity distribution maps for 1330-3M show an outburst from an AGN. This is evident as the region of highly increased velocity near the disc centre. The velocity of the gas in this outburst has a magnitude of between 1000 km s^{-1} – 2000 km s^{-1}. This magnitude is maintained until a height of $\sim$ 10 kpc above the disc, before substantially decreasing. Whilst there continue to be significant, lower-velocity outflows above this height, there are also several regions where the gas is seen to be falling back down on the galaxy. This justifies our statement in Subsection 3.3.3 that a galactic fountain is in action in this galaxy. The existence of these fountain flows also

[29]The gas velocity is even more sensitive to changes of gravitational potential and energy distribution than the gas density. A result of this is that gaseous bars, amongst other morphological features, turn out to be more easily identifiable in velocity space than in density space.

[30]If they were shown in the disc, the vectors would display almost uniform rotation in the anti-clockwise direction for both galaxies.

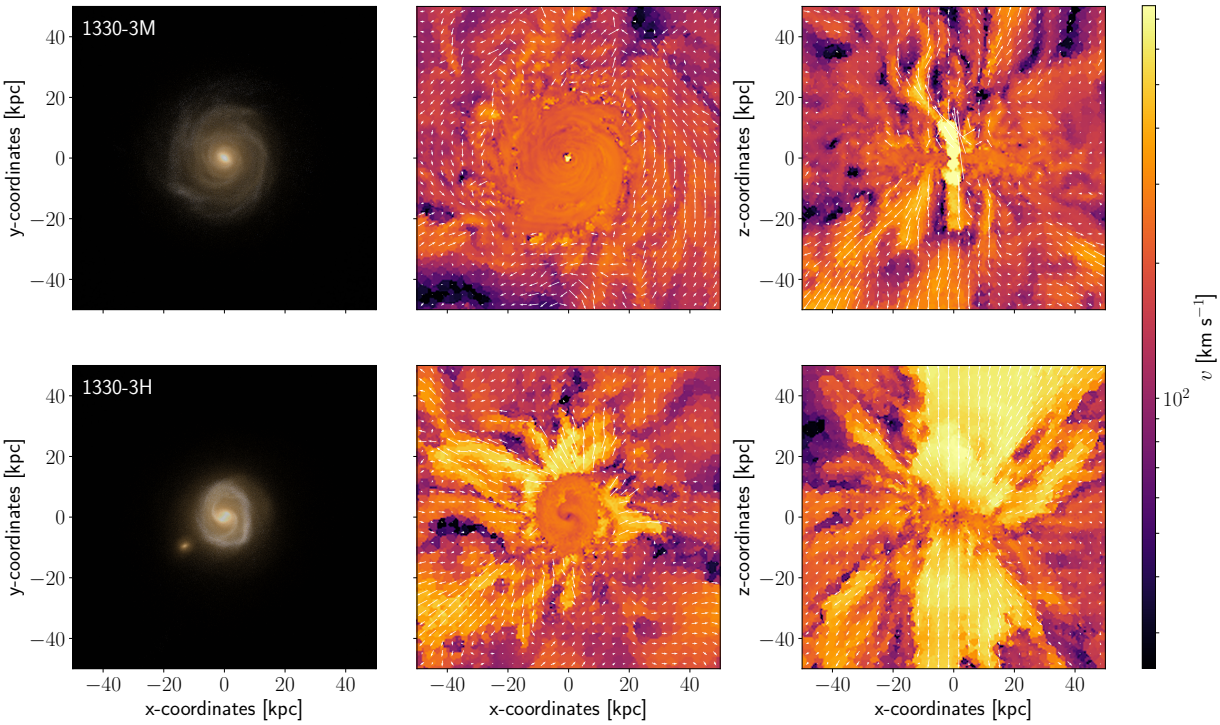

Figure 3.16: *1st column:* Mock SDSS gri composite images for simulations 1330-3M (top) and 1330-3H (bottom), created as described in Subsection 3.3.1. Galaxy profiles are seen face-on and show star particles to a depth of ±50 kpc in the z-direction. *2nd column:* Gas velocity distribution taken as a slice in the x-y plane, created as described in Subsection 3.3.3. The colours are scaled between 25 km s^{-1} and 750 km s^{-1}. Vectors have been included to show the direction of motion of the gas outside the disc. Each vector is scaled to the magnitude of the velocity of the gas cell at its midpoint. Data is still for simulations 1330-3M (top) and 1330-3H (bottom). *3rd column:* As 2nd column, but now taken as a slice in the x-z plane. The simulation in the top row includes MHD physics and is seen at $z = 0.17$. There is clear evidence of an AGN outburst disrupting bar formation. The simulation in the bottom row includes hydrodynamic physics instead and is seen at $z = 0.10$. These images show pronounced stellar winds resulting from strong star formation concentrated in a ring around the galaxy. Gas is spiralling into into a central bar, recognisable as a dark line, showing that it is rotating at a significantly lower speed than the gas in the surrounding disc.

support our observation in Fig. 3.7 that feedback is inefficient at removing gas from this galaxy.

In contrast, no small-scale fountain flows are visible in 1330-3H. The outflows in this simulation also originate from the whole disc, rather than from one point, with little disruption seen in the midplane. Furthermore, the velocity is lower than that seen for the AGN outburst, with typical speeds of between 500 km s^{-1} – 700 km s^{-1}. These properties imply that the outflows in this galaxy are driven by stellar, rather than AGN, feedback. The velocity of the outflow is maintained well beyond the margins of the figure. This helps to explain our observation in Fig. 3.2.3, that gas is being more effectively removed in 1330-3H compared to 1330-3M. The region of

high velocity gas is also clearly correlated with the regions of low gas density seen in Fig. 3.11, confirming that this was a result of stellar feedback.

In the mock image for 1330-3H, we see a well-defined stellar ring at the disc edge, with thin spiral arms connecting this ring to the galactic centre. These arms are also seen in the face-on gas velocity distribution. The gas in these arms has a significantly lower velocity than the gas in the rest of the disc. This shows it is spiralling in towards the centre, fuelling the formation of the stellar bar. The gaseous bar is even more clearly defined than the stellar bar. It is visible as a short, dark, diagonal line in the velocity distribution map. Strong winds are emanating from regions of recent star formation in the stellar ring. These winds are preventing gas from accreting onto the disc, except for at specific points. Two of these points seem to be aligned with the ends of the bar, at 1 and 7 o'clock. This suggests that the bar is torquing the gas at these points, causing it to lose angular momentum. In contrast, for 1330-3M the majority of the gas in the x-y plane is rotating in sync with the disc. The co-rotation of the gas in this manner, allows the gas to maintain its orbital angular momentum as it is accreted. This results in the rapid growth of the disc, as was seen in Fig. 3.14 and Fig. 3.15.

3.5.2 AGN activity and black hole mass as a function of time

The velocity distribution maps seen in the Subsection 3.5.3 showed clearly different gas dynamics at play in hydrodynamic and MHD simulations. AGN outflows were identifiable in the gas velocity maps as a contained region of high velocity near the galactic centre. On the other hand, gaseous bars were identifiable as a region of low velocity at the galactic centre. In order to trace the evolution of these dynamics over time, we introduce the parameter *inner gas velocity*. We define this as the area-weighted median of the gas velocity for a slice of radius 0.5 kpc in the x-y plane. This is a somewhat arbitrary definition, but it turns out to be sensitive to the events described above; in particular, it shows very high values during an outburst and low values during periods of relative stability. We plot this parameter as a function of time for our highest resolution galaxies in the top two rows of Fig. 3.17. The black stars in the panels on the far right mark the times presented in Fig. 3.16. From comparison between these figures, it may be seen that even a relatively small disturbance to the gas in the x-y plane is well caught by our parameter. Grey shaded regions show times when the galaxy does not have a sufficiently developed disc[31]. During these times, the x-y plane does not necessarily line up with the galactic midplane, and values for the inner gas velocity may therefore not faithfully reflect the gas dynamics at the centre of the galaxy.

[31] Considered to be a disc-to-total ratio of $\gtrsim 0.15$ (see Fig. 3.6).

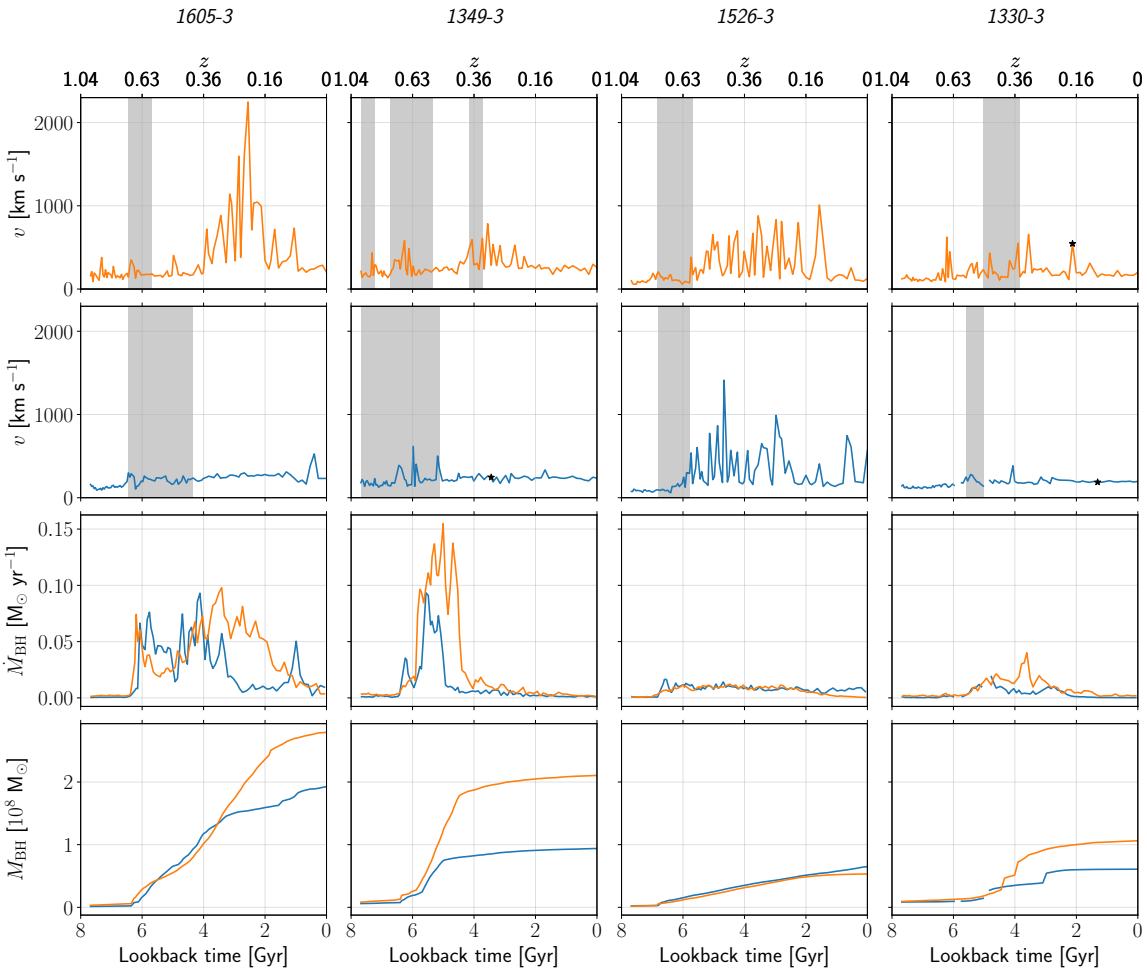

Figure 3.17: *1st row:* The *inner gas velocity* for the main galaxy in each simulation (as defined in Section 2.2.3) as a function of time. The inner gas velocity is a proxy for the gas dynamics at the centre of the galaxy and is defined as the area-weighted median of the gas velocity for a slice of radius 0.5 kpc lying in the x-y plane. All simulations in this row included MHD physics, with the prefix of the simulation seen above the panel/column. Grey shaded areas show data points where the galaxy orientation is unreliable (see text). *2nd row:* As above, except simulations included hydrodynamic physics instead. *3rd row:* The average gas accretion rate during the previous time step for the black hole closest to the galactic potential minimum. Orange (blue) lines indicate the simulation included MHD (hydrodynamic) physics. *4th row:* As above, but showing the total mass of the black hole at that time, including mass gained by mergers. The black stars in the last column of the first two rows are located at $z = 0.17$ and $z = 0.10$ respectively (see Fig. 3.16), whilst the black star in the 2nd panel of the 2nd row is located at $z = 0.30$ (see Fig. 3.18). In general, the central gas dynamics are quieter in the hydrodynamic simulations. This is important as a stellar bar is only able to form under relative stability. Strong AGN feedback, recognisable as a sudden, large increase in the inner gas velocity, can destroy or prevent the formation of a stellar bar. The increased AGN feedback in MHD simulations is powered by increased gas accretion onto the central black hole. This also results in black holes that are significantly more massive.

It is immediately clear that galaxies in MHD simulations have experienced more disturbance to the interior gas than their hydrodynamic counterparts. As stellar feedback does not typically affect the inner gas velocity parameter, this implies a greater level of AGN activity in MHD simulations compared to hydrodynamic simulations. Indeed, every hydrodynamic galaxy, except for 1526-3H, shows a relatively calm history, as described by this parameter. Analysis of mock images[32] shows that these periods of stability correlate with the emergence of stellar bars in the galaxies. Galaxies with high AGN activity do not show the emergence of stellar bars, suggesting that outbursts may be undermining their formation. Looking at the panels for 1605-3M and 1526-3H, we see that there have been extremely high gas velocities at the centre of the galaxy, particularly at late times. This supports our understanding of the gas dynamics in these galaxies, as discussed in sections 3.3 and 3.4. The 'flickering' of the inner gas velocity is likely to be a result of the self-regulation of the AGN, as previously discussed in Subsection 3.5.1. This effect may also be seen in the gas accretion history of the AGN, presented in the 3rd row of Fig. 3.17.

As discussed in Subsection 2.1.4, under the Auriga galaxy formation model, energy is continuously injected into the neighbouring gas cells of the black hole at a rate proportional to the accreted gas mass. We should therefore see generally higher gas accretion onto the central black hole in MHD simulations. Indeed, from the 3rd row of Fig. 3.17, this is generally what we see. The correlation is not exact, however. In particular, the 1526-3 simulations show a volatile inner gas velocity, but generally low gas accretion rates[33]. There are several potential reasons as to why this is the case. For a start, the black hole is not always located at the disc centre. For the 1526-3 simulations, this is particularly the case (see Section A.1). As the disc with which we make the inner gas velocity calculation is relatively small, this means we may sometimes either miss outflows or be more strongly affected by them. We have already seen in Fig. 3.16 that the outflow expands with height. A black hole positioned slightly above or below the x-y plane may therefore have a disproportionate affect. Furthermore, the outburst does not, in general, act isotropically. The direction of the outburst depends on various factors including the positions of the black hole neighbours and their current thermal and potential energy[34].

The increased accretion rates seen for most MHD simulations in row 3 naturally result in larger black hole masses. In row 4 of Fig. 3.17, we present the evolution of the black hole mass in each simulation. Unlike the row above, however, we now include mass added through black hole mergers. These are evident by a sudden jump in mass. Nonetheless, it is clear that the accreted gas counts for a substantial fraction of the total black hole mass. Outside of the simulations

[32] Not shown here due to space constraints. See Subsection 2.2.5 for further details.

[33] Coincidentally, 1526-3M is also the only galaxy to display an azimuthally-dominant magnetic field after the merger. We explore the meaning of this link in greater detail in Subsection 3.6.1.

[34] We expand on this in Section A.1.

with prefix 1526-3, the mass of the black hole is increased in the MHD simulations by a factor of ~ 2 compared to the hydrodynamic simulations. Auriga galaxies have certain parameters chosen so that they reproduce the black hole – stellar mass relation on average (G17). We have, however, already shown that the two physics models produce roughly the same stellar mass between physics models. This might suggest that this relation would be too low without the inclusion of magnetic fields. In practise, however, either values fall well within the standard deviation for the observed relation (Marconi and Hunt, 2003; Häring and Rix, 2004).

The growth of the black hole mass since $z = 1$ has been shown to negatively correlate with the disc radius for the Auriga galaxies (G17). This correlation is generally seen here as well for the same physics model. However, in order to form radially-extended discs in our simulations, it is clear that the AGN feedback may also not be too low. This is in contrast to G17, who found that the disc radius continued to increase if the AGN feedback was switched off after $z = 1$, staying relatively constant otherwise. The cause of this effect was not confirmed, but it was shown that with the AGN feedback turned off, the gas in the galactic neighbourhood was cooler on average, resulting in significantly increased star formation. In contrast, we found that the star formation history of our simulations did not change appreciably between physics models, despite hydrodynamic simulations showing generally lower levels of AGN feedback. This implies that the star formation in our simulations is not limited by a lack of available cool gas, as it is in G17[35]. This difference suggests that the conclusions we are drawing from our simulations are only valid for mergers where the remnant continues to be gas-rich[36]. For our merger scenarios, at least, we conclude that in hydrodynamic simulations stellar feedback is generally driving the outflows, whilst in MHD simulations the outflows are mainly driven by AGN feedback.

3.5.3 Evidence of a stellar bar torquing the gas

We have previously suggested in Section 3.3 that stellar bars may be generating rings of star formation by torquing the accreting gas[37]. We have also suggested that these features are, in turn, stunting the growth of the disc. This is supported by our observation in Fig. 3.16, that gas in the hydrodynamic simulation was predominantly entering the disc at positions aligned with the top and bottom of the stellar bar. We investigate our claim more thoroughly in the current subsection through the use of Monte-Carlo *tracer particles*. These, in their current form, were introduced in AREPO in Genel et al. (2013), and allow a quasi-Lagrangian tracking of the gaseous

[35] This result could be confirmed by calculating the temperature of the gas in the galactic neighbourhood in our simulations, but we leave this as an exercise for the future.

[36] We discuss this and further conditions in more detail in Section 4.1.

[37] We have also suggested that a similar feature may be formed given explosive enough AGN outflows meeting the accreting gas, as in 1605-3M and 1526-3H.

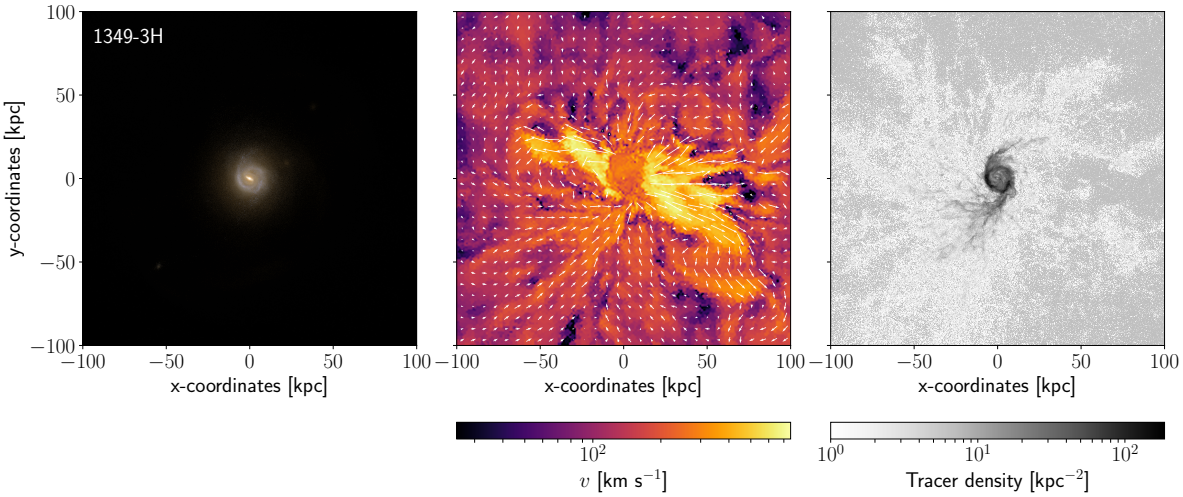

Figure 3.18: *Left panel:* Mock SDSS gri composite image for simulation 1349-3H taken at $z = 0.30$, created as described in Subsection 3.3.1. The galaxy is seen face-on and shows star particles to a depth of ± 100 kpc in the z-direction. *Middle panel:* Gas velocity distribution taken as a slice in the x-y plane through the gas cells, created as described in Subsection 3.3.3. The colours are scaled between 25 km s^{-1} and 750 km s^{-1}. Vectors have been included to show the direction of motion of the gas outside the disc. These are scaled to the magnitude of the gas velocity. Data is from the same simulation taken at the same time. *Right panel:* 2-D histogram of the x and y positions of tracer particles that will end up in gas cells in the galactic disc at $z = 0$. The size of each bin is 0.25 kpc^2. Tracer particles follow the mass flow in the simulation. Gas is shown to be clearly funnelling into the galaxy at the top and bottom of the galactic bar, fuelling the creation of a stellar ring.

mass-flow. This works as follows: at the start of each simulation, five tracer particles are assigned to each high resolution gas cell. These particles are then exchanged with neighbouring cells using a Monte-Carlo algorithm, with the probability of transfer set proportional to the mass-flux across the cell face[38]. As each particle has a unique ID, we may track the particles across snapshots, thereby following the flow of individual fluid parcels throughout the simulation.

In Fig. 3.18, we present three images of the main galaxy in simulation 1349-3H, each seen face-on at $z = 0.30$. In comparing these images, we may understand how the gas is reaching the galaxy. In the left-hand panel, we see a mock image. There is a bright stellar bar stretching across the galaxy, surrounded by a bluish stellar ring, indicating an abundance of recent star formation. There are also a few newly-formed star particles scattered at the ends of the bar. The stellar ring is slightly broken at these points. In the middle panel, we show the velocity of the gas cells in the x-y plane. Here we see many of the same features that were previously observed

[38] Tracer particles may also be transferred to black hole particles and to and from star particles. See Genel et al. (2013) for details.

for simulation 1330-3H in Fig. 3.16. These include strong stellar winds from the newly-formed stars, and gas accreting at the ends of the stellar bar. The stellar winds extend well beyond 50 kpc from the galactic centre, and are preventing gas from accreting onto the disc, except at the points of reduced star formation. With a good eye, it is still possible to see the gas spiralling into the bar, although the bar itself is not so clear. This is partly due to the decreased pixel resolution, as we are now observing the galaxy over dimensions of 100×100 kpc instead of 50×50 kpc. This is also partially due to the instability of these features in velocity space. The inner gas velocity for the galaxy at this time is marked in the 2nd row of Fig. 3.17. By this measure, the gas dynamics are not as stable as they were in 1330-3H. Nonetheless, the lack of outbursts are still allowing a significant stellar bar to develop. This implies that the gas transport from the ring to the bar is not high enough to result in disruptive AGN activity. The bar is therefore stable, given subsequent secular evolution. This explains the existence of the large stellar bars in Fig. 3.12, despite the galaxies being relatively isolated since $z = 1$.

In the rightmost panel, we see the binned positions of the tracer particles that will end up in gas cells within the disc by $z = 0$. The disc in this case was conservatively considered to be a cylinder bounded by a radius of $0.1 \times R_{200,\mathrm{crit}}$ from the galactic centre and with a vertical extent of ± 1.5 kpc from the midplane. The most striking thing about this image is the pair of arms that stretch from the stellar ring at each ends of the bar to several tens of kpc in the x-direction. Resonant forces from the bar have caused the tracer particles to line up in a filamentary-fashion. As the bar rotates, these forces apply periodically to the gas. Previous arms from other phases of this interaction can be seen in the other fainter filamentary structures. From the velocity map, we may see that the gas in these arms is heading towards the galaxy. The tracer particles show a relatively sharp increase in the curvature of their trajectory as they approach the disc. This implies that the gas is losing a great deal of angular momentum, as it is torqued by the bar onto the stellar ring.

The density of the tracer particles at the ends of the bar also correlates with the scattered star formation there, indicating the existence of dense gas. This implies that there is a large mass-flux into the stellar ring at these points. Correspondingly, there is an absence of tracer particles in regions where the stellar winds are particularly strong. This supports our conjecture that the stellar wind is reducing the gas density beyond the disc, as previously seen in Fig. 3.15, preventing this gas from accreting onto the galaxy. In general, it appears that the stellar ring and bar are working in tandem to funnel gas in at the ends of the bar, perpetuating star formation in the ring, and thereby preventing further expansion of the stellar disc.

3.5.4 Specific angular momentum of the gas as a function of time

In this subsection, we compare the evolution of the angular momentum of the gas that will end up in the disc between physics models. By doing so, we quantify our claim that the stellar bars are torquing the accreting gas. We do this for all of our highest resolution simulations and use the same definition of the disc as in the Subsection 3.5.3. For simulations with the prefix 1605-3, we track the gas that will end up in the disc at $z = 0.11$, thereby avoiding the tidal interaction for these galaxies at later times. For all other galaxies, we track the gas that ends up in the disc at $z = 0$. We calculate the tracer-weighted specific angular momentum[39] for all gas cells within 100 kpc of the centre of the main galaxy in each simulation through the formula: $|n_{\rm tr}(\mathbf{r}_i \times \mathbf{v}_i)|$, where i refers to a gas cell, $n_{\rm tr}$ is the number of tracer particles in that cell, $\mathbf{r}$ is its galactocentric position, and $\mathbf{v}$ is its galactocentric velocity. We then calculate the median of the distribution for each simulation and snapshot. The results of this evolution are plotted in Fig. 3.19. A black star in the second panel marks the median specific angular momentum for 1349-3H, at the same time as that shown in Fig. 3.18.

The median values start off relatively independent of the physics model. At this stage, the median value is dominated by the gas that will be accreted from the merging galaxy. This is also seen in the oscillation of the median value at early times. It is clear that this oscillation correlates with the distance between the merging and main galaxy, as seen in Fig. 3.5. These oscillations are broader for simulations with prefixes 1526-3 and 1330-3 as these mergers are the most inspiralling (as discussed in Subsection 2.2.5). After the galaxies have coalesced, the evolution of the median begin to be dominated by the gas being torqued onto the galaxy. Naturally, as the discs of hydrodynamic galaxies are smaller than their MHD analogues, the median specific angular momentum will end up with a lower value at the final snapshot. However, the trajectory of the median value is also different between the physics models. In the hydrodynamic simulations, the median value stays high after the major merger, and then drops, precipitously in the case of 1605-3H, within the last 2-3 Gyr. In contrast, MHD simulations show a much lower rate of decrease. For 1526-3M and 1330-3M, the gas keeps a relatively steady median specific angular momentum once the merger has completed. The gas then experiences very gentle torques at late times before joining the disc. This approximate conservation of the angular momentum of the gas explains why the disc in these simulations is able to grow so rapidly (see Subsection 3.4.1). On the other hand, the rapid loss of angular momentum in hydrodynamic simulations prevents the growth of the disc.

[39] As each gas cell is required to stay within a factor of two of the target mass, the specific angular momentum is roughly equivalent to the orbital angular momentum of the gas, divided by the target mass.

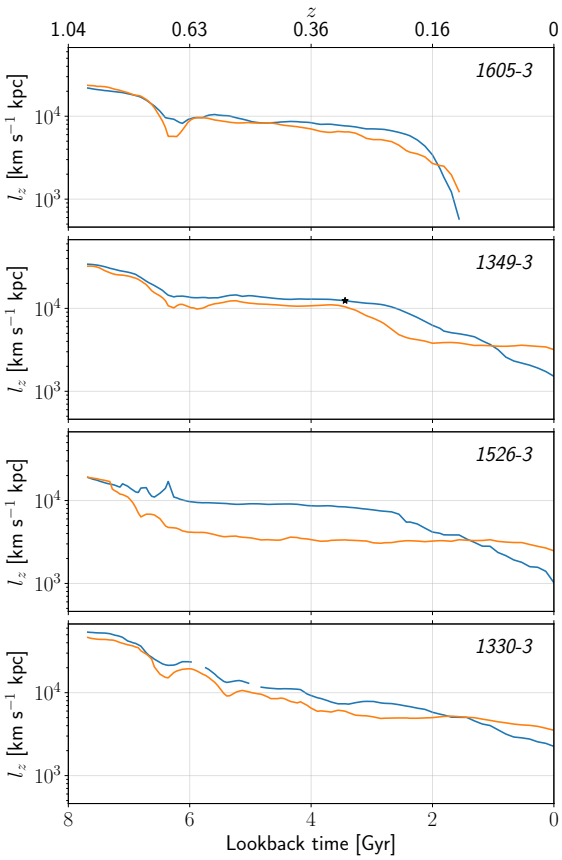

Figure 3.19: The evolution of the median specific angular momentum of all gas, weighted by the number of tracer particles contained per gas cell, that at $z = 0$ ($z = 0.11$ for simulations with prefix 1605-3) will be in the disc of the main galaxy for each simulation (as defined in Section 2.2.3). Orange (blue) lines show simulations that included MHD (hydrodynamic) physics. The prefix for each simulation may be found in the top right-hand corner of each panel. The black star in the 2nd panel is located at $z = 0.30$ (see Fig. 3.18). Initially, the angular momentum decreases in an oscillatory fashion as the merging galaxy inspirals onto the main galaxy. The median angular momentum then remains roughly constant and is either accreted onto the edge of the galaxy as the disc grows, as is the case for most simulations including MHD physics, or is strongly torqued in the last ∼2 Gyr by a bar or asymmetric stellar ring, as is the case for simulations including hydrodynamic physics.

Some remaining differences in the angular momentum evolution may be explained by differences in the merger history. In particular, whilst both galaxies in the 1526-3 simulations experience a major tidal interaction at 2.5 Gyr, the impact parameter for this interaction is significantly lower in the hydrodynamic simulation. This means that the galaxy in this simulation acquires a considerably larger amount of gas mass at late times compared to its MHD analogue[40]. The result is that the median specific angular momentum value for 1526-3H stays high until this time, whilst the galaxy in the 1526-3M has already shown a significant decrease. This effect is also seen

[40]This was previously discussed in Subsection 3.2.3.

by the reduction in strength of the oscillations at early times, and by the uptick in the median at around ∼6.5 Gyr. Similarly, the flyby in 1349-3H at ∼1 Gyr is seen in the slight rise in the median at this time. The impact of the disc rebuilding around the merger remnant, as discussed in Subsection 3.2.2, is also seen in the dip in the median for 1349-3M at ∼ 3 Gyr. From this point onwards, the median for 1349-3M behaves similarly to the median in simulations 1526-3M and 1330-3M post-merger. Even considering these differences, it is still clear that hydrodynamic galaxies exhibit an increased rate of loss of angular momentum at late times. This indicates that the gas is indeed being torqued more strongly as it approaches the disc in these simulations.

Finally, we note that simulations 1605-3M and 1526-3H once again show similarities with one another. Here, each simulation shows a relatively similar evolution of their median specific angular momentum in the final ∼ 4 Gyr. In each simulation, the median value declines steadily, before sharply decreasing in the last few Myr. We attribute this behaviour to the lack of stellar bar in these galaxies, with torques provided instead by an AGN-produced, asymmetric stellar ring. These asymmetries only dominate the gas dynamics at close range. The similarity of the trajectory of the median for these galaxies provides further support that their morphologies are produced by a similar mechanism. This mechanism is different from that followed in the other simulations. For the others, we conclude that the gas dynamics at the centre of the main galaxy in hydrodynamic simulations are relatively quiet. This allows for the formation of a stellar bar, which torques accreting gas into a ring. Together the bar and the stellar ring shepherd the gas so that they continue to be reinforced, thereby stunting further growth of the disc. For MHD simulations, on the other hand, the formation of such strong bars is inhibited by increased AGN feedback, caused by a more effective fuelling of the central black hole. This allows the galaxy to form a radially-extended disc with all the features noted in Fig. 3.9.

3.6 Magnetic field structure

In this section, we investigate the impact of the merger on the magnetic field in the disc. We show that magnetic fields in the inner region are strongly amplified during a merger and that the field has a dominant azimuthal component only when the gas is accreted whilst the galaxy has a stable orientation (Subsection 3.6.1). We also illustrate some common field configurations post-merger and show that the increased black hole fuelling seen in Subsection 3.5.2 occurs only when the field has a strong radial component (Subsection 3.6.2)

3.6.1 Magnetic field strength and galactic orientation evolution

In Subsection 1.4, we noted that previous simulations have concluded that magnetic fields may be efficiently amplified during mergers. We also noted that starburst regions — another common signature of mergers — have been observed with magnetic field strengths of between 50 and 100 μG. In this subsection, we investigate the magnetic field amplification in our own mergers and check that they show reasonable field strengths. To this end, in the top row of Fig. 3.20, we present the mean magnetic field strength over time, given in radial bins of 0.25 kpc. Bins contain each gas cell with a mesh-generating point within ± 1 kpc of the galactic midplane, and the contribution to the mean is weighted by the gas cell volume.

At the time of the merger, the magnetic field strength in the inner regions of the disc ($\lesssim 5$ kpc) is increased by up to an order of magnitude. As expected, the strongest amplification of the magnetic field also occurs for the most energetic mergers; i.e. in simulations 1605-3M and 1349-3M (see Subsection 2.2.5). The pixels only over-saturate in simulation 1349-3M, but here they over-saturate significantly, with mean field strengths reaching a maximum of 171 μG. Field strengths this high are unusual, but are not unheard of for starburst galaxies (see e.g. Lacki and Beck, 2013). Otherwise, the field strengths in our simulations are in good alignment with those expected for gas-rich merging galaxies. For example, the amplification seen for the inspiralling galaxies shows strong similarities with the observed field strengths and predicted evolution presented in Fig. 12 of Drzazga et al. (2011). Our simulations differ from this evolution after coalescence, however. Whilst Drzazga et al. (2011) predicts that the field strength quickly decreases to a magnitude lower than pre-merger, in our simulations, the field strength remains highly amplified for at least 1.5 Gyr after coalescence. Furthermore, when the field strength does eventually decrease, it saturates at a strength that is at least as high as that which the galaxy had pre-merger. This difference is likely to arise due to the fact that our galaxies do not eject their gas during the merger, in contrast to the 'traditional' merger scenario. A result of this is

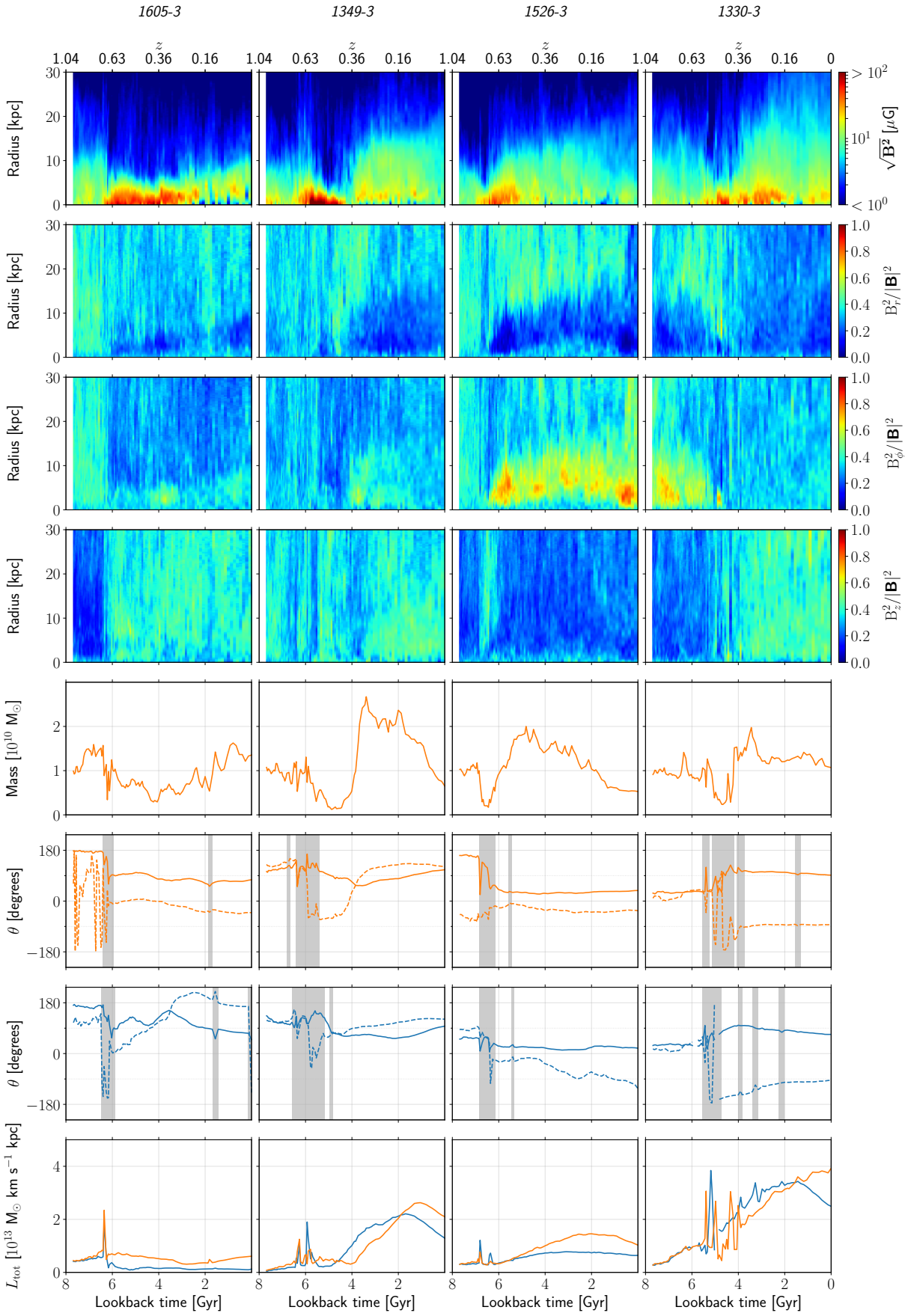
1605-3
1349-3
1526-3
1330-3
z
1.04 0.63 0.36 0.16 0
Radius [kpc]
$\sqrt{\mathbf{B}^2}$ [μG]
$\mathrm{B}_r^2/|\mathbf{B}|^2$
$\mathrm{B}_\phi^2/|\mathbf{B}|^2$
$\mathrm{B}_z^2/|\mathbf{B}|^2$
Mass [10^{10} M$_\odot$]
θ [degrees]
$L_{\omega t}$ [10^{13} M$_\odot$ km s^{-1} kpc]
Lookback time [Gyr]

Figure 3.20 ***(previous page)*****:** *1st row:* Radially-binned mean magnetic field strength for the main galaxy (as defined in Section 2.2.3) in each simulation that included MHD physics as a function of time. The simulation prefix is located above the panel/column. Bins have a radial extent of 0.25 kpc and a vertical extent of ±1 kpc from the midplane. *2nd, 3rd, and 4th row*: As 1st row, but showing the fraction of the magnetic field energy in the radial, azimuthal, and vertical components respectively. *5th row:* The gas mass that is contained within an annular ring with bounds ±1 kpc from the midplane and radii 2.5 kpc and 10 kpc from the galactic centre as a function of time for each MHD simulation. *6th row:* The angle of the stellar angular momentum vector (as defined in Section 2.2.4) from the positive z-axis (solid line) and in the x-y plane (dashed line) as defined pre-coordinate transformation (see Subsection 2.2.3) as a function of time for each MHD simulation. For the latter quantity, a positive value indicates anti-clockwise rotation from the positive x-axis. Bounds on this plot are ±235°. Grey shaded areas show data points where the galaxy orientation is unreliable (see text). *7th row:* As above but for simulations that included hydrodynamic physics instead. *8th row:* The magnitude of the stellar angular momentum vector for simulations that included MHD physics (orange) and simulations that included hydrodynamic physics (blue). Immediately after coalescence, the strength of the magnetic field in the inner 5 kpc increases by up to an order of magnitude. This amplified field is then evident for between 1 Gyr and 4 Gyr afterwards. At the same time, the magnetic field strength in the outskirts of the galaxy drops by roughly an order of magnitude, and stays this way until gas is brought back during the rebuilding of the disc to these radii. The merger process can destroy an azimuthally-dominant field (as in 1330-3M) or build one (as in 1526-3M). Whether one is created or not depends on whether gas is accreted onto the merger remnant whilst its orientation is stable. Galaxies end up with similar stellar angular momenta regardless of the physics model used. Differences in the evolution of the orientation of this vector are mostly accounted for by its stability, where a higher total angular momentum provides higher stability.

that the magnetic field is maintained and is observable in an amplified state well after the initial merger-induced starburst (as shown in the star formation histories presented in Fig. 3.5). The observation of a strong magnetic field in a galaxy with normal or low star formation rates may therefore be an indication that it has undergone a gas-rich major merger in its past.

The decrease in magnetic field strength in the inner regions after coalescence is correlated with the rebuilding of the disc. This rebuilding is seen in the figure through the increase in the field strength at higher radii. The field strength also reduces at these radii at late times in some galaxies, as gas is eroded by star formation without being replenished. Such a process is seen particularly for 1526-3M from ∼2 Gyr. Gas is also removed periodically from the inner regions, due to AGN activity (see discussions in subsections 3.4.2 and 3.5.2). This results in the magnetic field strength 'flickering' at late times. This process may be undermining the amplification of the magnetic field, as field strengths do not generally recover to the same level afterwards. On the other hand, there are periods when the magnetic field strength increases at late times. For example, we see an enhancement of the magnetic field strength in 1330-3M by a factor of roughly

two at $z \approx 0$. As discussed in Subsection 2.2.5, the galaxy in this simulation undergoes a series of minor tidal interactions at late times. However, it is not clear whether the field amplification is a direct result of this interaction; whilst Pakmor et al. (2017) do observe that minor mergers can cause such an effect, it is difficult to distinguish the enhancement in this galaxy from fluctuations seen in other simulations.

Whilst our simulations show reasonable agreement with observations, they show significantly higher field amplification in the central regions than that observed in isolated MHD merger simulations performed using either AMR (Rodenbeck and Schleicher, 2016) or SPH (Kotarba et al., 2010) codes. This may be a result of the more comprehensive feedback implementation included in our simulations[41]. Although not shown explicitly here, the field strength at the time of the merger increases by more than that expected through adiabatic compression due to the increased density (see Subsection 3.1.4). This suggests that the amplification at this time is at least in part due to the resolution of a small-scale dynamo, as argued by Pakmor et al. (2017). In contrast, the magnetic field strength in the outskirts of the galaxies (r $\gtrsim$10 kpc) increases and decreases almost exactly with $\rho^{2/3}$. This implies that the field strength at these radii depends almost exclusively on flux conservation, and that there is no dynamo in action. This observation is supported by the lack of amplification seen after the merger, despite the passing of several Gyr.

The Auriga galaxies, which evolved in relative isolation, showed azimuthally-dominant magnetic fields at $z = 0$ (Pakmor et al., 2017, 2018). We may ask whether our merger remnants show the same configuration. To check this, we consider the fraction of the magnetic field energy in the radial, azimuthal, and vertical components. These are shown in radial bins as a function of time in rows 2 – 4 of Fig. 3.20, respectively. Observing the images, it is immediately clear that only the galaxy in simulation 1526-3M shows an azimuthally-dominant magnetic field post-merger. Interestingly, 1330-3M shows an azimuthally-dominant magnetic field pre-merger. This shows that, in our simulations, mergers can both create and destroy such a configuration. The azimuthally-dominant field has also not produced a stronger magnetic field compared to the other galaxies. This suggests that the production of this field is a result of the gas dynamics, and is not the result of ordering by a dynamo.

We suggest that the main factor that affects the building of such a field is whether the galaxy has a stable orientation whilst it accretes its interior gas. To this end, in row 5 we show the mass of gas that is contained within an annular ring of depth $\pm$1 kpc of the midplane and with

[41] Neither of the cited simulations include an implementation of AGN feedback. Furthermore, only Kotarba et al. (2010) includes an implementation of stellar feedback, but this is treated implicitly through the Springel and Hernquist (2003) ISM model.

radial bounds of 2.5 kpc and 10 kpc from the galactic centre as a function of time. We neglect the inner 2.5 kpc of the disc so that we remain relatively unaffected by mass fluctuations due to AGN outbursts. We use the total gas mass in this ring as a proxy for the re-accretion of the gas onto the merger-remnant post-coalescence. In row 6, we show the angle of the stellar angular momentum vector from the z-axis (solid line) and in the x-y plane (dashed line) before the coordinate transformation described in Subsection 2.2.4. Grey shaded regions show times when our calculation of the stellar angular momentum vector has been affected by the galaxy undergoing a merger or significant tidal interaction[42]. We highlight these points to show that the remaining points are genuine re-orientations of the galactic disc in physical space. This physical reorientation is also evident in rows 2 – 4 by the magnetic energy fraction outside the disc transferring from one component to another. For example, the galaxy in simulation 1605-3M starts with its stellar angular momentum vector facing almost exactly in the negative z-direction[43]. The galaxy then re-orientates during the merger, such that its stellar angular momentum vector then aligns almost exactly with the $x-$axis. As a result, the magnetic field outside the disc, which previously had strong r and ϕ components, is transformed into a field that is dominant in the z component This process happens for every galaxy, but is especially clear here. Other relatively clear examples of this behaviour are 1526-3M at $z \approx 0.7$ and 1330-3 at $z \approx 0.4$.

From rows 5 and 6 of Fig. 3.20, it may be observed that only the galaxy in simulation 1526-3M accretes its interior gas whilst remaining in a relatively stable position. For the other simulations, 1330-3M has accreted most of its gas mass by the time the galaxy has a stable orientation, 1349-3M goes through an over-180° rotation in space whilst accreting gas, and 1605-3M does not become stable until the magnetic field has already been sufficiently amplified. Consequently, only 1526-3M generates an azimuthally-dominant magnetic field post-merger. This may have an important evolutionary impact on the galaxy. On comparison, with Fig. 3.17, we see that 1526-3M is the only galaxy that does not show enhanced black hole accretion rates compared with its hydrodynamic analogue. Furthermore, it is noticeable that the timing of the enhanced accretion in the other simulations correlates with the times at which the magnetic field is highly amplified. This implies that at these times the magnetic field is dynamically dominant[44] and is transporting gas to the black hole accretion zone.

The stellar angular momentum changes quickly during the merger, but shows remarkably smooth

[42] These events do not always significantly affect the circularity measurement, and so these regions are not the same as in Fig. 3.17.

[43] This also causes the chaotic behaviour of the dashed-line: the stellar angular momentum vector has almost no x or y component, and so small fluctuations of these components produce large changes to the angle in the x-y plane.

[44] We suggest further tests for this in Section 4.2.

transitions after this time. We may ask whether this a property introduced by the MHD physics by comparing the evolution of the stellar angular momentum vector to that of the galaxies in the hydrodynamic simulations. We do this in row 7 of Fig. 3.20. At first glance, the simulations that included MHD physics do indeed appear to show galaxies that are more stable than their hydrodynamic counterparts. However, this is explained by the evolution of the magnitude of the stellar angular momentum vector, plotted in row 8 of Fig. 3.20. The disc size in our MHD simulations is generally larger than in our hydrodynamic simulations. This translates to a larger total stellar angular momentum, providing stability to the orientation of the disc. This is supported by the fact that the galaxies with the most similar angular momentum evolution — those starting with prefix 1330-3 — show the least difference between their orientation evolution. In contrast, rapid changes in the stellar angular momentum orientation tend to happen when the magnitude of this vector is at its lowest — e.g. at 4 Gyr in 1349-3M, or generally for 1605-3M. We may therefore conclude that galaxies are indeed generally more stable in MHD simulations, but only for the reasons that we have previously identified. Considering this effect, and the inherent non-linearity in baryonic processes, it is interesting to see how close the galaxies end up in orientation between physics models. This shows that magnetic fields are only affecting the dynamics of dense gas. It also provides yet further support that our simulations are truly well-converged.

3.6.2 Examples of typical magnetic field configurations

During a merger, the magnetic field becomes almost fully random. As the disc begins to regrow, the magnetic field settles into particular configurations. It so happens, that these configurations fit into four main camps. We present some of the clearest examples of these configurations as slices in the x-y plane in Fig. 3.21. In doing so, we examine how the magnetic field affects the motion of the gas in the disc.

In the 1st row of Fig. 3.21, we observe a quadrupolar structure in the r and ϕ components[45] and a bipolar structure in the vertical component. As may be seen in Fig. 3.20, the components display roughly equal field strengths. This pattern is typical for all galaxies that do not display an azimuthally-dominant magnetic field. The configuration scales with the disc size, becoming less distinct at the downbending break in the gas density profile (see Subsection 3.4.2). The configuration becomes more stable with increased size, however, and is ultimately the most

[45] Coincidentally, mean-field dynamo theory also expects a quadrupolar magnetic field for differentially-rotating disc galaxies (Widrow, 2002). However, this configuration would be lie perpendicular to the midplane, rather than in the midplane, as we observe. This is not too concerning for us, as our simulations are not able to simulate a mean-field dynamo (see Subsection 2.1.3).

stable of all configurations shown here. At the centre of the galaxy, this configuration displays a strong radial component on the diagonal. These magnetic field lines act to channel gas towards the galactic centre, where it may be accreted by the central black hole.

When the magnetic field is not dynamically dominant, the field lines are dragged with the motion of the gas. This effect is particularly clear when the galaxy experiences a significant tidal interaction. The aftermath of such an event is seen in the 2nd row of Fig. 3.21. The field configuration for this galaxy previously appeared as in the 1st row, but has experienced a significant mixing of field lines due to the tidal interaction. As mentioned in Subsection 2.2.5, the impact parameter of the interacting galaxy is relatively large (~ 40 kpc from the galactic centre). Despite this, the galaxy has managed to generate a large amount of small-scale magnetic field structure. This shows that once the field has lost dynamical dominance, the field configurations become highly sensitive to a change of gravitational potential. From this configuration, we may also see that the existence of magnetic arms does not necessarily imply an azimuthally-dominant magnetic field. In general, small-scale components such as those presented here are not as stable as large-scale components.

The 3rd row of Fig. 3.21 shows galaxy 1526-3M at an early stage in the regrowth of its disc. Whilst the radial components are relatively unordered, there is already a clear dipole to be seen in the vertical component of the field. Both of these components are, however, dominated by the azimuthal component. Within the inner $\lesssim 5$ kpc, the field strength is very well-ordered, and has reached a consistent field strength of 20 μG – 30 μG. The combination of the enhanced field strengths and well-ordered field acts to keep gas moving on an azimuthal trajectory, thereby inhibiting the accretion of gas onto the central black hole. This supports the low accretion rates seen in Fig. 3.17 for this galaxy. As the magnetic field in this galaxy loses dynamical dominance, field lines from outside the disc are wound in due to differential rotation. This produces the spiral arms and magnetic field reversals shown in the 4th row. In this configuration, the same spiral structure is seen for all components of the magnetic field. This configuration is very similar to that shown in Fig. 8 of Pakmor et al. (2018). This is perhaps not surprising, as Pakmor et al. (2018) investigated relatively isolated galaxies, which are highly likely to have had a stable stellar angular momentum evolution, as discussed in Subsection 3.6.1.

Under standard dynamo terminology, the configuration shown in the 4th row is called a bisymmetric spiral structure (BSS) Krause et al. (1989). A common argument used in favour of a mean-field dynamo over primordial amplification is that the spiral magnetic field structure in observed galaxies is generally rather loosely wound, instead of being tightly wound as seen here. This implies that the magnetic field is being continuously generated by some mechanism (see e.g.

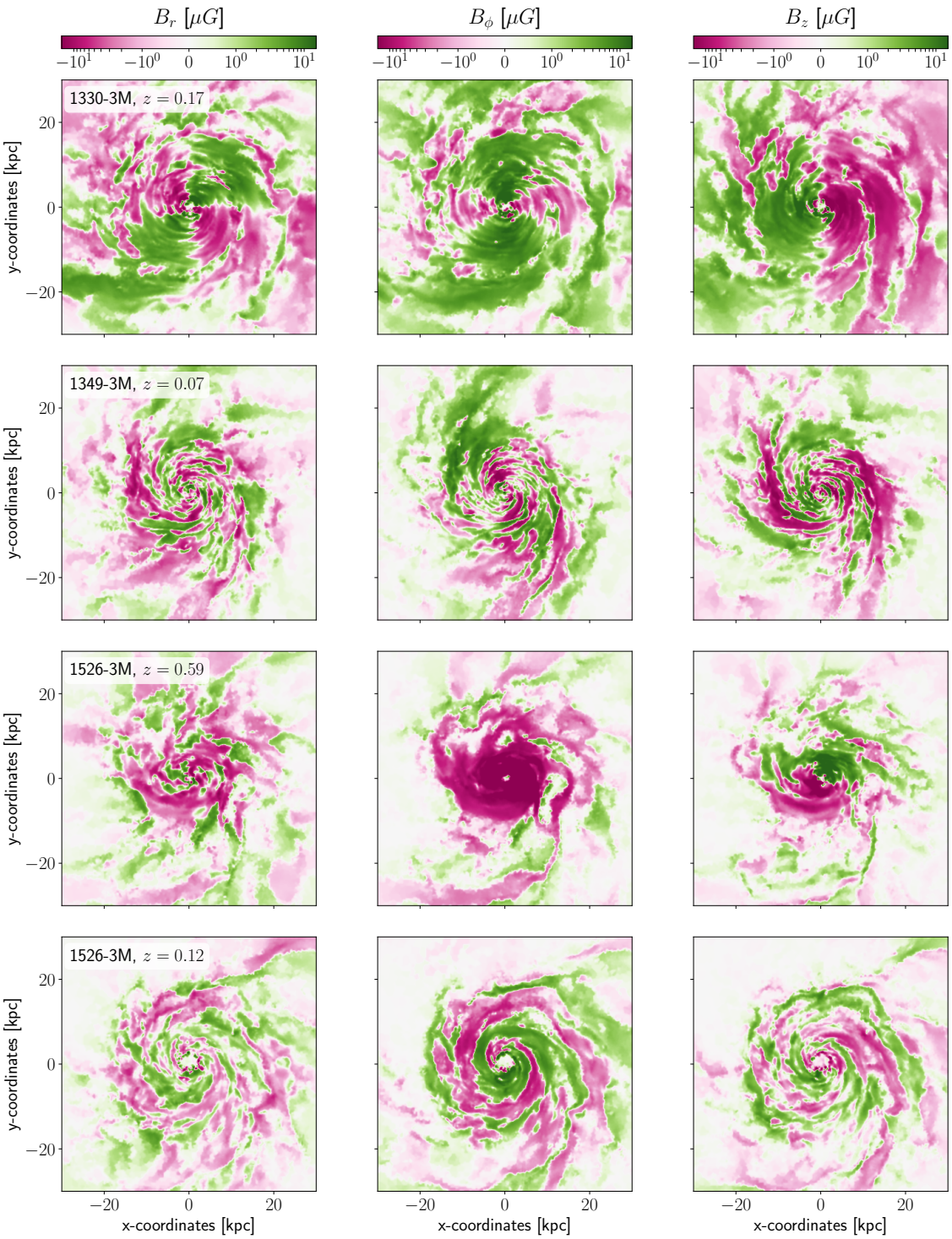

Figure 3.21: Slices showing the radial (left panel), azimuthal (middle panel), and vertical (right panel) components of the magnetic field vector when given in cylindrical components for the main galaxy in a simulation (as defined in Section 2.2.3). The simulation name and redshift is seen in the top left-hand corner of the leftmost panel. B_r is positive pointing away from the galactic centre, B_ϕ is positive in the clockwise direction, and B_z is positive pointing above the disc. The bounds of the colour bar are ± 15 μG. Slices were created as described in Subsection 3.3.3. The magnetic field configurations presented here are characteristic of those seen throughout the simulations. Configurations are not static, and depend on the dynamics of the accreted gas. The azimuthally-dominant magnetic field seen in 1526-3M starts in the configuration seen in the 3rd row, before developing into that seen in the 4th row. Small scale structure generally forms after large scale structure once a disc is established and is not stable.

Widrow, 2002). It has been argued in the past, however, that, as observations take the average of the field, the fine-scale structure of the field may actually be similar to that shown here (Howard and Kulsrud, 1997). As yet, observations are still insufficient to prove this one way or the other (Beck and Wielebinski, 2013).

We conclude from Fig. 3.20 and Fig. 3.21 that mergers can lead to a substantial amplification of the magnetic field in our simulated galaxies for several Gyr after coalescence. During this time, the magnetic field develops a quadrupolar or azimuthally-dominant configuration. The type of configuration generated has important ramifications for the evolution of the galaxy. If the configuration is quadrupolar, radial magnetic field lines transport gas towards the black hole, resulting in enhanced AGN feedback in the galaxy. If the configuration is azimuthal, the field lines act against such transport. The generation of either configuration depends on the spatial stability of the galaxy during the initial accretion onto the merger remnant, with a stable orientation producing an azimuthally-dominant field.

Chapter 4

Discussion

In this chapter we discuss caveats to the main work (Section 4.1) and suggest possible extensions that can be made to this thesis in the future (Section 4.2).

4.1 Caveats

First and foremost, this research has been an investigation into the importance of including MHD physics in the Auriga galaxy formation model. Whilst this model has been shown to be able to produce a range of current-day observables (see Subsection 2.1.4), we should be cautious before implying a link between what we have seen in our simulations and what takes place in reality. We must also note that we have chosen a set-up that, whilst cosmologically-consistent, should have shown magnetic fields at their most effective:

- The galaxies before the merger had large, gas-rich discs and consequently strong, well-ordered magnetic fields.
- In hydrodynamic simulations, the mergers had already been shown to produce high gas densities (Sparre and Springel, 2016). As the gas-component is frozen to the magnetic field lines in ideal MHD, it was therefore expected that we would see correspondingly high magnetic field strengths.
- Finally, in hydrodynamic simulations the galaxies were able to rebuild large, gas-rich discs after the merger (Sparre and Springel, 2017). The rebuilding process is also dependent on the gas dynamics, and hence is one where magnetic fields could have an impact.

In contrast, smaller and more gas-poor progenitors would have shown generally lower initial

magnetic field strengths, reducing their impact. The impact of magnetic fields would also have been reduced in the 'traditional' merger scenario, where the gas is expelled from the galaxy post-merger. Consequently, whilst including magnetic fields has had a significant effect in our mergers, we can not conclude that magnetic fields are important in mergers *generally*. This is especially true for mergers of more massive galaxies, which are generally more gas-poor (see sections 1.2 and 1.3).

We also point out that, whilst we have shown that our numerical methods are supported by previous work (see Section 2.1) and that they produce some expected results when applied within our simulations (see Section 3.1), there are still remaining issues related to numerical accuracy and physical fidelity that could affect our results. In particular, as these factors are key to our results, we highlight some potential issues with the current AGN feedback and MHD implementations:

- *AGN implementation:* Black hole accretion in our simulations was built on the Bondi-Hoyle-Lyttleton model. As already stated, this treatment is often too simplistic as it neglects the angular momentum of the gas (see Subsection 1.2). Perhaps more importantly, it is only strictly accurate within the Bondi-Hoyle radius[1], $r_{\rm B}$, which we do not resolve. This could be problematic, as Curtis and Sijacki (2015) have shown that resolving this radius affects the behaviour of the model. Using an aggressive refinement routine near the black hole, they found that once cell radii were brought below $r_{\rm B}$ thermally-coupled gas rose above the disc in a relatively collimated fashion, rather than disrupting the central regions of the disc as happens in our simulations[2]. This has clear implications for our work, as we found that the existence of such disruption was a likely factor behind the differing morphologies produced.

- *MHD implementation:* Whilst the Powell divergence cleaning scheme used has been shown to produce the correct results in a number of test cases, it is not as accurate as the constrained transport schemes now available, which are able to fulfil the divergence constraint to machine precision. This is important as isolated galaxy simulations that used such CT schemes have been shown to produce magnetic fields that differ in geometry and saturate at a lower level (see Subsection 2.1.3). Our MHD implementation also used the ideal MHD approximation, meaning that the magnetic field topology in our simulations was fixed. This means that we were unable to replicate any dynamo action that operates through transformation of the topology. This is particular relevant for the mean-field dynamo, which is

[1]This is equal to $GM_{\rm BH}/(c_\infty^2 + v^2)$, where G is the gravitational constant, $M_{\rm BH}$ is the mass of the black hole, c_∞ is the sound speed at infinity, and v is the relative velocity between the black hole and gas at infinity.

[2]These simulations were, however, hydrodynamic.

believed to reorder the large-scale field to become azimuthally-dominant in the disc (see Subsection 1.4). During our analysis, we suggested that radial magnetic fields in our simulations could be channelling gas towards the centre of the galaxy, powering the observed increase in AGN feedback. If this is a correct assessment, a reordering of the field in the disc could significantly disrupt this mechanism. Including non-ideal MHD effects to allow topology changes could also affect the magnetic field strengths observed, although it is difficult to say with certainty how: dynamo action would act to increase the magnetic field strength, but resistive MHD would allow magnetic fields to lose energy through diffusion and magnetic reconnection.

Resistive MHD codes for AREPO do now exist (Marinacci et al., 2018a). However, these are not yet appropriate for galaxy simulations, as they require a resolution such that the physical resistivity is higher than the numerical resistivity. This resolution is several orders of magnitude higher than that currently achievable in isolated simulations, let alone in zoom-in simulations. Reaching this resolution would also require a change to many other parts of the simulation; by this point we would be able to resolve individual gas clouds. This would require an explicit model of the ISM, as opposed to the implicit scheme that is currently implemented through the Springel and Hernquist (2003) model. Whilst resolution is above the giant molecular cloud scale, resistivity could be implemented through subgrid models. Indeed, Hanasz et al. (2009), who used subgrid models of turbulent reconnection and anomalous resistivity[3], showed reasonably successful results implementing this in isolated disc simulations. No convergence tests were shown for these simulations, however.

4.2 Future extensions

During this thesis, we made a series of conjectures that attempted to explain the phenomena we observed. In future projects, these conjectures could be more thoroughly investigated in the following way:

- *Transport of gas:* We suggested that the increased black hole masses seen in MHD simulations could be a result of radial magnetic field lines transporting gas to the inner regions of the disc. Radial profiles of the kinetic, turbulent, thermal, and magnetic energy densities in the disc would show whether the magnetic fields were truly dynamically dominant in these regions during the main period of accretion. Such analysis is technically straightforward,

[3] A form of resistivity where the magnetic diffusivity is a function of the current density.

but was beyond the scope of this thesis.

- *Disruption by AGN feedback:* We suggested that increased AGN feedback was the primary reason behind the different morphologies produced. This could be checked by re-running our MHD simulations, with the efficiency parameters in the energy injection equation (see Subsection 2.1.4) reduced such that the galaxies displayed sufficiently low winds after the merger[4].

- *Accelerated coalescence:* We observed that galaxies in MHD simulations coalesced faster than their hydrodynamic analogues and that this was particularly the case for inspiralling galaxies. Further inspiralling galaxies could be investigated to confirm this effect and explain its origin.

Our work can also be extended to provide more data that may be compared with observations. Over the next few years, a large amount of radio data will be produced from a broad range of telescopes including MeerKAT, the Low-Frequency Array (LOFAR), the Karl G. Jansky Very Large Array (VLA), the Australian Square Kilometre Array Pathfinder (ASKAP), and the Square Kilometre Array (SKA) (Haverkorn et al., 2019). When it comes online, the SKA, in particular, is likely to discover thousands of pulsars in the Milky Way, enormously increasing the number of Faraday rotation measurements. Furthermore, it will be able to resolve magnetic field structure in external galaxies with a spatial resolution of < 100 pc (Beck et al., 2015). It would therefore be useful to produce mock radio observations, as in Marinacci et al. (2018b), and mock Faraday rotation maps, as in Pakmor et al. (2018), for comparison. In this way, we can better identify the differences that exist between our models and reality.

It would also be interesting to use our simulations to investigate whether the equiparitition condition holds throughout the mergers. This would naturally have important consequences for inferences made from synchrotron emission observations (see Section 1.4). This could be achieved by including a cosmic ray implementation in our simulations. Such implementations already exist for AREPO (Pakmor et al., 2016; Pfrommer et al., 2017) and have been applied to the isolated, but still cosmological, galaxies from the Auriga suite (Buck et al., 2019). Here it was found that cosmic rays could strongly affect the properties of the CGM. This effect, combined with the extra cosmic-ray pressure term, is likely to impact the results of our simulations. Interestingly, Buck et al. (2019) also found that their cosmic ray implementations could affect the morphology and angular momentum distribution of the galaxy whilst leaving the bulk properties of the galaxy mostly untouched. This result has clear similarities with our own work.

[4]AGN feedback is a notoriously non-linear effect, however, and the other morphologies may prove difficult to replicate exactly.

Chapter 5

Conclusions

During this thesis, we have investigated the impact of magnetic fields on galaxy mergers and vice versa. We have done this through comparison of hydrodynamic and magnetohydrodynamic simulations of mergers based on the same initial conditions. Our simulations were fully cosmologically-consistent and used a state-of-the-art zoom-in code. This provided high resolution within a broad distance of the simulated galaxies, but still allowed us to include accurate external effects due to cosmological structure. To the best of our knowledge, this is the first time that MHD zoom-in simulations have been used to study mergers. Naturally, we required an extremely high resolution in order to revolve the small-scale physics involved. In our highest resolution simulations, we achieved a dark matter mass resolution that was $\sim$38.5 times finer than in the original Illustris simulation and $\sim$1.8 times finer than in the standard resolution level in the Auriga simulations (i.e. their Level 4).

The evolution and impact of galactic magnetic fields is an extremely complex problem and an accurate implementation of the physics involved is technically challenging. In order to increase the reliability of our results, we therefore built upon previously proven work. In particular, our simulations employed:

- The moving-mesh code AREPO, which has been shown to have significantly better numerical accuracy than competing codes when applied to a range of relevant physical problems.
- The Auriga galaxy formation model, which includes physically-motivated subgrid models and an MHD implementation that has been shown to sufficiently fulfil the divergence constraint even in dynamic environments.

The Auriga model was also chosen as it does not require the retuning of free parameters between resolution levels in order to produce broadly convergent results. We have shown that this conver-

gence may still be seen in our own simulations, despite the increased kinematic complexity. This result implies that our simulations were dependent on the choice of physics included, rather than on the numerical implementation. We complemented this result by showing that our simulations also produced values for observables that were both realistic and inline with previous numerical work. This is, however, not to say that our results are equivalent with previous work. Whilst other simulations of galaxy evolution have shown a mild to negligible impact from the inclusion of MHD physics, our simulations show a rather dramatic impact. We list our major conclusions below:

- During a merger, the average magnetic field strength in the inner $\lesssim 5$ kpc of the disc can be boosted by up to an order of magnitude. At the same time, the field outside this range may drop by an order of magnitude. These effects are typically apparent for at least 1.5 Gyr after coalescence and fade with the rebuilding of the disc.

- Discs that are stable when they reaccrete their gas can form azimuthally-dominant magnetic fields. These fields eventually develop large spiral structures with clear reversals. When the disc is not stable during accretion, the magnetic field eventually forms a quadrupolar structure in the disc-plane instead. Significant small-scale structure in the field can be introduced by minor tidal interactions. The configuration of the magnetic field post-merger is independent of that which the galaxy had pre-merger.

- We see significantly increased central black hole masses for galaxies that formed quadrupolar fields. We conjecture that the magnetic fields are powering this growth by driving gas into the accretion region. We also conjecture that the resultant increased AGN feedback is the principle driver of the differing morphologies produced by the two physics models.

- In contrast to their hydrodynamic analogues, MHD simulations produced galaxies that were generally extended with significant spiral arm structure. Gas in these galaxies generally had a flocculent structure with a shallow radial gradient. Galaxies from hydrodynamic simulations, on the other hand, were systematically smaller, and frequently showed large stellar bars and rings. Gas in these galaxies formed a thinner disc and showed a sharp cut-off in density at the disc edge. Analysis of isolated galaxies showed similar, but less marked, differences, implying these features are an outcome of mergers. This illustrates the importance of including MHD physics when simulating gas-rich major mergers.

- In galaxies from hydrodynamic simulations, the gas dynamics in the centre of the disc were generally quieter. This was correlated with reduced AGN activity. The added stability allowed for the formation of long-lasting stellar bars which, in turn, torqued the accreting

gas during the disc regrowth phase. We have identified this mechanism as the primary cause of the stellar rings and reduced disc sizes seen for galaxies in hydrodynamic simulations.

- The dense star formation in the bar and stellar rings in these galaxies also resulted in highly efficient stellar feedback. This feedback removed gas from the galaxy more effectively than AGN feedback did in MHD simulations. Despite this, no significant change was identified in the star formation history produced by each physics model. Similarly, there were negligible differences in the disc evolution as measured through the stellar mass fraction in the disc (D/T).

- The differences between MHD and hydrodynamic simulations noted above were *only seen with increased resolution*. We have shown that our simulations were generally numerically convergent given the same physics model. Divergence between models therefore points to the resolution of sufficiently small-scale physics.

We have performed simulations over three levels of resolution, with eight simulations performed at the very highest resolution. We have also included brief analysis of eight simulations from the Auriga suite, which provided supporting data. We therefore believe that our observations are robust. We have, however, discussed future work that could be done to both test the validity of our inferences and increase the physical fidelity of our simulations. With resolution in cosmological simulations seemingly ever increasing, we look forward to seeing whether similar results are found in future work. Certainly, this is not the last word to be said about the role of MHD in mergers and galaxy evolution.

Bibliography

Abadi, M. G., Navarro, J. F., Steinmetz, M., and Eke, V. R. (2003). *Simulations of Galaxy Formation in a Λ Cold Dark Matter Universe. II. The Fine Structure of Simulated Galactic Disks.* ApJ, 597(1):21–34.

Abel, T., Bryan, G. L., and Norman, M. L. (2002). *The Formation of the First Star in the Universe.* Science, 295(5552):93–98.

Adebahr, B., Krause, M., Klein, U., Heald, G., and Dettmar, R. J. (2017). *M 82 - A radio continuum and polarisation study. II. Polarisation and rotation measures.* A&A, 608:A29.

Adebahr, B., Krause, M., Klein, U., et al. (2013). *M 82 - A radio continuum and polarisation study. I. Data reduction and cosmic ray propagation.* A&A, 555:A23.

Agertz, O. and Kravtsov, A. V. (2016). *The Impact of Stellar Feedback on the Structure, Size, and Morphology of Galaxies in Milky-Way-sized Dark Matter Halos.* ApJ, 824(2):79.

Agertz, O., Moore, B., Stadel, J., et al. (2007). *Fundamental differences between SPH and grid methods.* MNRAS, 380(3):963–978.

Arshakian, T. G., Beck, R., Krause, M., and Sokoloff, D. (2009). *Evolution of magnetic fields in galaxies and future observational tests with the Square Kilometre Array.* A&A, 494(1):21–32.

Babul, A. and Ferguson, H. C. (1996). *Faint Blue Galaxies and the Epoch of Dwarf Galaxy Formation.* ApJ, 458:100.

Balbus, S. A. and Hawley, J. F. (1991). *A Powerful Local Shear Instability in Weakly Magnetized Disks. I. Linear Analysis.* ApJ, 376:214.

Bardeen, J. M., Bond, J. R., Kaiser, N., and Szalay, A. S. (1986). *The Statistics of Peaks of Gaussian Random Fields.* ApJ, 304:15.

Barnes, J. and Hut, P. (1986). *A hierarchical O(N log N) force-calculation algorithm.* Nature, 324(6096):446–449.

Barnes, J. E. (1988). *Encounters of Disk/Halo Galaxies.* ApJ, 331:699.

Barnes, J. E. and Hernquist, L. E. (1991). *Fueling Starburst Galaxies with Gas-rich Mergers.* ApJ, 370:L65.

Bastian, N., Covey, K. R., and Meyer, M. R. (2010). *A Universal Stellar Initial Mass Function? A Critical Look at Variations.* ARA&A, 48:339–389.

Bauer, A. and Springel, V. (2012). *Subsonic turbulence in smoothed particle hydrodynamics and moving-mesh simulations.* MNRAS, 423(3):2558–2578.

Beck, R. (2000). *Magnetic fields in normal galaxies.* Royal Society of London Transactions Series A, 358:777–796.

Beck, R. (2004). *The Role of Magnetic Fields in Spiral Galaxies.* Ap&SS, 289(3):293–302.

Beck, R. (2007). *Magnetism in the spiral galaxy NGC 6946: magnetic arms, depolarization rings, dynamo modes, and helical fields.* A&A, 470(2):539–556.

Beck, R. (2009). *Measuring interstellar magnetic fields by radio synchrotron emission.* IAU Symposium, 259:3–14.

Beck, R. (2015). *Magnetic fields in spiral galaxies.* A&A Rev., 24:4.

Beck, R., Bomans, D., Colafrancesco, S., et al. (2015). *Structure, dynamical impact and origin of magnetic fields in nearby galaxies in the SKA era.* Proceedings of Advancing Astrophysics with the Square Kilometre Array.

Beck, R., Brandenburg, A., Moss, D., Shukurov, A., and Sokoloff, D. (1996). *Galactic Magnetism: Recent Developments and Perspectives.* ARA&A, 34:155–206.

Beck, R. and Hoernes, P. (1996). *Magnetic spiral arms in the galaxy NGC6946.* Nature, 379(6560):47–49.

Beck, R., Klein, U., and Krause, M. (1985). *M 81 at high radio frequencies.* A&A, 152:237–249.

Beck, R. and Wielebinski, R. (2013). *Magnetic Fields in Galaxies.* Planets, Stars and Stellar Systems. Volume 5: Galactic Structure and Stellar Populations, 5:641.

Behroozi, P., Knebe, A., Pearce, F. R., et al. (2015). *Major mergers going Notts: Challenges for modern halo finders.* MNRAS, 454(3):3020–3029.

Behroozi, P. S., Wechsler, R. H., and Conroy, C. (2013). *The Average Star Formation Histories of Galaxies in Dark Matter Halos from z = 0-8.* ApJ, 770(1):57.

Bell, E. F., Phleps, S., Somerville, R. S., et al. (2006). *The Merger Rate of Massive Galaxies.* ApJ, 652(1):270–276.

Biermann, L. (1950). *Über den Ursprung der Magnetfelder auf Sternen und im interstellaren Raum.* Zeitschrift Naturforschung Teil A, 5:65.

Binney, J. (1978). *On the rotation of elliptical galaxies.* MNRAS, 183:501–514.

Blanton, M. R., Bershady, M. A., Abolfathi, B., et al. (2017). *Sloan Digital Sky Survey IV: Mapping the Milky Way, Nearby Galaxies, and the Distant Universe.* AJ, 154:28.

Blázquez-Calero, G., Florido, E., Pérez, I., et al. (2019). *Structural and photometric properties of barred galaxies from the Auriga cosmological simulations.* MNRAS, page 2715.

Blumenthal, G. R., Faber, S. M., Primack, J. R., and Rees, M. J. (1984). *Formation of galaxies and large-scale structure with cold dark matter.* Nature, 311:517–525.

Bondi, H. (1952). *On spherically symmetrical accretion.* MNRAS, 112:195.

Bondi, H. and Hoyle, F. (1944). *On the mechanism of accretion by stars.* MNRAS, 104:273.

Bournaud, F. and Combes, F. (2002). *Gas accretion on spiral galaxies: Bar formation and renewal.* A&A, 392:83–102.

Bower, R. G., Lucey, J. R., and Ellis, R. S. (1992). *Precision photometry of early-type galaxies in the Coma and Virgo clusters : a test of the universality of the colour-magnitude relation - I. The data.* MNRAS, 254:589–600.

Brandenburg, A. and Subramanian, K. (2005). *Astrophysical magnetic fields and nonlinear dynamo theory.* Phys. Rep., 417(1-4):1–209.

Bromm, V. and Loeb, A. (2003). *Formation of the First Supermassive Black Holes.* ApJ, 596(1):34–46.

Bruzual, G. and Charlot, S. (2003). *Stellar population synthesis at the resolution of 2003.* MNRAS, 344(4):1000–1028.

Buck, T., Pfrommer, C., Pakmor, R., Grand, R. J. J., and Springel, V. (2019). *The effects of cosmic rays on the formation of Milky Way-like galaxies in a cosmological context.* arXiv e-prints, page arXiv:1911.00019.

Buta, R. and Combes, F. (1996). *Galactic Rings.* Fund. Cosmic Phys., 17:95–281.

Buta, R. J., Byrd, G. G., and Freeman, T. (2004). *A Hubble Space Telescope Study of Star Formation in the Inner Resonance Ring of NGC 3081.* AJ, 127(4):1982–2001.

Carucci, I. P., Sparre, M., Hansen, S. H., and Joyce, M. (2014). *Particle ejection during mergers of dark matter halos.* J. Cosmol. Astropart. Phys, 2014(6):057.

Ceverino, D., Klypin, A., Klimek, E. S., et al. (2014). *Radiative feedback and the low efficiency of galaxy formation in low-mass haloes at high redshift.* MNRAS, 442(2):1545–1559.

Chabrier, G. (2003). *Galactic Stellar and Substellar Initial Mass Function.* PASP, 115(809):763–795.

Chabrier, G., Hennebelle, P., and Charlot, S. (2014). *Variations of the Stellar Initial Mass Function in the Progenitors of Massive Early-type Galaxies and in Extreme Starburst Environments.* ApJ, 796(2):75.

Chandrasekhar, S. (1942). *Principles of stellar dynamics.* The University of Chicago Press.

Chandrasekhar, S. and Fermi, E. (1953). *Magnetic Fields in Spiral Arms.* ApJ, 118:113.

Chaves-Montero, J., Angulo, R. E., Schaye, J., et al. (2016). *Subhalo abundance matching and assembly bias in the EAGLE simulation.* MNRAS, 460(3):3100–3118.

Chyży, K. T. and Buta, R. (2008). *Strong magnetic spiral pattern in a ringed galaxy NGC 4736.* IAU Symposium, 245:133–134.

Clowe, D., Gonzalez, A., and Markevitch, M. (2004). *Weak-Lensing Mass Reconstruction of the Interacting Cluster 1E 0657-558: Direct Evidence for the Existence of Dark Matter.* ApJ, 604(2):596–603.

Cole, S., Percival, W. J., Peacock, J. A., et al. (2005). *The 2dF Galaxy Redshift Survey: power-spectrum analysis of the final data set and cosmological implications.* MNRAS, 362(2):505–534.

Combes, F., Young, L. M., and Bureau, M. (2007). *Molecular gas and star formation in the SAURON early-type galaxies.* MNRAS, 377(4):1795–1807.

Couch, W. J., Barger, A. J., Smail, I., Ellis, R. S., and Sharples, R. M. (1998). *Morphological Studies of the Galaxy Populations in Distant "Butcher-Oemler" Clusters with the Hubble Space Telescope. II. AC 103, AC 118, and AC 114 at Z = 0.31.* ApJ, 497(1):188–211.

Crocker, A. F., Bureau, M., Young, L. M., and Combes, F. (2011). *Molecular gas and star formation in early-type galaxies.* MNRAS, 410(2):1197–1222.

Curtis, M. and Sijacki, D. (2015). *Resolving flows around black holes: numerical technique and applications.* MNRAS, 454(4):3445–3463.

Davis, Leverett, J. and Greenstein, J. L. (1951). *The Polarization of Starlight by Aligned Dust Grains.* ApJ, 114:206.

Davis, M., Efstathiou, G., Frenk, C. S., and White, S. D. M. (1985). *The evolution of large-scale structure in a universe dominated by cold dark matter.* ApJ, 292:371–394.

de Bernardis, P., Ade, P. A. R., Bock, J. J., et al. (2000). *A flat Universe from high-resolution maps of the cosmic microwave background radiation.* Nature, 404(6781):955–959.

de Vaucouleurs, G. (1948). *Recherches sur les Nébuleuses Extragalactiques.* Annales d'Astrophysique, 11:247.

de Vaucouleurs, G. (1963). *Revised Classification of 1500 Bright Galaxies.* ApJS, 8:31.

Deason, A. J., McCarthy, I. G., Font, A. S., et al. (2011). *Mismatch and misalignment: dark haloes and satellites of disc galaxies.* MNRAS, 415(3):2607–2625.

Di Matteo, T., Springel, V., and Hernquist, L. (2005). *Energy input from quasars regulates the growth and activity of black holes and their host galaxies.* Nature, 433(7026):604–607.

Dib, S. (2011). *Feedback-regulated Star Formation: Implications for the Kennicutt-Schmidt Law.* ApJ, 737(1):L20.

Dolag, K., Bartelmann, M., and Lesch, H. (1999). *SPH simulations of magnetic fields in galaxy clusters.* A&A, 348:351–363.

Dolag, K., Grasso, D., Springel, V., and Tkachev, I. (2005). *Constrained simulations of the magnetic field in the local Universe and the propagation of ultrahigh energy cosmic rays.* J. Cosmol. Astropart. Phys, 2005(1):009.

Draper, A. R. and Ballantyne, D. R. (2012). *The Merger-triggered Active Galactic Nucleus Contribution to the Ultraluminous Infrared Galaxy Population.* ApJ, 753(2):L37.

Dressler, A. (1980). *Galaxy morphology in rich clusters: implications for the formation and evolution of galaxies.* ApJ, 236:351–365.

Drzazga, R. T., Chyży, K. T., Jurusik, W., and Wiórkiewicz, K. (2011). *Magnetic field evolution in interacting galaxies.* A&A, 533:A22.

Dubois, Y. and Teyssier, R. (2010). *Magnetised winds in dwarf galaxies.* A&A, 523:A72.

Durrer, R. and Neronov, A. (2013). *Cosmological magnetic fields: their generation, evolution and observation.* A&A Rev., 21:62.

Eisenstein, D. J., Zehavi, I., Hogg, D. W., et al. (2005). *Detection of the Baryon Acoustic Peak in the Large-Scale Correlation Function of SDSS Luminous Red Galaxies.* ApJ, 633(2):560–574.

Evans, C. R. and Hawley, J. F. (1988). *Simulation of Magnetohydrodynamic Flows: A Constrained Transport Model.* ApJ, 332:659.

Faber, S. M. and Gallagher, J. S. (1976). *H I in early-type galaxies. II. Mass loss and galactic winds.* ApJ, 204:365–378.

Faucher-Giguère, C.-A., Lidz, A., Zaldarriaga, M., and Hernquist, L. (2009). *A New Calculation of the Ionizing Background Spectrum and the Effects of He II Reionization.* ApJ, 703(2):1416–1443.

Fermi, E. (1949). *On the Origin of the Cosmic Radiation.* Physical Review, 75(8):1169–1174.

Ferrarese, L. and Merritt, D. (2000). *A Fundamental Relation between Supermassive Black Holes and Their Host Galaxies.* ApJ, 539(1):L9–L12.

Ferrière, K. M. (2001). *The interstellar environment of our galaxy.* Reviews of Modern Physics, 73(4):1031–1066.

Freeman, K. C. (1970). *On the Disks of Spiral and S0 Galaxies.* ApJ, 160:811.

Gebhardt, K., Bender, R., Bower, G., et al. (2000). *A Relationship between Nuclear Black Hole Mass and Galaxy Velocity Dispersion.* ApJ, 539(1):L13–L16.

Genel, S., Vogelsberger, M., Nelson, D., et al. (2013). *Following the flow: tracer particles in astrophysical fluid simulations.* MNRAS, 435(2):1426–1442.

Genel, S., Vogelsberger, M., Springel, V., et al. (2014). *Introducing the Illustris project: the evolution of galaxy populations across cosmic time.* MNRAS, 445(1):175–200.

Geng, A., Kotarba, H., Bürzle, F., et al. (2012). *Magnetic field amplification and X-ray emission in galaxy minor mergers.* MNRAS, 419(4):3571–3589.

Gerhard, O. E. (1981). *N-body simulations of disc-halo galaxies - Isolated systems, tidal interactions and merging.* MNRAS, 197:179–208.

Gnedin, N. Y., Ferrara, A., and Zweibel, E. G. (2000). *Generation of the Primordial Magnetic Fields during Cosmological Reionization.* ApJ, 539(2):505–516.

Gnedin, N. Y. and Kravtsov, A. V. (2011). *Environmental Dependence of the Kennicutt-Schmidt Relation in Galaxies.* ApJ, 728(2):88.

Grand, R. J. J., Bustamante, S., Gómez, F. A., et al. (2018). *Origin of chemically distinct discs in the Auriga cosmological simulations.* MNRAS, 474(3):3629–3639.

Grand, R. J. J., Gómez, F. A., Marinacci, F., et al. (2017). *The Auriga Project: the properties and formation mechanisms of disc galaxies across cosmic time.* MNRAS, 467(1):179–207.

Gunawardhana, M. L. P., Hopkins, A. M., Sharp, R. G., et al. (2011). *Galaxy and Mass Assembly (GAMA): the star formation rate dependence of the stellar initial mass function.* MNRAS, 415(2):1647–1662.

Hanasz, M., Wóltański, D., and Kowalik, K. (2009). *Global Galactic Dynamo Driven by Cosmic Rays and Exploding Magnetized Stars.* ApJ, 706(1):L155–L159.

Häring, N. and Rix, H.-W. (2004). *On the Black Hole Mass-Bulge Mass Relation.* ApJ, 604(2):L89–L92.

Haverkorn, M., Machida, M., and Akahori, T. (2019). *Workshop Summary "The Power of Faraday Tomography".* Galaxies, 7(1):26.

Heckman, T. M. and Best, P. N. (2014). *The Coevolution of Galaxies and Supermassive Black Holes: Insights from Surveys of the Contemporary Universe.* ARA&A, 52:589–660.

Heesen, V., Beck, R., Krause, M., and Dettmar, R. J. (2011). *Cosmic rays and the magnetic field in the nearby starburst galaxy NGC 253 III. Helical magnetic fields in the nuclear outflow.* A&A, 535:A79.

Heiles, C. (1996). *The Local Direction and Curvature of the Galactic Magnetic Field Derived from Starlight Polarization.* ApJ, 462:316.

Heiles, C. and Robishaw, T. (2009). *Zeeman splitting in the diffuse interstellar medium-The Milky Way and beyond.* IAU Symposium, 259:579–590.

Heitmann, K., Lukić, Z., Fasel, P., et al. (2008). *The cosmic code comparison project.* Computational Science and Discovery, 1(1):015003.

Heitsch, F., Zweibel, E. G., Slyz, A. D., and Devriendt, J. E. G. (2004). *Turbulent Ambipolar Diffusion: Numerical Studies in Two Dimensions.* ApJ, 603(1):165–179.

Hildebrand, R. H. (1988). *Magnetic fields and stardust.* QJRAS, 29:327–351.

Hinshaw, G., Larson, D., Komatsu, E., et al. (2013). *Nine-year Wilkinson Microwave Anisotropy Probe (WMAP) Observations: Cosmological Parameter Results.* ApJS, 208(2):19.

Hopkins, A. M. (2018). *The Dawes Review 8: Measuring the Stellar Initial Mass Function.* PASA, 35:39.

Hopkins, P. F., Chan, T. K., Garrison-Kimmel, S., et al. (2019). *But What About Cosmic Rays, Magnetic Fields, Conduction, & Viscosity in Galaxy Formation.* MNRAS, page 2993.

Hopkins, P. F., Hernquist, L., Cox, T. J., and Kereš, D. (2008). *A Cosmological Framework for the Co-Evolution of Quasars, Supermassive Black Holes, and Elliptical Galaxies. I. Galaxy Mergers and Quasar Activity.* ApJS, 175(2):356–389.

Hopkins, P. F., Kereš, D., Oñorbe, J., et al. (2014). *Galaxies on FIRE (Feedback In Realistic Environments): stellar feedback explains cosmologically inefficient star formation.* MNRAS, 445(1):581–603.

Hopkins, P. F. and Quataert, E. (2011). *An analytic model of angular momentum transport by gravitational torques: from galaxies to massive black holes.* MNRAS, 415(2):1027–1050.

Hopkins, P. F., Quataert, E., and Murray, N. (2012). *Stellar feedback in galaxies and the origin of galaxy-scale winds.* MNRAS, 421(4):3522–3537.

Hopkins, P. F., Wetzel, A., Kereš, D., et al. (2018). *FIRE-2 simulations: Physics versus numerics in galaxy formation.* MNRAS, 480(1):800–863.

Howard, A. M. and Kulsrud, R. M. (1997). *The Evolution of a Primordial Galactic Magnetic Field.* ApJ, 483(2):648–665.

Hubble, E. (1926). *No. 324. Extra-galactic nebulae.* Contributions from the Mount Wilson Observatory / Carnegie Institution of Washington, 324:1–49.

Hubble, E. P. (1927). *The classification of spiral nebulae.* The Observatory, 50:276–281.

Hubble, E. P. (1936). *Realm of the Nebulae.* Yale University Press.

Ikeuchi, S. and Ostriker, J. P. (1986). *Evolution of the Intergalactic Medium: What Happened during the Epoch Z = 3–10?* ApJ, 301:522.

Jarosik, N., Bennett, C. L., Dunkley, J., et al. (2011). *Seven-year Wilkinson Microwave Anisotropy Probe (WMAP) Observations: Sky Maps, Systematic Errors, and Basic Results.* ApJS, 192(2):14.

Jeans, J. H. (1928). *Astronomy and cosmogony.* Cambridge University Press.

Jenkins, A. (2010). *Second-order Lagrangian perturbation theory initial conditions for resimulations.* MNRAS, 403(4):1859–1872.

Kafle, P. R., Sharma, S., Lewis, G. F., and Bland-Hawthorn, J. (2014). *On the Shoulders of Giants: Properties of the Stellar Halo and the Milky Way Mass Distribution.* ApJ, 794(1):59.

Kennicutt, Robert C., J. (1998). *The Global Schmidt Law in Star-forming Galaxies.* ApJ, 498(2):541–552.

Kiepenheuer, K. O. (1950). *Cosmic Rays as the Source of General Galactic Radio Emission.* Physical Review, 79(4):738–739.

King, A. and Nixon, C. (2015). *AGN flickering and chaotic accretion.* MNRAS, 453(1):L46–L47.

Klypin, A. A., Trujillo-Gomez, S., and Primack, J. (2011). *Dark Matter Halos in the Standard Cosmological Model: Results from the Bolshoi Simulation.* ApJ, 740(2):102.

Kolmogorov, A. (1941). *The Local Structure of Turbulence in Incompressible Viscous Fluid for Very Large Reynolds' Numbers.* The Proceedings of the USSR Academy of Sciences, 30:301–305.

Kormendy, J. and Ho, L. C. (2013). *Coevolution (Or Not) of Supermassive Black Holes and Host Galaxies.* ARA&A, 51(1):511–653.

Kotarba, H., Karl, S. J., Naab, T., et al. (2010). *Simulating Magnetic Fields in the Antennae Galaxies.* ApJ, 716(2):1438–1452.

Kotarba, H., Lesch, H., Dolag, K., et al. (2011). *Galactic ménage à trois: simulating magnetic fields in colliding galaxies.* MNRAS, 415(4):3189–3218.

Krause, M., Hummel, E., and Beck, R. (1989). *The magnetic field structures in two nearby spiral galaxies. I. The axisymmetric spiral magnetic field in IC 342.* A&A, 217:4–16.

Kravtsov, A. V., Vikhlinin, A. A., and Meshcheryakov, A. V. (2018). *Stellar Mass—Halo Mass Relation and Star Formation Efficiency in High-Mass Halos.* Astronomy Letters, 44(1):8–34.

Kroupa, P. (2001). *On the variation of the initial mass function.* MNRAS, 322(2):231–246.

Kulsrud, R. M., Cen, R., Ostriker, J. P., and Ryu, D. (1997). *The Protogalactic Origin for Cosmic Magnetic Fields.* ApJ, 480(2):481–491.

Lacki, B. C. and Beck, R. (2013). *The equipartition magnetic field formula in starburst galaxies: accounting for pionic secondaries and strong energy losses.* MNRAS, 430(4):3171–3186.

Li, H.-B. and Henning, T. (2011). *The alignment of molecular cloud magnetic fields with the spiral arms in M33.* Nature, 479(7374):499–501.

Lopez-Rodriguez, E., Dowell, C. D., Jones, T. J., et al. (2019). *SOFIA/HAWC+ traces the magnetic fields in NGC 1068.* arXiv e-prints, page arXiv:1907.06648.

Lupton, R., Blanton, M. R., Fekete, G., et al. (2004). *Preparing Red-Green-Blue Images from CCD Data.* PASP, 116(816):133–137.

Lynden-Bell, D. (1967). *Statistical mechanics of violent relaxation in stellar systems.* MNRAS, 136:101.

Maccagni, F. M., Murgia, M., Serra, P., et al. (2020). *The flickering nuclear activity of Fornax A.* A&A, 634:A9.

Madau, P. and Dickinson, M. (2014). *Cosmic Star-Formation History.* ARA&A, 52:415–486.

Maddox, S. J., Efstathiou, G., Sutherland, W. J., and Loveday, J. (1990). *Galaxy correlations on large scales.* MNRAS, 242:43.

Manchester, R. N. (1972). *Pulsar Rotation and Dispersion Measures and the Galactic Magnetic Field.* ApJ, 172:43.

Marconi, A. and Hunt, L. K. (2003). *The Relation between Black Hole Mass, Bulge Mass, and Near-Infrared Luminosity.* ApJ, 589(1):L21–L24.

Marinacci, F., Pakmor, R., and Springel, V. (2014). *The formation of disc galaxies in high-resolution moving-mesh cosmological simulations.* MNRAS, 437(2):1750–1775.

Marinacci, F., Sales, L. V., Vogelsberger, M., Torrey, P., and Springel, V. (2019). *Simulating the interstellar medium and stellar feedback on a moving mesh: implementation and isolated galaxies.* MNRAS, 489(3):4233–4260.

Marinacci, F. and Vogelsberger, M. (2016). *Effects of simulated cosmological magnetic fields on the galaxy population.* MNRAS, 456(1):L69–L73.

Marinacci, F., Vogelsberger, M., Kannan, R., et al. (2018a). *Non-ideal magnetohydrodynamics on a moving mesh.* MNRAS, 476(2):2476–2492.

Marinacci, F., Vogelsberger, M., Pakmor, R., et al. (2018b). *First results from the IllustrisTNG simulations: radio haloes and magnetic fields.* MNRAS, 480(4):5113–5139.

Markevitch, M., Gonzalez, A. H., Clowe, D., et al. (2004). *Direct Constraints on the Dark Matter Self-Interaction Cross Section from the Merging Galaxy Cluster 1E 0657-56.* ApJ, 606(2):819–824.

McKee, C. F. and Ostriker, E. C. (2007). *Theory of Star Formation.* ARA&A, 45(1):565–687.

Meszaros, P. (1974). *The behaviour of point masses in an expanding cosmological substratum.* A&A, 37(2):225–228.

Mihos, J. C. and Hernquist, L. (1996). *Gasdynamics and Starbursts in Major Mergers.* ApJ, 464:641.

Mocz, P., Pakmor, R., Springel, V., et al. (2016). *A moving mesh unstaggered constrained transport scheme for magnetohydrodynamics.* MNRAS, 463(1):477–488.

Mocz, P., Vogelsberger, M., Sijacki, D., Pakmor, R., and Hernquist, L. (2014). *A discontinuous Galerkin method for solving the fluid and magnetohydrodynamic equations in astrophysical simulations.* MNRAS, 437(1):397–414.

Monaghan, J. J. (1992). *Smoothed particle hydrodynamics.* ARA&A, 30:543–574.

Monaghan, J. J. (2005). *Smoothed particle hydrodynamics.* Reports on Progress in Physics, 68(8):1703–1759.

Moster, B. P., Somerville, R. S., Maulbetsch, C., et al. (2010). *Constraints on the Relationship between Stellar Mass and Halo Mass at Low and High Redshift.* ApJ, 710(2):903–923.

Naab, T. and Ostriker, J. P. (2017). *Theoretical Challenges in Galaxy Formation.* ARA&A, 55(1):59–109.

Navarro, J. F., Frenk, C. S., and White, S. D. M. (1996). *The Structure of Cold Dark Matter Halos.* ApJ, 462:563.

Negroponte, J. and White, S. D. M. (1983). *Simulations of mergers between disc-halo galaxies.* MNRAS, 205:1009–1029.

Nelson, D., Pillepich, A., Genel, S., et al. (2015). *The Illustris simulation: Public data release.* Astronomy and Computing, 13:12–37.

Nelson, D., Springel, V., Pillepich, A., et al. (2019). *The IllustrisTNG simulations: public data release.* Computational Astrophysics and Cosmology, 6(1):2.

Niklas, S. (1995). *Eigenschaften von Spiralgalaxien im hochfrequenten Radiokontinuum.* PhD Thesis, University of Bonn.

Noguchi, M. (1987). *Close encounter between galaxies - II. Tidal deformation of a disc galaxy stabilized by massive halo.* MNRAS, 228:635–651.

Nulsen, P. E. J. and Fabian, A. C. (2000). *Fuelling quasars with hot gas.* MNRAS, 311(2):346–356.

Okamoto, T., Frenk, C. S., Jenkins, A., and Theuns, T. (2010). *The properties of satellite galaxies in simulations of galaxy formation.* MNRAS, 406(1):208–222.

Orr, M. E., Hayward, C. C., Hopkins, P. F., et al. (2018). *What FIREs up star formation: the emergence of the Kennicutt-Schmidt law from feedback.* MNRAS, 478(3):3653–3673.

Pakmor, R., Bauer, A., and Springel, V. (2011). *Magnetohydrodynamics on an unstructured moving grid.* MNRAS, 418(2):1392–1401.

Pakmor, R., Gómez, F. A., Grand , R. J. J., et al. (2017). *Magnetic field formation in the Milky Way like disc galaxies of the Auriga project.* MNRAS, 469(3):3185–3199.

Pakmor, R., Guillet, T., Pfrommer, C., et al. (2018). *Faraday rotation maps of disc galaxies.* MNRAS, 481(4):4410–4418.

Pakmor, R., Marinacci, F., and Springel, V. (2014). *Magnetic Fields in Cosmological Simulations of Disk Galaxies.* ApJ, 783(1):L20.

Pakmor, R., Pfrommer, C., Simpson, C. M., Kannan, R., and Springel, V. (2016). *Semi-implicit anisotropic cosmic ray transport on an unstructured moving mesh.* MNRAS, 462(3):2603–2616.

Pakmor, R. and Springel, V. (2013). *Simulations of magnetic fields in isolated disc galaxies.* MNRAS, 432(1):176–193.

Parker, E. N. (1992). *Fast Dynamos, Cosmic Rays, and the Galactic Magnetic Field.* ApJ, 401:137.

Peebles, P. J. E. (1970). *Structure of the Coma Cluster of Galaxies.* AJ, 75:13.

Perlmutter, S., Aldering, G., Goldhaber, G., et al. (1999). *Measurements of Ω and Λ from 42 High-Redshift Supernovae.* ApJ, 517(2):565–586.

Pfrommer, C., Pakmor, R., Schaal, K., Simpson, C. M., and Springel, V. (2017). *Simulating cosmic ray physics on a moving mesh.* MNRAS, 465(4):4500–4529.

Planck Collaboration (2014). *Planck 2013 results. I. Overview of products and scientific results.* A&A, 571:A1.

Planck Collaboration (2016). *Planck 2015 results. XIX. Constraints on primordial magnetic fields.* A&A, 594:A19.

Planck Collaboration (2018). *Planck 2018 results. VI. Cosmological parameters.* arXiv e-prints.

Pohlen, M. and Trujillo, I. (2006). *The structure of galactic disks. Studying late-type spiral galaxies using SDSS.* A&A, 454(3):759–772.

Powell, K. G., Roe, P. L., Linde, T. J., Gombosi, T. I., and De Zeeuw, D. L. (1999). *A Solution-Adaptive Upwind Scheme for Ideal Magnetohydrodynamics.* Journal of Computational Physics, 154(2):284–309.

Power, C., Navarro, J. F., Jenkins, A., et al. (2003). *The inner structure of ΛCDM haloes - I. A numerical convergence study.* MNRAS, 338(1):14–34.

Price, D. J. and Monaghan, J. J. (2007). *An energy-conserving formalism for adaptive gravitational force softening in smoothed particle hydrodynamics and N-body codes.* MNRAS, 374(4):1347–1358.

Primack, J. R. (2009). *Dark Matter and Galaxy Formation.* American Institute of Physics Conference Series, 1192:101–137.

Rautiainen, P. and Salo, H. (2000). *Presence and Absence of Outer Rings in Barred Galaxies.* IAU Colloq. 174: Small Galaxy Groups, 209:330.

Raymond, J. C. (1992). *Microflare Heating of the Galactic Halo.* ApJ, 384:502.

Rees, M. J. (2005). *Magnetic Fields in the Early Universe.* Lecture Notes in Physics, 664:1.

Rees, M. J. and Ostriker, J. P. (1977). *Cooling, dynamics and fragmentation of massive gas clouds: clues to the masses and radii of galaxies and clusters.* MNRAS, 179:541–559.

Renaud, F., Bournaud, F., Kraljic, K., and Duc, P. A. (2014). *Starbursts triggered by intergalactic tides andinterstellar compressive turbulence.* MNRAS, 442:L33–L37.

Riess, A. G., Filippenko, A. V., Challis, P., et al. (1998). *Observational Evidence from Supernovae for an Accelerating Universe and a Cosmological Constant.* AJ, 116(3):1009–1038.

Robertson, B., Bullock, J. S., Cox, T. J., et al. (2006). *A Merger-driven Scenario for Cosmological Disk Galaxy Formation.* ApJ, 645(2):986–1000.

Rodenbeck, K. and Schleicher, D. R. G. (2016). *Magnetic fields during galaxy mergers.* A&A, 593:A89.

Rodriguez-Gomez, V., Genel, S., Vogelsberger, M., et al. (2015). *The merger rate of galaxies in the Illustris simulation: a comparison with observations and semi-empirical models.* MNRAS, 449(1):49–64.

Rodriguez-Gomez, V., Sales, L. V., Genel, S., et al. (2017). *The role of mergers and halo spin in shaping galaxy morphology.* MNRAS, 467(3):3083–3098.

Rubin, V. C., Ford, W. K., J., and Thonnard, N. (1980). *Rotational properties of 21 SC galaxies with a large range of luminosities and radii, from NGC 4605 (R=4kpc) to UGC 2885 (R=122kpc).* ApJ, 238:471–487.

Rubin, V. C. and Ford, W. Kent, J. (1970). *Rotation of the Andromeda Nebula from a Spectroscopic Survey of Emission Regions.* ApJ, 159:379.

Ruzmaikin, A. A. and Sokolov, D. D. (1977). *The Scale and Strength of the Galactic Magnetic Field According to the Pulsar Data.* Ap&SS, 52(2):365–374.

Sales, L. V., Navarro, J. F., Theuns, T., et al. (2012). *The origin of discs and spheroids in simulated galaxies.* MNRAS, 423(2):1544–1555.

Salpeter, E. E. (1955). *The Luminosity Function and Stellar Evolution.* ApJ, 121:161.

Sandage, A. (1961). *The Hubble Atlas of Galaxies.* Carnegie Institution, Washington.

Sanders, D. B., Soifer, B. T., Elias, J. H., et al. (1988). *Ultraluminous Infrared Galaxies and the Origin of Quasars.* ApJ, 325:74.

Scannapieco, C., Wadepuhl, M., Parry, O. H., et al. (2012). *The Aquila comparison project: the effects of feedback and numerical methods on simulations of galaxy formation.* MNRAS, 423(2):1726–1749.

Scannapieco, C., White, S. D. M., Springel, V., and Tissera, P. B. (2009). *The formation and survival of discs in a ΛCDM universe.* MNRAS, 396(2):696–708.

Schleicher, D. R. G. and Miniati, F. (2011). *Primordial magnetic field constraints from the end of reionization.* MNRAS, 418(1):L143–L147.

Schlickeiser, R. and Shukla, P. K. (2003). *Cosmological Magnetic Field Generation by the Weibel Instability.* ApJ, 599(2):L57–L60.

Schmidt, M. (1959). *The Rate of Star Formation.* ApJ, 129:243.

Scoville, N., Sheth, K., Aussel, H., et al. (2016). *ISM Masses and the Star formation Law at Z = 1 to 6: ALMA Observations of Dust Continuum in 145 Galaxies in the COSMOS Survey Field.* ApJ, 820(2):83.

Sérsic, J. L. (1963). *Influence of the atmospheric and instrumental dispersion on the brightness distribution in a galaxy.* Boletín de la Asociación Argentina de Astronomía, 6:41.

Shukurov, A., Sokoloff, D., Subramanian, K., and Brand enburg, A. (2006). *Galactic dynamo and helicity losses through fountain flow.* A&A, 448(2):L33–L36.

Sijacki, D., Vogelsberger, M., Kereš, D., Springel, V., and Hernquist, L. (2012). *Moving mesh cosmology: the hydrodynamics of galaxy formation.* MNRAS, 424(4):2999–3027.

Silk, J. and Rees, M. J. (1998). *Quasars and galaxy formation.* A&A, 331:L1–L4.

Simard-Normandin, M. and Kronberg, P. P. (1979). *New large-scale magnetic features of the Milky Way.* Nature, 279(5709):115–118.

Smoot, G. F., Bennett, C. L., Kogut, A., et al. (1992). *Structure in the COBE Differential Microwave Radiometer First-Year Maps.* ApJ, 396:L1.

Snyder, G. F., Torrey, P., Lotz, J. M., et al. (2015). *Galaxy morphology and star formation in the Illustris Simulation at z = 0.* MNRAS, 454(2):1886–1908.

Soida, M., Beck, R., Urbanik, M., and Braine, J. (2002). *Magnetic fields in the absence of spiral density waves - NGC 4414.* A&A, 394:47–57.

Somerville, R. S. and Davé, R. (2015). *Physical Models of Galaxy Formation in a Cosmological Framework.* ARA&A, 53:51–113.

Sparre, M. and Springel, V. (2016). *Zooming in on major mergers: dense, starbursting gas in cosmological simulations.* MNRAS, 462(3):2418–2430.

Sparre, M. and Springel, V. (2017). *The unorthodox evolution of major merger remnants into star-forming spiral galaxies.* MNRAS, 470(4):3946–3958.

Springel, V. (2005). *The cosmological simulation code GADGET-2.* MNRAS, 364(4):1105–1134.

Springel, V. (2010a). *E pur si muove: Galilean-invariant cosmological hydrodynamical simulations on a moving mesh.* MNRAS, 401(2):791–851.

Springel, V. (2010b). *Smoothed Particle Hydrodynamics in Astrophysics.* ARA&A, 48:391–430.

Springel, V. (2012). *Larger, faster, better: Current trends in cosmological simulations.* Astronomische Nachrichten, 333(5-6):515–522.

Springel, V. (2015). *N-GenIC: Cosmological structure initial conditions.*

Springel, V., Di Matteo, T., and Hernquist, L. (2005a). *Modelling feedback from stars and black holes in galaxy mergers.* MNRAS, 361(3):776–794.

Springel, V., Frenk, C. S., and White, S. D. M. (2006). *The large-scale structure of the Universe.* Nature, 440(7088):1137–1144.

Springel, V. and Hernquist, L. (2003). *Cosmological smoothed particle hydrodynamics simulations: a hybrid multiphase model for star formation.* MNRAS, 339(2):289–311.

Springel, V., White, S. D. M., Jenkins, A., et al. (2005b). *Simulations of the formation, evolution and clustering of galaxies and quasars.* Nature, 435(7042):629–636.

Springel, V., White, S. D. M., Tormen, G., and Kauffmann, G. (2001). *Populating a cluster of galaxies - I. Results at $z = 0$.* MNRAS, 328(3):726–750.

Steinwandel, U. P., Beck, M. C., Arth, A., et al. (2019). *Magnetic buoyancy in simulated galactic discs with a realistic circumgalactic medium.* MNRAS, 483(1):1008–1028.

Subramanian, K. (2016). *The origin, evolution and signatures of primordial magnetic fields.* Reports on Progress in Physics, 79(7):076901.

Sutherland, R. S. and Dopita, M. A. (1993). *Cooling Functions for Low-Density Astrophysical Plasmas.* ApJS, 88:253.

Tacchella, S., Diemer, B., Hernquist, L., et al. (2019). *Morphology and star formation in IllustrisTNG: the build-up of spheroids and discs.* MNRAS, 487(4):5416–5440.

Taylor, A. N., Dye, S., Broadhurst, T. J., Benítez, N., and van Kampen, E. (1998). *Gravitational Lens Magnification and the Mass of Abell 1689.* ApJ, 501(2):539–553.

Teyssier, R., Chapon, D., and Bournaud, F. (2010). *The Driving Mechanism of Starbursts in Galaxy Mergers.* ApJ, 720(2):L149–L154.

Toomre, A. (1974). *Gravitational Interactions Between Galaxies (invited Paper).* The Formation and Dynamics of Galaxies, 58:347.

Toomre, A. (1977). *Mergers and Some Consequences.* Evolution of Galaxies and Stellar Populations, page 401.

Toomre, A. and Toomre, J. (1972). *Galactic Bridges and Tails.* ApJ, 178:623–666.

Tremaine, S. D., Ostriker, J. P., and Spitzer, L., J. (1975). *The formation of the nuclei of galaxies. I. M31.* ApJ, 196:407–411.

Trujillo-Gomez, S., Klypin, A., Primack, J., and Romanowsky, A. J. (2011). *Galaxies in ΛCDM with Halo Abundance Matching: Luminosity-Velocity Relation, Baryonic Mass-Velocity Relation, Velocity Function, and Clustering.* ApJ, 742(1):16.

Übler, H., Naab, T., Oser, L., et al. (2014). *Why stellar feedback promotes disc formation in simulated galaxies.* MNRAS, 443(3):2092–2111.

van Dokkum, P. G. and Conroy, C. (2010). *A substantial population of low-mass stars in luminous elliptical galaxies.* Nature, 468(7326):940–942.

Vishniac, E. (2005). *The Magnetic Helicity Current in an Alpha-Omega Dynamo*. The Magnetized Plasma in Galaxy Evolution, pages 177–184.

Vogelsberger, M., Genel, S., Sijacki, D., et al. (2013). *A model for cosmological simulations of galaxy formation physics*. MNRAS, 436(4):3031–3067.

Vogelsberger, M., Genel, S., Springel, V., et al. (2014a). *Properties of galaxies reproduced by a hydrodynamic simulation*. Nature, 509(7499):177–182.

Vogelsberger, M., Genel, S., Springel, V., et al. (2014b). *Introducing the Illustris Project: simulating the coevolution of dark and visible matter in the Universe*. MNRAS, 444(2):1518–1547.

Vollmer, B., Soida, M., Beck, R., et al. (2013). *Large-scale radio continuum properties of 19 Virgo cluster galaxies. The influence of tidal interactions, ram pressure stripping, and accreting gas envelopes*. A&A, 553:A116.

Wang, P. and Abel, T. (2009). *Magnetohydrodynamic Simulations of Disk Galaxy Formation: The Magnetization of the Cold and Warm Medium*. ApJ, 696(1):96–109.

Weinberger, R., Springel, V., and Pakmor, R. (2019). *The Arepo public code release*. ApJS, arXiv:1909.04667.

Welker, C., Dubois, Y., Devriendt, J., et al. (2017). *The rise and fall of stellar discs across the peak of cosmic star formation history: effects of mergers versus diffuse stellar mass acquisition*. MNRAS, 465(1):1241–1258.

Wetzel, A. R., Cohn, J. D., and White, M. (2009). *Simulating subhaloes at high redshift: merger rates, counts and types*. MNRAS, 395(3):1376–1390.

White, S. D. M. and Rees, M. J. (1978). *Core condensation in heavy halos: a two-stage theory for galaxy formation and clustering*. MNRAS, 183:341–358.

Widrow, L. M. (2002). *Origin of galactic and extragalactic magnetic fields*. Reviews of Modern Physics, 74(3):775–823.

Wielebinski, R. and Beck, R. (2005). *Cosmic Magnetic Fields*. Lecture Notes in Physics, 664.

Wiersma, R. P. C., Schaye, J., and Smith, B. D. (2009). *The effect of photoionization on the cooling rates of enriched, astrophysical plasmas*. MNRAS, 393(1):99–107.

Yoachim, P. and Dalcanton, J. J. (2006). *Structural Parameters of Thin and Thick Disks in Edge-on Disk Galaxies*. AJ, 131(1):226–249.

Yoshida, N., Oh, S. P., Kitayama, T., and Hernquist, L. (2007). *Early Cosmological H II/He III Regions and Their Impact on Second-Generation Star Formation*. ApJ, 663(2):687–707.

Zel'Dovich, Y. B. (1970). *Gravitational instability: an approximate theory for large density perturbations*. A&A, 500:13–18.

Zhang, X. (1999). *Secular Evolution of Spiral Galaxies. III. The Hubble Sequence as a Temporal Evolution Sequence*. ApJ, 518(2):613–626.

Zwicky, F. (1933). *Die Rotverschiebung von extragalaktischen Nebeln*. Helvetica Physica Acta, 6:110–127.

Appendix A

Appendix

A.1 Distance between the black hole and the galactic potential minimum

In Subsection 2.2.3, we observed that tracking a subhalo between snapshots is frequently akin to tracking the black hole particle that resides in that subhalo. This is shown in Fig. A.1, where we can see clearly that for the vast majority of snapshots, the distance between the closest black hole and the galactic centre (as defined in Subsection 2.2.4) does not exceed 5 kpc. This black hole is always the same particle, as shown by the continuity in the distance measurements and in the black hole mass evolution (see bottom row of Fig. 3.17). Fig. A.1 therefore provides further support that our galaxy tracking has been accurate.

In simulation 1526-3H, the merging galaxy passes through the main galaxy. For a short time afterwards, the black hole of the main galaxy becomes gravitationally bound to the merging galaxy. Indeed, we can see that its distance from the main galaxy between 7.11 Gyr and 6.35 Gyr is approximately equal to the distance between the merging galaxies, as shown in the bottom row of Fig. 3.5 and Fig. 3.6. During this time as well, SUBFIND allocates most of the mass in the system to the merging galaxy. This is inconsistent with our visual-based galaxy tracking method (as defined in Subsection 2.2.3). It is for this reason that we do not plot subhalo values for 1526-3H during these times. In practise this only affects Fig. 3.1.1 and Fig. 3.2.3.

Finally, this plot may help to explain the discrepancies seen between the black hole accretion rates shown in the third row of Fig. 3.17 and the 'inner gas velocity' as shown in the top row of the same figure. As explained in Subsection 2.1.4, energy is continuously injected into gas cells neighbouring the black hole with a rate proportional to the accreted gas mass. However,

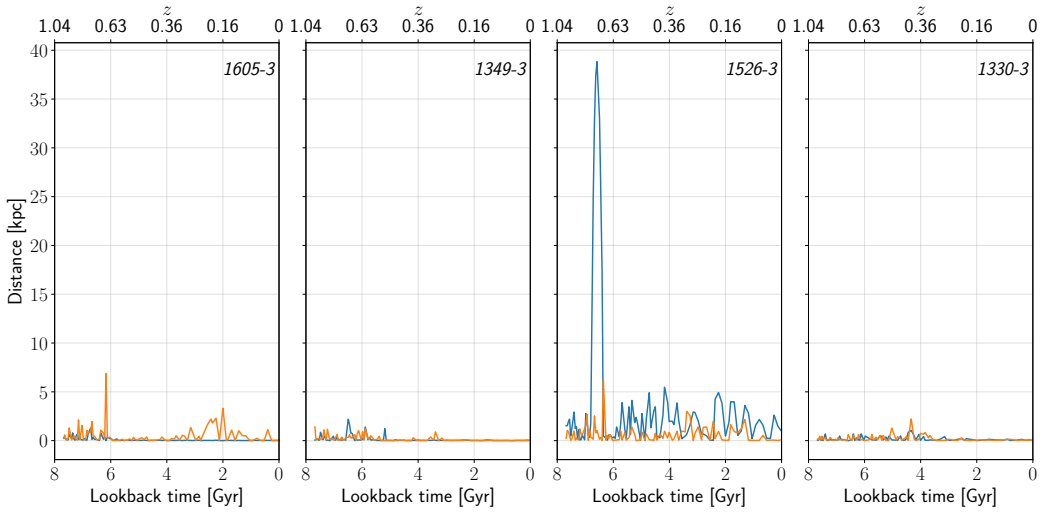

Figure A.1: Proper distance between the galactic potential minimum and the closest black hole for the main galaxy in each simulation (as defined in Section 2.2.2) as a function of time. Orange (blue) lines show simulations that included MHD (hydrodynamic) physics. The prefix for each simulation may be found in the top righthand corner of each panel. For simulation 1526-3H between 7.11 Gyr and 6.35 Gyr, the black hole briefly joins a different galaxy during the merger. For virtually every other data point, the distance is <5 kpc. The differences that there are help to explain the discrepancies seen between the black hole activity and inner gas velocity, as explained in Fig. 3.17.

it is clear from Fig. A.1 that these gas cells will not always be at the galaxy centre. Our measurement of the inner gas velocity *is* based on the centre though, and is only measured over a disc of radius 0.5 kpc. We may therefore over or underestimate some outbursts through this measure. In particular, it may be a factor that led to the high inner gas velocities seen for the simulations with the prefix 1526-3, even when the accreted gas mass in these simulations was relatively low.

The galactic centre is also where the gravitational potential is generally lowest, and hence where the most mass is concentrated. As we keep gas cells within a target mass, the cell sizes here will be relatively smaller compared to the rest of the galaxy. Consequently, the injected energy will be more localised. Correspondingly, for times when the black hole is further away from the galactic centre, the neighbouring cell sizes will likely be larger, resulting in an outburst that is more spread out. This could affect both our measurement and the simulation behaviour. This may be a factor in the differing morphologies seen for 1526-3H and 1526-3M, even when the two simulations showed relatively similar gas accretion histories (see Subsection 3.5.2).